UNIVERSITY OF CALIFORNIA

Santa Barbara

Electronic Structure, Chemical Mechanism, and Morphology in Doping Organic Semiconductors

A dissertation submitted in partial satisfaction of the

requirements for the degree Doctor of Philosophy

in Materials

by

Kelly Ann Peterson

Committee in charge:

Professor Michael L. Chabinyc, Chair

Professor Craig J. Hawker

Professor Christopher M. Bates

Professor Steven K. Buratto

December 2021

The dissertation of Kelly Ann Peterson is approved.

_____

Craig J. Hawker

_____

Christopher M. Bates

_____

Steven K. Buratto

_____

Michael L. Chabinyc, Committee Chair

December 2021

Electronic Structure, Chemical Mechanism, and Morphology in Doping Organic Semiconductors

by

Kelly Ann Peterson

ACKNOWLEDGEMENTS

I would like to thank my advisor, Michael Chabinyc, for his mentorship over the years. I truly appreciate that he gave me the freedom to pursue the research I was interested in on my own terms. I also thank my committee members for their feedback and consideration of my work.

Thank you to all of the members of the Chabinyc group for their help and for making the group a nice place to work. They taught me how to use so many techniques and pieces of lab equipment, helped keep everything in the lab working well, and provided input on this work.

I would like to thank the MRL, CNSI, CSC, and Materials department staff for all of the work that goes into the lab equipment, facilities, and administration that were necessary for this research.

Thank you to my friends for their support and for their company in Santa Barbara. Thank you to my parents, Mark and Sheryl, and my sister, Hanna, for their support and belief in me.

And thank you to everyone above for doing those things during a global pandemic!

VITA OF KELLY ANN PETERSON
December 2021

EDUCATION

Bachelor of Science in Chemistry, Case Western Reserve University, May 2015

Doctor of Philosophy in Materials, University of California, Santa Barbara, December 2021 (expected)

PROFESSIONAL EMPLOYMENT

2012-2014: Undergraduate Researcher, Department of Materials Science and Engineering, Case Western Reserve University

2014-2015: Undergraduate Researcher, Departments of Materials Science and Engineering and Chemistry, Case Western Reserve University

Winter 2016: Teaching Assistant, Materials Department, University of California, Santa Barbara

2015-2021: Graduate Student Researcher, Materials Department, University of California, Santa Barbara

PUBLICATIONS

- E. M. Thomas, **K. A. Peterson**, A. H. Balzer, D. Rawlings, N. Stingelin, R. A. Segalman and M. L. Chabinyc, Effects of Counter-Ion Size on Delocalization of Carriers and Stability of Doped Semiconducting Polymers, *Adv. Electron. Mater.*, 2020, **6**, 2000595.
- **K. A. Peterson,** A. Patterson, A. Vega-Flick, B. Liao and M. L. Chabinyc, Doping molecular organic semiconductors by diffusion from the vapor phase, *Mater. Chem. Front.*, 2020, **4**, 3632–3639.
- **K. A. Peterson**, E. M. Thomas and M. L. Chabinyc, Thermoelectric Properties of Semiconducting Polymers, *Annu. Rev. Mater. Res.*, 2020, **50**, 551–574.
- **K. A. Peterson**, E. Lim and M. L. Chabinyc, in *Conjugated Polymers*, eds. J. R. Reynolds, B. C. Thompson and T. A. Skotheim, CRC Press, 4th edn., 2019, pp. 129–159.
- E. Lim, **K. A. Peterson**, G. M. Su and M. L. Chabinyc, Thermoelectric Properties of Poly(3-hexylthiophene) (P3HT) Doped with 2,3,5,6-Tetrafluoro-7,7,8,8-tetracyanoquinodimethane (F4TCNQ) by Vapor-Phase Infiltration, *Chem. Mater.*, 2018, **30**, 998–1010.
- S. N. Patel, A. M. Glaudell, **K. A. Peterson**, E. M. Thomas, K. A. O'Hara, E. Lim and M. L. Chabinyc, Morphology controls the thermoelectric power factor of a doped semiconducting polymer, *Sci. Adv.*, 2017, **3**, e1700434.
- H. M. Mirletz, **K. A. Peterson**, I. T. Martin and R. H. French, Degradation of transparent conductive oxides: Interfacial engineering and mechanistic insights, *Sol. Energy Mater. and Sol. Cells*, 2015, **143**, 529–538.

- Y. Stark, D. M. Dryden, J. Olderman, **K. A. Peterson**, P. H. Niewiarowski, R. H. French and A. Dhinojwala, Adhesive interactions of geckos with wet and dry fluoropolymer substrates, *J. R. Soc., Interface*, 2015, **12**, 20150464.

PRESENTATIONS

- K. A. Peterson, A. Patterson, A. Vega-Flick, B. Liao, M. L. Chabinyc, "Disordered Transport in Highly Doped Materials—Vapor Doping of a Small Molecule System," 2018 MRS Fall Meeting, oral presentation.
- K. A. Peterson, A. Patterson, M. L. Chabinyc, "Vapor Doped Spiro-OMeTAD as a Model System for Disordered Charge Transport," APS March Meeting 2018, poster presentation.
- K. A. Peterson, A. Patterson, M. L. Chabinyc, "Charge Transport in Vapor Doped Spiro-OMeTAD," 2017 MRS Fall Meeting, poster presentation.

AWARDS

Hypercube Scholar Award, CWRU, 2015
The Carl F. Prutton Prize, CWRU, 2014
The Iota Sigma Pi/Frank Hovorka Prize, CWRU, 2013

FIELDS OF STUDY

Doping of Organic Semiconductors with Professor Michael L. Chabinyc
Degradation of Polymer OLEDs with Professors Roger H. French and Emily B. Pentzer
Degradation of Transparent Conductive Oxides with Professor Roger H. French

ABSTRACT

Electronic Structure, Chemical Mechanism, and Morphology in Doping Organic Semiconductors

by

Kelly Ann Peterson

The properties of organic semiconductors make them well-suited for certain applications in electronic devices or energy conversion. Because of their low inherent conductivity, organic semiconductors need to be doped to be used in many of these applications. The limited set of small molecules commonly used for organic semiconductor doping do not always have the desired combination of properties for some applications, such as high ionization energy or air stability. In addition to removing or adding charges, these small molecule dopants can significantly alter the semiconducting film structure through Coulombic interactions. These challenges suggest a need to explore new dopants and doping mechanisms and to better understand the effects of doping on the electronic structure and morphology of organic semiconductors. We used a combination of experimental methods and DFT calculations to explore new doping mechanisms based on Lewis acid-base pair chemistry. Combining UV-Vis-NIR spectroscopy, electrical transport measurements, and grazing incidence wide-angle X-ray scattering, we connected changes in the electronic structure to changes in morphology and transport in both amorphous and semicrystalline semiconductor systems. Our results suggest ways to control the electronic structure and

morphology of organic semiconductors, as well as providing a starting point to further apply Lewis acid-base chemistry to doping.

TABLE OF CONTENTS

1. Introduction

1.1. Molecular Structure and Electronic Properties

Semiconducting polymers have conjugated backbones with alternating single and double carbon-carbon bonds (Figure 1.1). This pattern allows the unoccupied p orbitals of the carbon atoms to form delocalized π and π^* symmetry molecular orbitals along the polymer chain that are the valence and conduction bands of the single polymer chain. In the solid state, intermolecular interactions modify the energies of the single chain states, but these electronic interactions are weak. Thus, the electronic states are frequently described in terms of molecular levels. The ionization energy (IE) is associated with the highest occupied molecular orbital (HOMO), and the electron affinity (EA) is associated with the lowest unoccupied molecular orbital (LUMO). For example, the homopolymer poly(3-hexylthiophene) (P3HT) has an approximate IE level of 5.1 eV and EA level of ≈3.0 eV, giving an energy gap of 2.1 eV.[1] The band gap can be modified by the choice of monomer or by synthesizing copolymers with alternating electron-donating and -accepting units.[2] Judicious design of the donor and acceptor units allows the IE and EA to be tuned separately, which is helpful for chemical stability in the ambient.[2]

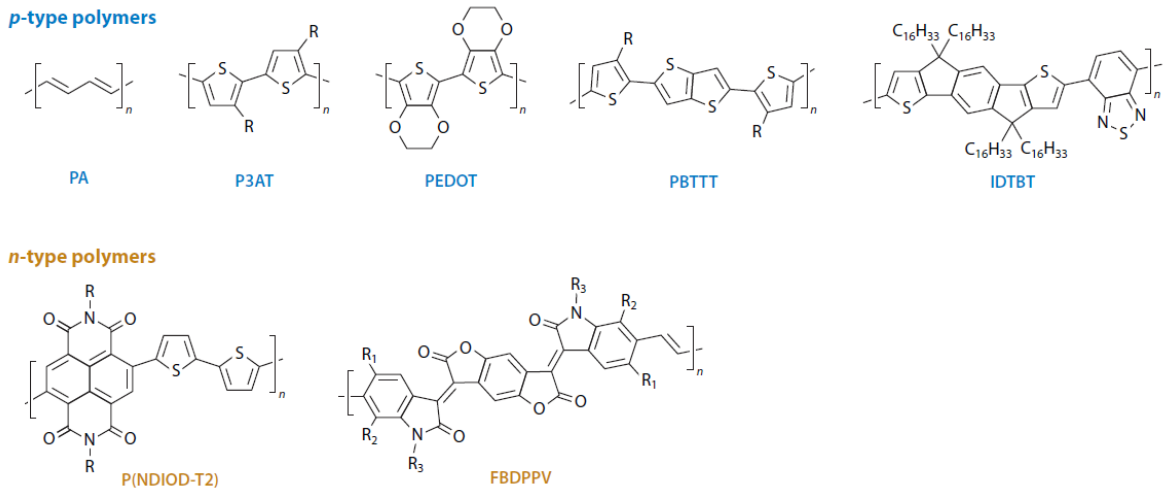

Figure 1.1. Chemical structures of widely studied *p*-type and *n*-type polymers. Abbreviations: FBDPPV, fluorinated benzodifurandione-phenylenevinylene; IDTBT, indacenodithiophene-*co*-benzothiadiazole; P3AT, poly(3-alkylthiophene); PA, polyacetylene; PBTTT, poly(2,5-bis(3-tetradecylthiophen-2-yl)thieno[3,2-b]thiophene); PEDOT, poly(3,4-ethylenedioxythiophene); P(NDIOD-T2), poly{[*N*,*N'*-bis(2-octyldodecyl)-naphthalene-1,4,5,8-bis(dicarboximide)-2,6-diyl]-*alt*-5,5'-(2,2'-bithiophene)}. Reprinted with permission from Reference 51. Copyright 2020 Annual Reviews.

Many semiconducting polymers have been developed with a wide range of band gaps and solution processabilities. The use of cyclic conjugated units and heterocycles in the backbone of the polymer provides the ability to rationally modify the IE and EA, but this structure leads to difficulties in processing because of the stiffening of the polymer backbone. To improve the processability of semiconducting polymers, side chains are added to the backbone to lower the melting point and to improve solubility in common solvents. These side chains are usually formed from functionalities that do not interact strongly with the π orbitals on the backbone, but they can help to tune the IE and EA by withdrawing or donating electron density. Semiconducting polymers with linear or branched alkyl side chains, such as P3HT and poly(2,5-bis(3-tetradecylthiophen-2-yl)thieno[3,2-b]thiophene) (PBTTT), have been among the most widely studied as thermoelectrics.

The interplay between the side chains and backbones helps to control the organization and properties of semiconducting polymers in the solid state. Electronic interaction between

the planar backbones of polymers leads to cofacial arrangement referred to as π-π stacking. These π-π stacks form lamellae that are separated by the side chains, commonly referred to as alkyl stacking for materials with alkyl side chains (Figure 1.2). This structural motif leads to crystallization for polymers with regioregular (RR) backbones. RR polymers have their monomers connected in the same isomeric sequence, i.e., head-to-tail. RR polymers, such as RR-P3HT, can crystallize because of the translational symmetry along the backbone. In contrast, regiorandom (RRa) polymers have monomers connected in a random arrangement, where some monomers are connected head-to-head and others tail-to-tail. In RRa-P3HT, the alkyl side chains will not have a regular spacing, and the polymer backbone will be less planar than RR-P3HT, making RRa-P3HT more soluble but unlikely to form crystallites in films. In RR polymers that form semicrystalline films, such as P3HT and PBTTT, charge transport within the crystallites can be highly anisotropic. Electronic transport is fastest along the conjugated backbones, and the π-π stacks facilitate electronic transport as well. However, transport is inhibited in the alkyl, or lamellar, stacking direction due to the insulating side chains (Figure 1.2). This anisotropy complicates the measurement of the thermoelectric properties. For example, in thin films, the backbone of conjugated polymers tends to lie parallel to the substrate. Crystallites with the alkyl stacking direction perpendicular to the substrate are called edge-on, while those with the π-π stacking direction perpendicular to the substrate are called face-on. Measurements of electrical and thermal transport taken in the in-plane and out-of-plane directions can differ because of the anisotropy of the polymer chains.

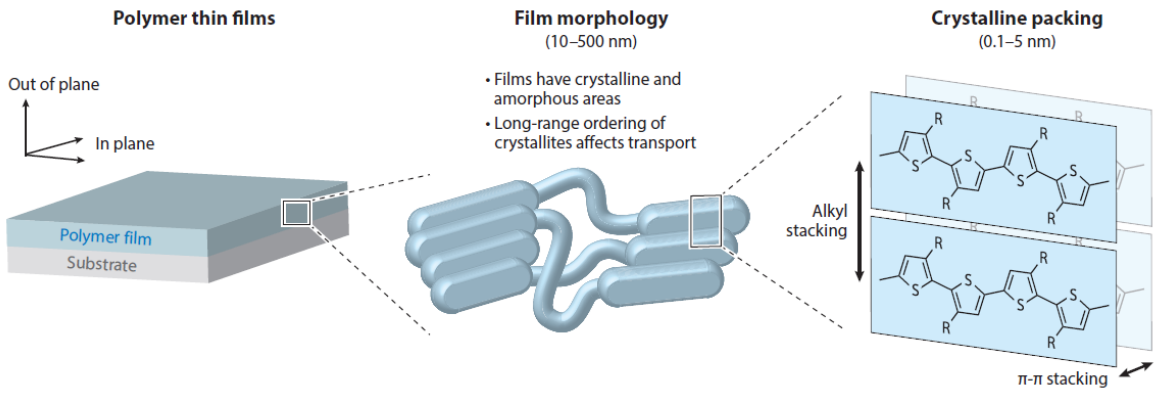

Figure 1.2. Thin films of semiconducting polymers have structural order over multiple length scales and directions that must be considered for interpretation of thermoelectric properties. Reprinted with permission from Reference 51. Copyright 2020 Annual Reviews.

1.2. Structural Order and Disorder

Semiconducting polymers have both structural and electronic disorder. Structural disorder can originate from polymer synthesis, e.g., chain defects and the polydispersity of the molecular weight of the polymer molecules, or from the kinetics of solidification from a solvent or the melt state. Because polymers have a limited amount of time to crystallize during solidification, polymer chains form an amorphous structure outside of the crystallites. The amorphous and crystalline regions exhibit different electronic properties. The band gap arises from the interaction of the π and π^* orbitals of the repeat units along the chain; therefore, conformational changes modify the electronic levels. For example, the IE of RRa-P3HT, which is thought to be mostly amorphous, is ≈5.25 eV, while that of RR-P3HT, which contains more crystalline domains, is ≈5 eV.[3] The conformational disorder disrupts intermolecular interactions, further modifying the electronic levels. Overall, the structural and electronic disorder broaden the electronic density of states (DOS), leading to trap states that reduce the carrier mobility.

The majority of the recent studies of the thermoelectric properties of polymers have been carried out on thin (~100 nm-thick) films rather than on bulk samples. Thin films have

advantages over bulk samples because physical characterization methods, such as optical spectroscopy and X-ray scattering, can be carried out without further steps that could perturb their morphology, e.g., sectioning.[4] These studies have revealed that alignment and connectivity of ordered domains are critical for charge transport because these ordered domains have the least electronic disorder and hence have a higher carrier mobility than disordered regions.[5] The connectivity of ordered domains is accomplished by domain boundaries and tie chains, which are polymer chains that extend and connect crystallites or ordered aggregates together through the amorphous regions.[5,6] It is critical that the molecular weight of a polymer is high enough such that tie chains can sufficiently connect crystallites by spanning intervening amorphous domains.[6] Charge carrier mobility is further improved if crystallites are aligned in one direction over a length scale several times the crystallite size. Processing strategies that increase chain alignment therefore tend to increase the carrier mobility of polymers.[7] The length scale of crystallite alignment can be observed using high-resolution transmission electron microscopy or small-angle X-ray scattering. Recently, resonant soft X-ray scattering (RSoXS) has proven helpful in defining an orientational correlation length (OCL) for the length scale over which backbones maintain comparable directionality.[8]

1.3. Doping Semiconducting Polymers

Doping is required to increase the conductivity and to optimize the power factor of semiconductors because most semiconducting polymers are highly insulating as synthesized. While inorganic semiconductors can be doped by substitution of atoms, organic semiconductors are doped by introducing molecular species that can remove or add electrons to the conjugated backbone. For polymers synthesized in an insulating state, several

mechanisms exist to introduce charge carriers. The most straightforward doping method involves charge transfer between the dopant and the polymeric backbone, where the resulting charged dopant acts as the counterion to the carrier on the polymer. In the case of *p*-type doping, charge transfer is energetically favorable when the HOMO energy level of the polymer is above the LUMO level of the dopant. Examples of *p*-type charge transfer dopants include tetrafluorotetracyanoquinodimethane (F_4TCNQ) and organometallic oxidants (Figure 1.3). In contrast, chemical doping involves a chemical reaction leading to charge transfer with the polymer and formation of a charge balancing counterion. For example, the salt $NOPF_6$ reacts by charge transfer followed by evolution of NO gas leaving PF_6^- as the counterion. Strong acids, such as 4-ethylbenzenesulfonic acid (EBSA), can protonate the backbone followed by subsequent reactions between chains to form charge carriers. Examples of *n*-type dopants include the charge transfer reductant tetrakis(dimethylamino)ethylene, the hydride transfer reagent 4-(2,3-dihydro-1,3-dimethyl-1*H*-benzimidazol-2-yl)-*N*,*N*-dimethylbenzenamine (N-DMBI),[9] and organometallic species (Figure 1.3).[10,11] Semiconducting polymers can also be synthesized in doped form; PEDOT is commonly synthesized in an oxidized state that is stabilized by poly(styrene sulfonate) (PSS), forming a water-processable dispersion, PEDOT:PSS.[12] Independent of the doping method, a counterion is present in a doped polymeric semiconductor to maintain charge neutrality.

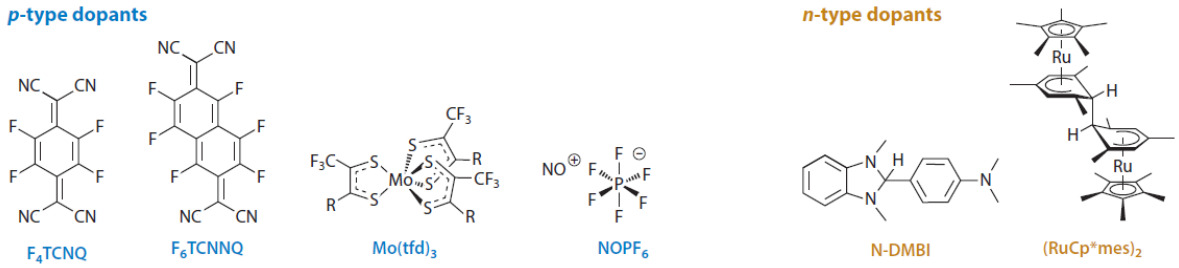

Figure 1.3. Chemical structures of charge transfer and chemical reactive dopants for polymeric semiconductors. Abbreviations: F_4TCNQ, tetrafluorotetracyanoquinodimethane; F_6TCNNQ, 1,3,4,5,7,8-hexafluoro-tetracyanonaphthoquinodimethane; $Mo(tfd)_3$, molybdenum tris(1,2-bis(trifluoromethyl)ethane-1,2-dithiolene); N-DMBI, 4-(2,3-dihydro-1,3-dimethyl-1*H*-benzimidazol-2-yl)-*N*,*N*-dimethylbenzenamine; $NOPF_6$, nitrosonium hexafluorophosphate; $(RuCp^*mes)_2$, mesitylene pentamethylcyclopentadienyl ruthenium dimer. Reprinted with permission from Reference 51. Copyright 2020 Annual Reviews.

An important question is how the charge carriers introduced on polymer chains interact with each other. The initial oxidation (or reduction) of the backbone leads to the formation of a singly charged species that can be localized, i.e., a polaron.[13] Polarons form because of the changes in molecular structure upon the introduction of charge carriers. The structural disorder also leads to energetic disorder, further localizing the charge carriers through broadening of the electronic DOS. The formation of charge carriers leads to bleaching of the main optical absorption of the neutral polymer and the appearance of suboptical gap transitions that are assigned to the polaronic levels. The energies of these transitions have been modeled and shown to depend on the separation of the counterion and the charge carrier.[14,15] Recent theoretical work suggests that shifts in optical transition can be correlated to the distance of anions from polarons, with greater polaron delocalization arising from increases in separation.[16] In addition to polarons, studies employing electron spin resonance (ESR) spectroscopy have indicated the formation of spinless carriers. When solutions with increasing doping levels were measured using ESR spectroscopy, the concentration of charge carriers first showed an increase in the concentration of spins with increasing doping but turned over at high concentrations.[17] The formation of spinless carriers has historically been attributed to

the formation of bipolarons, but the nature of the carriers is still debated.[18,19] The combination of spinless carriers and structural disorder makes determination of the carrier concentration using conventional methods, such as the Hall effect, difficult.[20,21]

Dopants cause significant changes in the processability and solid-state structure of polymers.[22] The charged counterions must be relatively close to the carriers on the backbone because of the low dielectric constant of the material. Additionally, the formation of charge carriers can stiffen the polymer chains as the charge delocalizes along the backbone.[16,23] These changes lead to a strong dependence of the thermoelectric properties on the processing and doping route used to form solid films.

To overcome the challenges associated with casting doped polymers, researchers have developed several methods to introduce dopants after film processing. If polymer chains are doped in a solvent (solution doping), charged polymer-dopant aggregates can precipitate from nonpolar solvents.[24] The model system of P3HT and F_4TCNQ has been widely studied in this context. Films cast from doped solutions tend to be relatively inhomogeneous and have relatively low electrical conductivity (<1 S/cm).[24] Sequential processing methods have been developed to prevent aggregation during film deposition. Sequential processing methods involve casting a neutral polymer film and then adding dopants in a second processing step. This second step often involves dissolving the dopant in an antisolvent for the polymer, i.e., an orthogonal solvent, so that the dopants can penetrate the polymer film without redissolving and washing off the film. For example, the polymer film can be immersed in a dopant solution in an orthogonal solvent (immersion doping). Dopant solution from an orthogonal solvent can also be spun cast on the polymer film (sequential casting).[24] Finally, volatile dopants, such as F_4TCNQ, can be diffused into polymer films from the vapor phase (vapor doping) without

using a second solvent.[25] These two-step methods take advantage of the ability to process the neutral semiconducting polymer into morphologies that are known to improve charge transport.

Dopants further affect the morphology of semiconducting polymers because of conformational changes in the backbone and through their electrostatic and steric interactions. P3HT, the most widely studied model system, demonstrates changes in morphology because of its combination of crystalline and amorphous domains. Smaller dopants like F_4TCNQ have been found to become incorporated into the alkyl chain portions of P3HT crystallites, as well as in the amorphous regions of the films.[24,26] For F_4TCNQ sequentially cast on P3HT films, the optical transition energy of the polaron in the IR region was consistent with simulations of anions 6–8 Å away from the P3HT polarons, indicating that anions were located in between alkyl chains or outside of crystallites.[15] Measurements of RRa-P3HT films with sequentially cast F_4TCNQ suggest that anions can be located even closer to polarons in amorphous regions of films, further localizing charges.[27,28] Dopants that are too large to be incorporated into alkyl stacking regions are located outside of polymer crystallites, potentially increasing the anion distance from the polaron.[29,30] F_4TCNQ doping also causes P3HT backbones to increase in planarity.[31] This dopant-induced backbone stiffening can even cause amorphous RRa-P3HT films to order into edge-on crystallites.[27,28,32] These results show how the electrostatic and steric effects of dopants are interrelated and change polymer film morphology.

Despite the understanding of the basic behavior, some aspects of doping remain to be elucidated. Seemingly contrary to the energetic driving force for charge transfer, uphill doping, where the dopant EA is slightly less than the polymer IE, has been observed in commonly used semiconducting polymers.[33] Conversely, common charge transfer dopants

such as F_4TCNQ have been shown to form partial charge transfer complexes with polymers where integer charge transfer was seemingly favorable.[34,35] In a charge transfer complex, only a partial charge transfer is completed between the donor and acceptor.[36] Because the donor and acceptor share electron density, charge transfer complexes do not provide free carriers for electrical conduction. A polythiophene with branched side chains, poly(3-(2'-ethyl)hexylthiophene), forms a charge transfer complex with F_4TCNQ, even though integer charge transfer would be energetically favorable based on its IE.[34] Due to the electronic and morphological complexities involved in doping semiconducting polymers, much still remains to be studied to optimize doping for thermoelectric applications.

1.4. Thermoelectric Properties

Thermoelectrics are materials that can readily interconvert electrical and thermal energy. While thermoelectric devices are currently made with inorganic materials,[37] there is emerging interest in applications where integrating inorganic materials into devices would be challenging. For example, modules operating near room temperature that are mechanically flexible could be used for wearable devices for health sensing.[38] This motivation has led to the investigation of semiconducting polymers as thermoelectric materials. The electronic properties of semiconducting polymers suggest they have significant potential as thermoelectric materials with the benefit of simple processing routes, such as printing or extrusion.[39,40]

Thermoelectric materials take advantage of the Seebeck effect, where an electric potential is generated in response to an applied thermal gradient, or the Peltier effect, where a thermal gradient is generated in response to an applied electric potential.[37] The magnitude of

the Seebeck effect is given by the Seebeck coefficient, or thermopower, S, where ΔV is the electric potential and ΔT is the temperature gradient (Equation 1.1):

$$S = -\frac{\Delta V}{\Delta T} \tag{1.1}$$

In *n*-type materials, the Seebeck coefficient is negative, while S is positive in *p*-type materials. In addition to the Seebeck coefficient, the thermoelectric performance of a material depends on its electrical conductivity, σ, and thermal conductivity, κ. Thermal conductivity has two components, the thermal conductivity from electrons, κ_{el}, and that from phonons, or vibrations of the lattice, κ_{ph} (Equation 1.2):

$$\kappa = \kappa_{\text{el}} + \kappa_{\text{ph}} \tag{1.2}$$

These properties contribute to the performance of a material through the figure of merit, ZT, that can be used with the Carnot cycle to predict the ultimate efficiency of thermoelectric energy conversion (Equation 1.3):

$$\text{ZT} = \frac{S^2 \sigma T}{\kappa} \tag{1.3}$$

The performance of a thermoelectric material can be improved by increasing the numerator of Equation 1.3, where $S^2\sigma$ is referred to as the power factor, or by reducing the total thermal conductivity. In practice, optimization of ZT is challenging because, as the electrical conductivity of a material increases, the Seebeck coefficient tends to decrease while the thermal conductivity increases. If one considers doping of a semiconductor, peak ZT tends to occur at a relatively high charge carrier concentration but before the material reaches degeneracy.[41] Because each of the fundamental properties is temperature dependent, ZT will vary with temperature, leading to a peak temperature of performance.

Inorganic thermoelectric materials are commercially used in specialized power generation and cooling applications, but these materials are typically stiff, made from relatively rare elements, and can reach peak efficiency at high temperature.[41,42] The performance of inorganic materials, such as binary tellurides, chalcogenides, and skutterudites, has been improved by efforts to decrease their thermal conductivity while maintaining their electrical properties.[43,44] Strategies to decrease thermal conductivity by increased scattering of phonons include alloying and introduction of grain boundaries in polycrystalline samples.[41,45] Conversely, because polymeric thermoelectrics have lower thermal conductivity than inorganic materials in their insulating state, different approaches are necessary to optimize their thermoelectric performance.

Doping semiconducting polymers is necessary for fabricating thermoelectric devices. Foundational research on materials such as polyacetylene and polyaniline demonstrated that doped semiconducting polymers, also referred to as conducting polymers, can have high electrical conductivities (>1,000 S/cm).[46–49] The thermopowers of these polymers were examined mainly as a means to study the fundamental transport properties and were found to be relatively low (e.g., ~1 μV/K for highly conductive polyaniline). Their application as thermoelectric materials was not extensively explored due to issues with stability in the ambient. Recent work on the stable polymer poly(3,4-ethylenedioxythiophene) (PEDOT) has revealed relatively high thermopowers at electrical conductivities of ~100 S/cm in thin films, spurring the interest in the thermoelectric behavior of polymers.[50]

1.5. Summary

In this work, we study the interplay between electronic structure, chemical mechanism in morphology in three organic semiconductor and dopant systems. In Chapter 2, we study the

effects of 2+ oxidation states on the electronic density of states and charge transport in *p*-type small molecule films. In Chapter 3, we demonstrate a Lewis acid-base pair mechanism for *p*-type doping and investigate how this dopant combination affects the film morphology and the nature and delocalization of the resulting polarons. In Chapter 4, we propose a novel mechanism for *n*-type doping based on frustrated Lewis pairs and use computation and thermochemical analysis to demonstrate its potential feasibility. Overall, these studies show that changes in electronic structure and film morphology can be interrelated during doping and can both affect the transport properties of the material. Our work on using Lewis acids and bases for doping shows that exploring new doping mechanisms and dopant combinations may help to optimize dopant-semiconductor systems for future applications in electronic and energy conversion devices.

1.6. Rights and Permissions

Chapter 3 will be submitted as K. A. Peterson, M. L. Chabinyc, Lewis Acid-Base Pair Doping of *p*-Type Organic Semiconductors, *in preparation*.

1.7. References

1 G. Tu, A. Bilge, S. Adamczyk, M. Forster, R. Heiderhoff, L. J. Balk, D. Mühlbacher, M. Morana, M. Koppe, M. C. Scharber, S. A. Choulis, C. J. Brabec and U. Scherf, The Influence of Interchain Branches on Solid State Packing, Hole Mobility and Photovoltaic Properties of Poly(3-hexylthiophene) (P3HT), *Macromol. Rapid Commun.*, 2007, **28**, 1781–1785.

2 Z. Zhang and J. Wang, Structures and properties of conjugated Donor–Acceptor copolymers for solar cell applications, *J. Mater. Chem.*, 2012, **22**, 4178–87.

3 S. Ko, E. T. Hoke, L. Pandey, S. Hong, R. Mondal, C. Risko, Y. Yi, R. Noriega, M. D. McGehee, J.-L. Brédas, A. Salleo and Z. Bao, Controlled Conjugated Backbone Twisting for an Increased Open-Circuit Voltage while Having a High Short-Circuit Current in Poly(hexylthiophene) Derivatives, *J. Am. Chem. Soc.*, 2012, **134**, 5222–5232.

4 D. M. DeLongchamp, R. J. Kline, D. A. Fischer, L. J. Richter and M. F. Toney, Molecular Characterization of Organic Electronic Films, *Adv. Mater.*, 2011, **23**, 319–337.

5 R. Noriega, J. Rivnay, K. Vandewal, F. P. V. Koch, N. Stingelin, P. Smith, M. F. Toney and A. Salleo, A general relationship between disorder, aggregation and charge transport in conjugated polymers, *Nat. Mater.*, 2013, **12**, 1038–1044.

6 K. Gu, C. R. Snyder, J. Onorato, C. K. Luscombe, A. W. Bosse and Y.-L. Loo, Assessing the Huang–Brown Description of Tie Chains for Charge Transport in Conjugated Polymers, *ACS Macro Lett.*, 2018, **7**, 1333–1338.

7 A. Hamidi-Sakr, L. Biniek, J.-L. Bantignies, D. Maurin, L. Herrmann, N. Leclerc, P. Lévêque, V. Vijayakumar, N. Zimmermann and M. Brinkmann, A Versatile Method to Fabricate Highly In-Plane Aligned Conducting Polymer Films with Anisotropic Charge Transport and Thermoelectric Properties: The Key Role of Alkyl Side Chain Layers on the Doping Mechanism, *Adv. Funct. Mater.*, 2017, **27**, 1700173.

8 B. A. Collins, J. E. Cochran, H. Yan, E. Gann, C. Hub, R. Fink, C. Wang, T. Schuettfort, C. R. McNeill, M. L. Chabinyc and H. Ade, Polarized X-ray scattering reveals non-crystalline orientational ordering in organic films, *Nat. Mater.*, 2012, **11**, 536–543.

9 P. Wei, J. H. Oh, G. Dong and Z. Bao, Use of a 1 *H* -Benzoimidazole Derivative as an *n* -Type Dopant and To Enable Air-Stable Solution-Processed *n* -Channel Organic Thin-Film Transistors, *J. Am. Chem. Soc.*, 2010, **132**, 8852–8853.

10 B. D. Naab, S. Guo, S. Olthof, E. G. B. Evans, P. Wei, G. L. Millhauser, A. Kahn, S. Barlow, S. R. Marder and Z. Bao, Mechanistic Study on the Solution-Phase n-Doping of 1,3-Dimethyl-2-aryl-2,3-dihydro-1H-benzoimidazole Derivatives, *J. Am. Chem. Soc.*, 2013, **135**, 15018–15025.

11 S. Guo, S. B. Kim, S. K. Mohapatra, Y. Qi, T. Sajoto, A. Kahn, S. R. Marder and S. Barlow, n-Doping of Organic Electronic Materials using Air-Stable Organometallics, *Adv. Mater.*, 2012, **24**, 699–703.

12 I. Petsagkourakis, N. Kim, K. Tybrandt, I. Zozoulenko and X. Crispin, Poly(3,4-ethylenedioxythiophene): Chemical Synthesis, Transport Properties, and Thermoelectric Devices, *Adv. Electron. Mater.*, 2019, **5**, 1800918.

13 A. J. Heeger, Semiconducting and Metallic Polymers: The Fourth Generation of Polymeric Materials, *J. Phys. Chem. B*, 2001, **105**, 8475–8491.

14 R. Ghosh, C. M. Pochas and F. C. Spano, Polaron Delocalization in Conjugated Polymer Films, *J. Phys. Chem. C*, 2016, **120**, 11394–11406.

15 D. T. Scholes, P. Y. Yee, J. R. Lindemuth, H. Kang, J. Onorato, R. Ghosh, C. K. Luscombe, F. C. Spano, S. H. Tolbert and B. J. Schwartz, The Effects of Crystallinity on Charge Transport and the Structure of Sequentially Processed F4TCNQ-Doped Conjugated Polymer Films, *Adv. Funct. Mater.*, 2017, **27**, 1702654.
16 R. Ghosh, A. R. Chew, J. Onorato, V. Pakhnyuk, C. K. Luscombe, A. Salleo and F. C. Spano, Spectral Signatures and Spatial Coherence of Bound and Unbound Polarons in P3HT Films: Theory Versus Experiment, *J. Phys. Chem. C*, 2018, **122**, 18048–18060.
17 M. J. Nowak, D. Spiegel, S. Hotta, A. J. Heeger and P. A. Pincus, Charge storage on a conducting polymer in solution, *Macromolecules*, 1989, **22**, 2917–2926.
18 O. Bubnova, Z. U. Khan, H. Wang, S. Braun, D. R. Evans, M. Fabretto, P. Hojati-Talemi, D. Dagnelund, J.-B. Arlin, Y. H. Geerts, S. Desbief, D. W. Breiby, J. W. Andreasen, R. Lazzaroni, W. M. Chen, I. Zozoulenko, M. Fahlman, P. J. Murphy, M. Berggren and X. Crispin, Semi-metallic polymers, *Nat. Mater.*, 2013, **13**, 190–194.
19 G. Heimel, The Optical Signature of Charges in Conjugated Polymers, *ACS Cent. Sci.*, 2016, **2**, 309–315.
20 S. Schott, U. Chopra, V. Lemaur, A. Melnyk, Y. Olivier, R. D. Pietro, I. Romanov, R. L. Carey, X. Jiao, C. Jellett, M. Little, A. Marks, C. R. McNeill, I. McCulloch, E. R. McNellis, D. Andrienko, D. Beljonne, J. Sinova and H. Sirringhaus, Polaron spin dynamics in high-mobility polymeric semiconductors, *Nat. Phys.*, 2019, **15**, 814–822.
21 S. Wang, M. Ha, M. Manno, C. D. Frisbie and C. Leighton, Hopping transport and the Hall effect near the insulator–metal transition in electrochemically gated poly(3-hexylthiophene) transistors, *Nat. Commun.*, 2012, **3**, 1210.
22 I. E. Jacobs and A. J. Moulé, Controlling Molecular Doping in Organic Semiconductors, *Adv. Mater.*, 2017, **29**, 1703063.
23 T. F. Harrelson, Y. Q. Cheng, J. Li, I. E. Jacobs, A. J. Ramirez-Cuesta, R. Faller and A. J. Moulé, Identifying Atomic Scale Structure in Undoped/Doped Semicrystalline P3HT Using Inelastic Neutron Scattering, *Macromolecules*, 2017, **50**, 2424–2435.
24 I. E. Jacobs, E. W. Aasen, J. L. Oliveira, T. N. Fonseca, J. D. Roehling, J. Li, G. Zhang, M. P. Augustine, M. Mascal and A. J. Moulé, Comparison of solution-mixed and sequentially processed P3HT:F4TCNQ films: effect of doping-induced aggregation on film morphology, *J. Mater. Chem. C*, 2016, **4**, 3454–3466.
25 K. Kang, S. Watanabe, K. Broch, A. Sepe, A. Brown, I. Nasrallah, M. Nikolka, Z. Fei, M. Heeney, D. Matsumoto, K. Marumoto, H. Tanaka, S. Kuroda and H. Sirringhaus, 2D coherent charge transport in highly ordered conducting polymers doped by solid state diffusion, *Nat. Mater.*, 2016, **15**, 896–902.
26 E. Lim, K. A. Peterson, G. M. Su and M. L. Chabinyc, Thermoelectric Properties of Poly(3-hexylthiophene) (P3HT) Doped with 2,3,5,6-Tetrafluoro-7,7,8,8-tetracyanoquinodimethane (F4TCNQ) by Vapor-Phase Infiltration, *Chem. Mater.*, 2018, **30**, 998–1010.
27 P. Y. Yee, D. T. Scholes, B. J. Schwartz and S. H. Tolbert, Dopant-Induced Ordering of Amorphous Regions in Regiorandom P3HT, *J. Phys. Chem. Lett.*, 2019, **10**, 4929–4934.
28 B. Neelamraju, K. E. Watts, J. E. Pemberton and E. L. Ratcliff, Correlation of Coexistent Charge Transfer States in F_4TCNQ-Doped P3HT with Microstructure, *J. Phys. Chem. Lett.*, 2018, **9**, 6871–6877.
29 Z. Liang, Y. Zhang, M. Souri, X. Luo, A. M. Boehm, R. Li, Y. Zhang, T. Wang, D.-Y. Kim, J. Mei, S. R. Marder and K. R. Graham, Influence of dopant size and electron affinity

on the electrical conductivity and thermoelectric properties of a series of conjugated polymers, *J. Mater. Chem. A*, 2018, **6**, 16495–16505.
30 T. J. Aubry, J. C. Axtell, V. M. Basile, K. J. Winchell, J. R. Lindemuth, T. M. Porter, J.-Y. Liu, A. N. Alexandrova, C. P. Kubiak, S. H. Tolbert, A. M. Spokoyny and B. J. Schwartz, Dodecaborane-Based Dopants Designed to Shield Anion Electrostatics Lead to Increased Carrier Mobility in a Doped Conjugated Polymer, *Adv. Mater.*, 2019, **31**, 1805647.
31 J. Gao, J. D. Roehling, Y. Li, H. Guo, A. J. Moulé and J. K. Grey, The effect of 2,3,5,6-tetrafluoro-7,7,8,8-tetracyanoquinodimethane charge transfer dopants on the conformation and aggregation of poly(3-hexylthiophene), *J. Mater. Chem. C*, 2013, **1**, 5638.
32 E. Lim, A. M. Glaudell, R. Miller and M. L. Chabinyc, The Role of Ordering on the Thermoelectric Properties of Blends of Regioregular and Regiorandom Poly(3-hexylthiophene), *Adv. Electron. Mater.*, 2019, **5**, 1800915.
33 K.-H. Yim, G. L. Whiting, C. E. Murphy, J. J. M. Halls, J. H. Burroughes, R. H. Friend and J.-S. Kim, Controlling Electrical Properties of Conjugated Polymers via a Solution-Based p-Type Doping, *Adv. Mater.*, 2008, **20**, 3319–3324.
34 E. M. Thomas, E. C. Davidson, R. Katsumata, R. A. Segalman and M. L. Chabinyc, Branched Side Chains Govern Counterion Position and Doping Mechanism in Conjugated Polythiophenes, *ACS Macro Lett.*, 2018, **7**, 1492–1497.
35 I. E. Jacobs, C. Cendra, T. F. Harrelson, Z. I. Bedolla Valdez, R. Faller, A. Salleo and A. J. Moulé, Polymorphism controls the degree of charge transfer in a molecularly doped semiconducting polymer, *Mater. Horiz.*, 2018, **5**, 655–660.
36 E. F. Aziz, A. Vollmer, S. Eisebitt, W. Eberhardt, P. Pingel, D. Neher and N. Koch, Localized Charge Transfer in a Molecularly Doped Conducting Polymer, *Adv. Mater.*, 2007, **19**, 3257–3260.
37 A. Zevalkink, D. M. Smiadak, J. L. Blackburn, A. J. Ferguson, M. L. Chabinyc, O. Delaire, J. Wang, K. Kovnir, J. Martin, L. T. Schelhas, T. D. Sparks, S. D. Kang, M. T. Dylla, G. J. Snyder, B. R. Ortiz and E. S. Toberer, A practical field guide to thermoelectrics: Fundamentals, synthesis, and characterization, *Appl. Phys. Rev.*, 2018, **5**, 021303.
38 J.-H. Bahk, H. Fang, K. Yazawa and A. Shakouri, Flexible thermoelectric materials and device optimization for wearable energy harvesting, *J. Mater. Chem. C*, 2015, **3**, 10362–10374.
39 M. Magliulo, M. Y. Mulla, M. Singh, E. Macchia, A. Tiwari, L. Torsi and K. Manoli, Printable and flexible electronics: from TFTs to bioelectronic devices, *J. Mater. Chem. C*, 2015, **3**, 12347–12363.
40 B. Russ, A. Glaudell, J. J. Urban, M. L. Chabinyc and R. A. Segalman, Organic thermoelectric materials for energy harvesting and temperature control, *Nat. Rev. Mater.*, 2016, **1**, 16050.
41 G. J. Snyder and E. S. Toberer, Complex thermoelectric materials, *Nat. Mater.*, 2008, **7**, 105–114.
42 A. Shakouri, Recent Developments in Semiconductor Thermoelectric Physics and Materials, *Annu. Rev. Mater. Res.*, 2011, **41**, 399–431.
43 B. C. Sales, D. Mandrus and R. K. Williams, Filled Skutterudite Antimonides: A New Class of Thermoelectric Materials, *Science*, 1996, **272**, 1325–1328.

44 D. A. Wright, Thermoelectric Properties of Bismuth Telluride and its Alloys, *Nature*, 1958, **181**, 834–834.
45 C. J. Vineis, A. Shakouri, A. Majumdar and M. G. Kanatzidis, Nanostructured Thermoelectrics: Big Efficiency Gains from Small Features, *Adv. Mater.*, 2010, **22**, 3970–3980.
46 C. K. Chiang, C. R. Fincher, Y. W. Park, A. J. Heeger, H. Shirakawa, E. J. Louis, S. C. Gau and A. G. MacDiarmid, Electrical Conductivity in Doped Polyacetylene, *Phys. Rev. Lett.*, 1977, **39**, 1098–1101.
47 R. McNeill, R. Siudak, J. H. Wardlaw and D. E. Weiss, Electronic Conduction in Polymers. I. The Chemical Structure of Polypyrrole, *Aust. J. Chem.*, 1963, **16**, 1056–1075.
48 B. A. Bolto and D. E. Weiss, Electronic Conduction in Polymers. II. The Electrochemical Reduction of Polypyrrole at Controlled Potential, *Aust. J. Chem.*, 1963, **16**, 1076–1089.
49 B. A. Bolto, R. McNeill and D. E. Weiss, Electronic Conduction in Polymers. III. Electronic Properties of Polypyrrole, *Aust. J. Chem.*, 1963, **16**, 1090–1103.
50 O. Bubnova, Z. U. Khan, A. Malti, S. Braun, M. Fahlman, M. Berggren and X. Crispin, Optimization of the thermoelectric figure of merit in the conducting polymer poly(3,4-ethylenedioxythiophene), *Nat. Mater.*, 2011, **10**, 429–433.
51 K. A. Peterson, E. M. Thomas and M. L. Chabinyc, Thermoelectric Properties of Semiconducting Polymers, *Annu. Rev. Mater. Res.*, 2020, **50**, 551–574.

2. Charge Transport in Vapor Doped Small Molecule Films

2.1. Introduction

Small molecule organic semiconductors have become widely used in organic light emitting devices (OLEDs) for information displays.[1] Small molecules can be thermally evaporated to form smooth, glassy layers in devices. Amorphous films of organic semiconductors can also be cast from solvent and are used frequently as electron and hole transport layers in devices such as thin film solar cells.[2,3] Doping of such transport layers is particularly beneficial to modify their electrical conductivity and to control the energetic line-up of transport levels at interfaces. The role of dopants on the structural ordering of amorphous materials has not been extensively studied,[4] particularly if there is aggregation induced by charge transfer interactions.

Amorphous small molecule semiconductor films have been found to follow an Arrhenius-type thermally activated hopping conduction model.[5] The conductivity, σ, is given by Eq. 2.1 where σ_0 is the conductivity at infinite temperature with all carriers activated, E_a is the hopping activation energy, k_B is the Boltzmann constant, and T is the temperature.

$$\sigma = \sigma_0 \exp\left(\frac{-E_a}{k_B T}\right) \tag{2.1}$$

While Eq. 2.1 describes hopping conduction well, it does not provide any insight into the shape of the density of states (DOS) of an amorphous semiconducting material. The DOS of amorphous molecular semiconductors is usually modeled with a Gaussian form, but the changes in the shape of the DOS with doping are not well understood. Arkhipov, et al. proposed a DOS model where a Gaussian distribution of host states is broadened by an

exponential tail of trap states.[6] However, this model is only formulated for dopant concentrations up to 10^{18} – 10^{19} cm^{-3}. Recent research on doped small molecule semiconductors has suggested that, at higher dopant concentrations, dopants no longer act as Coulombic traps.[7] The charge transfer between the host molecules and dopants causes the ionized hosts and dopants to form integer charge transfer complexes (ICTCs) bound with Coulomb forces. This Coulomb interaction modifies the energy level of the ionized host molecules. At 10 mol% doping, the concentration of ICTCs is high enough that carriers will preferentially hop among the Coulomb-modified ICTC states. These distributions of ICTC states were described by the width of their static disorder, σ_{ICTC}. E_a was found to be related to both σ_{ICTC} and the relaxation energy of the host molecule after ionization.[7] Kinetic Monte Carlo simulations have also treated the DOS of small molecule semiconductors as two distributions of states, neutral host states and ionized host states. The conductivity of some small molecule semiconductors increases superlinearly with doping,[8,9] and these simulations found that a reduction in disorder from adding dopants may explain this superlinear increase.[10]

One example of a solution-processable small molecule semiconductor that forms amorphous films is 2,2',7,7'-tetrakis[N,N-di(4-methoxyphenyl)amino]-9,9'-spirobifluorene (spiro-OMeTAD) (Figure 2.1a). This material is commonly used as a hole transport layer in perovskite solar cells[3,11] and dye sensitized solar cells.[12,13] In solar cells, spiro-OMeTAD is typically doped with LiTFSI, tert-butylpyridine, and oxygen to a conductivity ~10^{-5} S/cm at 12-30 mol% LiTFSI.[14] As shown in Figure 1a, the core of the spiro-OMeTAD molecule has two fluorene units connected by a spiro-bridged carbon atom. Because of this spiro bridge, the two fluorene units are perpendicular to each other, and the molecular structure frustrates crystallization in thin films. Spiro-OMeTAD can be crystallized, leading to a triclinic $P\bar{1}$

structure with only short-range π-π overlap between adjacent molecules.[15,16] The spiro-bridge also leads to a unique electronic structure relative to other materials. Density functional theory (DFT) calculations using the long-range corrected hybrid functional ωB97X-D reveal that the HOMO and HOMO-1 orbitals of spiro-OMeTAD in the experimental geometry from a single crystal structure are nearly degenerate and localize onto opposite sides of the spiro bridge.[15,16] Our ωB97X-D/6-31G(d) calculations on an isolated molecule in vacuum without symmetry constraints show similar localization of the HOMO and HOMO-1 on the asymmetric structure that is likely present in amorphous films (Figure 2.1b). Such long-range corrected hybrid DFT functionals are helpful to more accurately model the electronic structure of mixed-valence spiro compounds than functionals such as B3LYP that overly delocalize and mix the molecular orbitals.[17] The impact of this near degeneracy on charge transport has not been examined in detail.

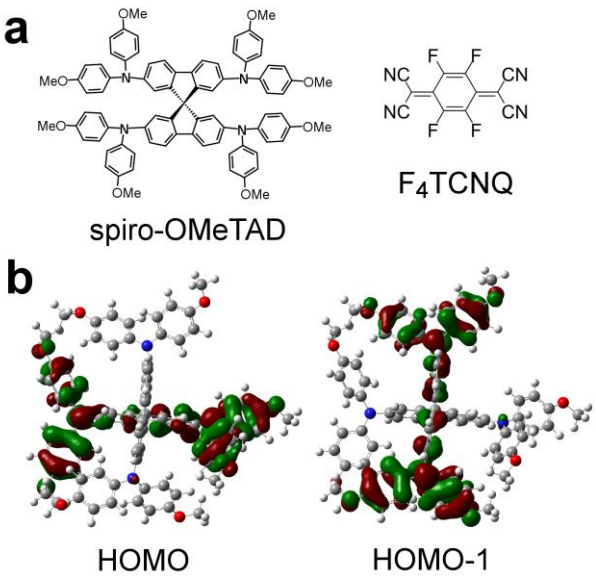

Figure 2.1. (a) Chemical structure of spiro-OMeTAD and F_4TCNQ and (b) DFT calculations of spiro-OMeTAD's nearly degenerate HOMO and HOMO-1. Perpendicular fluorene units are both seen edge-on in (b).

Here we examine spiro-OMeTAD as a model system to study charge transport in amorphous small molecule semiconductor films at high carrier concentrations. It has the advantage of being readily cast from solution into amorphous thin films and has a unique electronic structure relative to many molecular semiconductors. We doped spiro-OMeTAD films with small molecule dopant 2,3,5,6-tetrafluoro-7,7,8,8-tetracyanoquinodimethane (F_4TCNQ) by infiltration from the vapor phase leading to a maximum of 39 ± 2 mol% F_4TCNQ films. The electron affinity of F_4TCNQ at 5.24 eV[18] is close to Spiro-OMeTAD's first and second ionization energies, ≈5.1 - 5.3 eV.[12] This close energy match between the dopant and host allowed us to study the effects of spiro-OMeTAD's two hopping sites on the material's electronic transport. We found that Seebeck coefficient and temperature-dependent conductivity measurements are consistent with a Gaussian density of charged states modified by the presence of spiro-OMeTAD^{2+} states.

2.2. Experimental Methods

2.2.1 Sample Preparation

All materials were used as received. Spiro-OMeTAD (Lumtec) films were spun cast on cleaned quartz substrates from 170 mg/mL solution in chlorobenzene (Sigma Aldrich, anhydrous, 99.8%) at 2000 rpm/s for 45 s under N_2 atmosphere. Gold contacts (80 nm) were evaporated on films for conductivity or Seebeck measurements through a shadow mask. Substrates were attached with tape to the lid of a glass doping chamber with F_4TCNQ (TCI America) in the bottom. The doping chamber was heated on a hot plate at 200 °C in N_2 atmosphere to diffuse F_4TCNQ vapor into the films. Films were annealed at 150 °C for 10 min. To measure the undoped spiro-OMeTAD thermal diffusivity, a pink-dyed film was prepared by blade-coating a chlorobenzene solution containing 1.4 mg/mL Oil Red O (Sigma

Aldrich) and 162 mg/mL spiro-OMeTAD on a quartz substrate at 60 °C for an intended 5 mol% Oil Red O film.

2.2.2 Physical Characterization

Film thicknesses were measured on a Bruker DektakXT stylus profilometer. SIMS was performed on a Cameca IMS 7f Auto SIMS with oxygen ion source. GIWAXS was performed at beamline 11-3 at the Stanford Synchrotron Radiation Lightsource, SLAC National Accelerator Laboratory. GIWAXS samples were prepared on native oxide silicon substrates. X-ray incident angle was 0.1°, sample-detector distance was 315 mm, and exposure time was 350-400 s. GIWAXS data was processed using IgorPro packages Nika[*] and WAXStools.[†]

2.2.3 Spectroscopic Characterization

UV-Vis-NIR film spectra were collected on a Shimadzu UV3600 or PerkinElmer Lambda 750 spectrometer.

2.2.4 Charge Transport Measurements

Room-temperature conductivity was measured under N_2 atmosphere using the four-point probe method with a Keithley 6220 precision current source and Keithley 2400. Low-temperature conductivity was measured under vacuum in a liquid nitrogen-cooled LakeShore Cryotonics TTP probe station. Low-temperature conductivity was measured using the transmission line method with a Keithley 6487 picoammeter. In-plane Seebeck coefficient was measured at room temperature under N_2 atmosphere with a custom probe station. The sample was placed across two Peltier elements that were alternately cooled to create a

[*] J. Ilavsky, Nika: software for two-dimensional data reduction, J. Appl. Cryst., 2012, 45, 324–328.

[†] S. D. Oosterhout, V. Savikhin, J. Zhang, Y. Zhang, M. A. Burgers, S. R. Marder, G. C. Bazan and M. F. Toney, Mixing Behavior in Small Molecule:Fullerene Organic Photovoltaics, *Chem. Mater.*, 2017, **29**, 3062–3069.

temperature gradient across the film. The temperature gradient was measured by type T thermocouples on the sample surface with a Fluke 1529 Chub E-4, and the potential gradient was measured with a Keithley 2400.

2.2.5 Thermal Diffusivity

Thermal diffusivity was measured with the transient grating technique on spiro-OMeTAD films on quartz substrates. Extensive details of the transient grating technique can be found in Reference 35. Briefly, a pulsed laser beam at 515 nm from a Yb-doped fiber laser (Clark-MRX IMPULSE) is split by a phase mask and recombined by a confocal imaging system onto the sample surface to form a one-dimensional optical intensity grating. This intensity grating is absorbed by the spiro-OMeTAD film, creating a temperature change with a sinusoidal spatial profile, or a "temperature grating." The decay of the amplitude of this "temperature grating" in time is monitored by the diffraction of a continuous-wave laser (532 nm), which is detected by a fast photodiode (Hamamatsu C5658) and an oscilloscope (Tektronix TDS 784A). This real-time decay signal is analyzed using a thermal transport model, from which the thermal diffusivity of the spiro-OMeTAD films can be extracted.

Heat capacity was measured on a powder sample of spiro-OMeTAD with a TA Instruments Q2000 differential scanning calorimeter. The sample was subjected to three melting-cooling cycles before measuring the reversing heat capacity during a modulated heating from 15 to 35 °C with a modulation of ±1 °C every 100 s.

2.2.6 Computational Methods

Geometry of spiro-OMeTAD was optimized at the 6-31G(d)/ωB97-XD level without symmetry constraints using the default value of ω (0.2 $Bohr^{-1}$) in Gaussian 16.[‡]

[‡] Gaussian 16, Revision C.01, M. J. Frisch, G. W. Trucks, H. B. Schlegel, G. E. Scuseria, M. A. Robb, J. R. Cheeseman, G. Scalmani, V. Barone, G. A. Petersson, H. Nakatsuji, X. Li, M. Caricato, A. V. Marenich, J.

2.3. Results and Discussion

We doped spun-cast spiro-OMeTAD films by diffusing F_4TCNQ vapor into the films, or "vapor doping" them with F_4TCNQ. We and others have previously used this vapor-doping process to dope semiconducting polymers, including PBTTT and P3HT,[19,20] but we are not aware of its use for molecular systems. Vapor doping differs from methods, such as thermal co-evaporation of host and dopant molecules or spin casting of doped solutions. Casting the neutral semiconductor prior to the doping process eliminates difficulties in the solubilization of the doped form of the semiconductor and its associated counterion that can preclude achieving high levels of doping. For the vapor doping process, the spiro-OMeTAD films were placed face-down in the top of a doping chamber in a N_2 atmosphere glovebox. A small amount of F_4TCNQ was placed in the bottom of the doping chamber. When the doping chamber is heated on a hot plate at 200 °C, the F_4TCNQ sublimates and can diffuse into the film. The glass transition temperature, T_g, of spiro-OMeTAD is relatively high at 124 °C.[21] In our apparatus, the substrate temperature is not fixed and after 15 min of heating, the substrate reaches 92.5 °C, and ~106 °C after 90 min of heating, so T_g of spiro-OMeTAD is never exceeded during the doping process (See Supplementary Information for full heating curve).

Bloino, B. G. Janesko, R. Gomperts, B. Mennucci, H. P. Hratchian, J. V. Ortiz, A. F. Izmaylov, J. L. Sonnenberg, D. Williams-Young, F. Ding, F. Lipparini, F. Egidi, J. Goings, B. Peng, A. Petrone, T. Henderson, D. Ranasinghe, V. G. Zakrzewski, J. Gao, N. Rega, G. Zheng, W. Liang, M. Hada, M. Ehara, K. Toyota, R. Fukuda, J. Hasegawa, M. Ishida, T. Nakajima, Y. Honda, O. Kitao, H. Nakai, T. Vreven, K. Throssell, J. A. Montgomery, Jr., J. E. Peralta, F. Ogliaro, M. J. Bearpark, J. J. Heyd, E. N. Brothers, K. N. Kudin, V. N. Staroverov, T. A. Keith, R. Kobayashi, J. Normand, K. Raghavachari, A. P. Rendell, J. C. Burant, S. S. Iyengar, J. Tomasi, M. Cossi, J. M. Millam, M. Klene, C. Adamo, R. Cammi, J. W. Ochterski, R. L. Martin, K. Morokuma, O. Farkas, J. B. Foresman, and D. J. Fox, Gaussian, Inc., Wallingford CT, 2016.

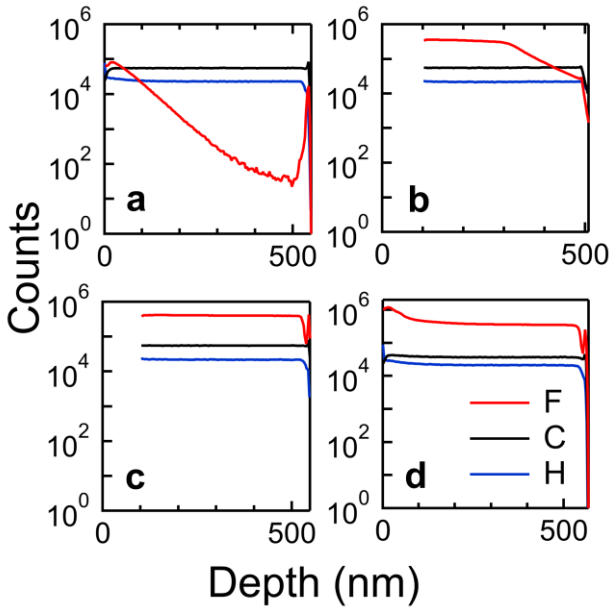

Figure 2.2. Secondary ion mass spectroscopy plots tracking the depth distribution of fluorine (red), carbon (black), and hydrogen (blue) in spiro-OMeTAD films vapor doped with F4TCNQ for (a) 15 min, (b) 30 min, (c) 45 min, and (d) 30 min with 10 min annealing. Spikes in the plots at the bottom of the film are an artefact caused by the primary ion beam hitting the insulating quartz substrates.

We determined whether F_4TCNQ had diffused through the full depth of the film during vapor doping using secondary ion mass spectroscopy (SIMS). Fluorine atoms provide a unique maker for the presence of F_4TCNQ; we note that due to the high fluorine signal level, the amount of F_4TCNQ could not be accurately quantified relative to other atoms using our SIMS instrument. In Figure 2.2a, 15 min of vapor doping leads to a concentration profile where the concentration of F_4TCNQ is greatest near the surface of the film and decreases to the instrument noise level at the bottom of the film. After 30 min of vapor doping, Figure 2.2b, F_4TCNQ has nearly diffused through the full depth of the film. F_4TCNQ can fully diffuse through the film with a roughly even concentration profile after 45 min of vapor doping, as seen in Figure 2.2c. To test whether the uneven concentration profiles caused by vapor doping could be leveled through annealing, we annealed a 30 min vapor doped film for 10 min at 140 °C. This annealing temperature was chosen because it is above spiro-OMeTAD's glass transition temperature of 124 °C but below the temperature at which F_4TCNQ sublimes from

films, 150 °C.[22] Figure 2.2d shows that the concentration profile of the annealed film was more even at the bottom of the film than the unannealed film (Figure 2.2b). Ten minutes was long enough for F_4TCNQ to diffuse through the film without much de-doping but was not long enough for the film to crystallize. In the 45 and 75 min doped films, crystallization was observed around the edges of the film after annealing. Films used for charge transport measurements were annealed to reduce concentration gradients, and partially crystallized areas of annealed films were not measured.

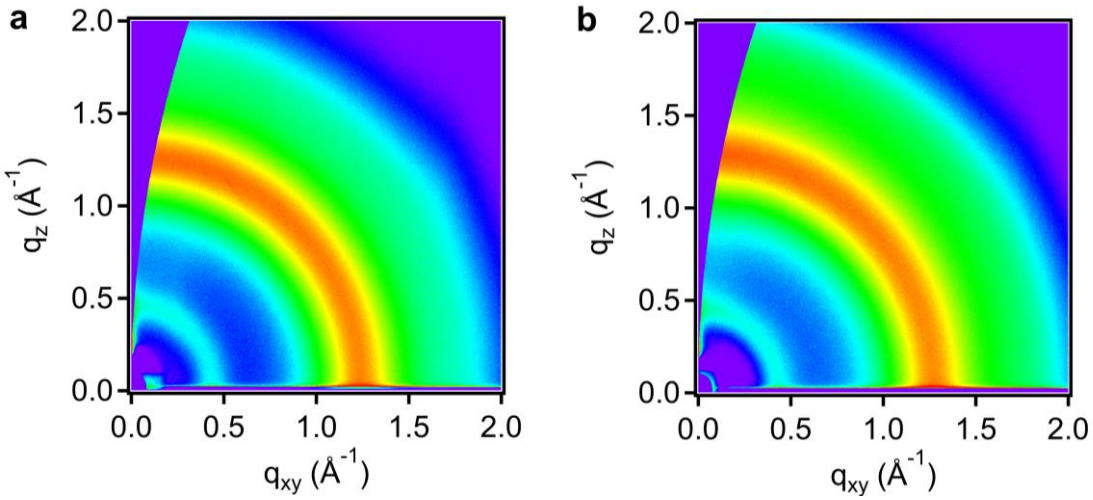

Figure 2.3. Grazing incidence wide angle X-ray scattering images of (a) neat and (b) 80 min F4TCNQ vapor doped spiro-OMeTAD.

We used grazing incidence wide angle X-ray scattering (GIWAXS) to determine if either spiro-OMeTAD or F4TCNQ crystallized (or co-crystallized) during the doping procedure. In the scattering from the undoped film, Figure 2.3a, a broad, nearly isotropic ring of scattering was observed around $q \approx 1.25$ Å^{-1}. This indicates that the film has an amorphous structure, as expected for spiro-OMeTAD, which is known to generally form glassy films. In Figure 2.3b, the scattering for an 80 min F_4TCNQ vapor doped film showed a similar, nearly isotropic scattering pattern and no signatures of scattering at *d*-spacings known for crystalline form of F_4TCNQ.[23] Because this 80 min doping time is higher than the doping times used for

charge transport measurements, this scattering indicates that the doped films retain their amorphous structure throughout the vapor doping process, as opposed to forming a co-crystal or phase separating.

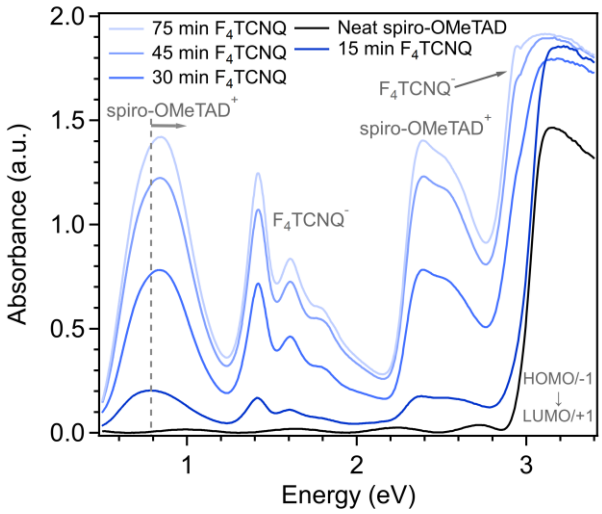

Figure 2.4. UV-Vis-NIR spectra of undoped (black) and doped (shades of blue) spiro-OMeTAD films. New peaks in the visible and NIR regions of the doped film spectra indicate the presence of F4TCNQ anions and spiro-OMeTAD cations (labeled in gray) and confirm integer charge transfer in the films.

To understand the nature of the charge transfer process between spiro-OMeTAD and F_4TCNQ, we measured the UV-Vis-NIR absorbance as a function of doping time (Figure 2.4). The absorbance spectrum of undoped spiro-OMeTAD has an onset around 3 eV with weak sub-optical gap features in the spectrum due to interference effects from the ~500 nm thick film. Upon doping, new features were observed in the spectra that confirm that integer charge transfer (ICT) occurred between F_4TCNQ and spiro-OMeTAD. Two spectra regions have features that can be assigned to the F_4TCNQ anion: the vibronic series between 1.3 – 2 eV and the peak at 2.9 eV.[24] The features centered around 0.8 eV and 2.5 eV can be assigned to transitions of spiro-OMeTAD$^+$ or spiro-OMeTAD^{2+}. Spiro-OMeTAD$^+$ and spiro-OMeTAD^{2+} have an additional weak transition centered at 1.77 eV.[25] In our spectra, that peak is obscured by the stronger F_4TCNQ anion absorbance. Due to the degenerate HOMO and HOMO-1 of

spiro-OMeTAD, spiro-OMeTAD^{+} still has a transition at 3 eV. At high doping levels, the feature centered around 0.8 eV becomes less symmetric and shows a blueshift. This blueshift suggests that some population of spiro-OMeTAD molecules has been oxidized to the 2+ state by two F_4TCNQ molecules. The energy gap between the HOMO-1 and HOMO levels was calculated to shift from 0.37 to 0.95 eV when spiro-OMeTAD^{+} is oxidized to the 2+ triplet state.[26] Because spiro-OMeTAD is a mixed-valence compound with two degenerate oxidation states, spiro-OMeTAD^{2+} may be in a triplet state or an open-shell singlet state.

Because spiro-OMeTAD and F_4TCNQ undergo integer charge transfer, we used UV-Vis-NIR spectra to estimate the charge carrier concentration in the doped films. In disordered organic semiconductors with hopping conduction, the carrier concentration cannot be measured readily using the Hall effect. Instead, we used the absorbance of F_4TCNQ^{-} to estimate the hole concentration. The area under the F_4TCNQ^{-} peaks between 1.25 – 2.15 eV is proportional to the concentration of F_4TCNQ^{-} anions in the films. We fit the three F_4TCNQ^{-} peaks and the spiro-OMeTAD^{+} transition at 1.77 eV to determine the area of the F_4TCNQ^{-} absorbance. We used reference spectra of $[Cp^{*}_2Co][F_4TCNQ]$ and $[Cp^{*}_2Fe][F_4TCNQ]$ solutions to calculate a reference value of the molar extinction coefficient, ε of the F_4TCNQ^{-} optical absorbance. With the F_4TCNQ^{-} absorbance, film thickness, and molar extinction coefficient, the concentration of F_4TCNQ^{-} in each film can be calculated. (See SI for full description of fitting methods) The number of F_4TCNQ^{-} is equivalent to the number of electrons removed from spiro-OMeTAD and spiro-OMeTAD^{+}. The UV-Vis spectra cannot easily be used to distinguish the relative amounts of spiro-OMeTAD+ and spiro-OMeTAD^{2+}, therefore it is difficult to measure how the holes are distributed on the two possible oxidation sites of a spiro-OMeTAD molecule. While some spiro-OMeTAD^{+} polarons could condense

to spiro-OMeTAD^{2+} bipolarons, the shape of the NIR peak suggests that both could be present in the doped films.

On average, films doped to our maximum doping time of 75 min reached a carrier concentration of 3.3 ± 0.3 x 10^{20} cm^{-3}, which is estimated to correspond to a film composition of 39 ± 2 mol% F_4TCNQ based on the concentration of F_4TCNQ^- determined by UV-Vis and the density of spiro-OMeTAD films.[27] (see Supplementary Information for details) Because the vapor doping process adds mass to the spiro-OMeTAD films, the thickness or density of the films can change. We found that film thicknesses increased from ≈420 ± 20 nm for undoped films to ≈530 ± 30 nm for films doped for 45 and 75 min. With this increase in film thickness, the density of spiro-OMeTAD hopping sites would decrease. Based on a spiro-OMeTAD film density of 1.02 g/cm^3,[27] the molecule density of spiro-OMeTAD films is 5.02 x 10^{20} cm^{-3}. Because the HOMO and HOMO-1 of spiro-OMeTAD are nearly degenerate, each molecule has two potential electronic states, giving a hopping site density of 1 x 10^{21} cm^{-3}.

We measured the room temperature conductivity of several samples with different doping levels. We found that the conductivity generally increases with doping level, with a maximum of 0.017 S/cm (Figure 2.5). This value is two orders of magnitude higher than the conductivity reached by typical LiTFSI doping[14] and similar to the 0.024 S/cm reported for LiTFSI and benzoyl peroxide doping.[28] Estimating with $\sigma = qp\mu$, we found that the electrical mobility may decrease but remains on the order of 10^{-4} $cm^2/V{\cdot}s$. (see Supplementary Information Figure S1.8) The mobility of these films cannot be measured directly because they are too disordered for Hall effect measurements, and field-effect transistor and space charge limited current (SCLC) mobility measurements are not accurate on highly doped films. For comparison, the Mott-Gurney SCLC mobility of undoped glassy spiro-OMeTAD was 2.3

x 10^{-4} $cm^2/V{\cdot}s$.[29] Many doped small molecule systems show a superlinear increase in conductivity with doping, such as MeO-TPD:F_6TCNNQ's increase over a dopant:host density ratio range of 0.01 – 0.29.[9] In our measurements of spiro-OMeTAD:F_4TCNQ, the increase in conductivity with hole concentration is no greater than linear, which could be attributed to this decrease in hole mobility.

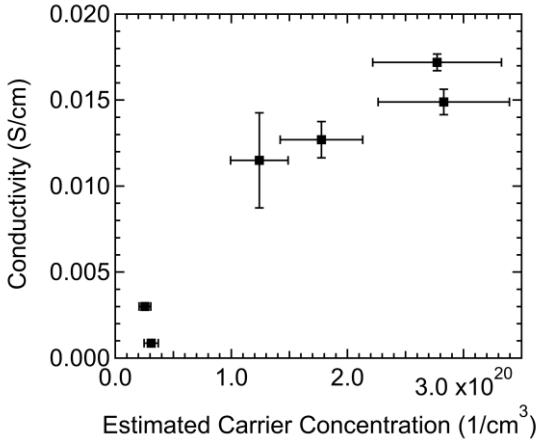

Figure 2.5. Room temperature conductivity increases with the estimated carrier concentration in the spiro-OMeTAD:F4TCNQ films. The error in the conductivity is the standard deviation of three measurements taken at different locations of the same film. The error in the carrier concentration is estimated at 20%.

To find the activation energy of hopping, E_a, in this system, we measured the conductivity of films with varying doping levels over a temperature range of at least 140 – 295 K (see Supplementary Information Figure S1.9). The dependence of the electrical conductivity on temperature followed the Arrhenius relationship of Eq. 2.1 with a nearly constant $E_a \approx 170$ meV (Figure 2.6). E_a decreases with increasing doping level and can level off at high doping levels.[7] The constant (or slightly decreasing) trend of E_a in this carrier concentration range is consistent with E_a leveling off at high doping levels. A broad range of *p*-type materials has been reported to have E_a values 171 – 295 meV.[7] Our measurements of E_a were on films with greater than 10 mol% doping, but spiro-OMeTAD:F_4TCNQ is among the systems with lower E_a values. For comparison, 2,2',7,7'-tetrakis(*N*,*N*-diphenylamino)-9.9-

spirobifluorene (spiro-TAD):F_6TCNNQ system has similar physical and electronic properties to spiro-OMeTAD:F_4TCNQ and its E_a is 180 meV at 10 mol% doping.[30] Both spiro-TAD:F_6TCNNQ and spiro-OMeTAD:F_4TCNQ have very small host IE-dopant EA offsets ~0.1 eV. Interestingly the electrical conductivity of spiro-OMeTAD:F_4TCNQ is significantly higher than that of spiro-TAD:F_6TCNNQ despite the comparable value of E_a.

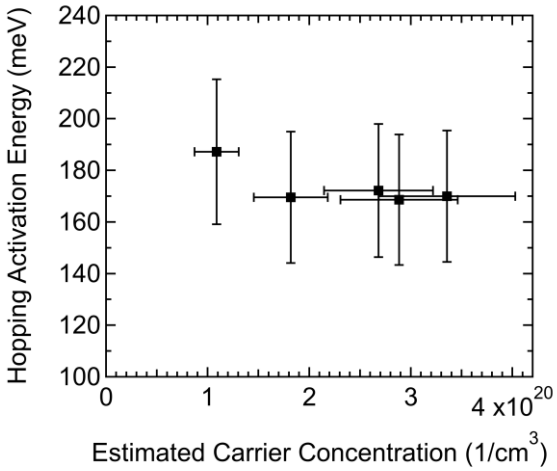

Figure 2.6. Hopping activation energy (E_a) was roughly constant with carrier concentration in this range. Error in E_a was estimated at 15%, while error in the carrier concentration was estimated at 20%.

One model proposes that electrical conduction in highly doped small molecule organic semiconductors primarily takes place among host-dopant charge transfer complexes, which form a DOS with width σ_{ICTC}.[7] Based on data from a wide variety of *p*- and *n*-type host:dopant systems at 10 mol% doping, a relationship between σ_{ICTC} determined by ultraviolet photoemission spectroscopy (UPS) and E_a, as well as the material's carrier density, was determined. Using the reported empirical relationship between E_a and σ_{ICTC}, doped films of spiro-OMeTAD are expected to have a low σ_{ICTC}. Spiro-OMeTAD has a low molecular density in doped films of 5 x 10^{20} cm^{-3}, similar to other materials that are reported to have a low σ_{ICTC}. The roughly constant E_a of spiro-OMeTAD:F_4TCNQ over this doping range

suggests that the σ_{ICTC} disorder in the system is roughly constant over this doping range, as well.

We measured the in-plane Seebeck coefficient, S, of the doped spiro-OMeTAD films with varying carrier concentrations at room temperature to assess how the shape of the electronic DOS changes with doping (Figure 2.7a). Because spiro-OMeTAD has two potential sites for charge hopping, it is of interest to determine if there are signs that both oxidation states are involved in charge transport. The Seebeck coefficient is related to the shape of the DOS through the Mott formalism,[31]

$$S = -\frac{k_B}{e}\int\left(\frac{E - E_{\mathrm{F}}}{k_B T}\right)\frac{\sigma_E}{\sigma}\left(\frac{\partial f}{\partial E}\right)\mathrm{d}E \tag{2.2}$$

where σ_{E} is the transport function, e is the electronic charge, E is energy, E_{F} is the Fermi energy, and f is the Fermi function. In hopping semiconductors, Eq. 2.2 becomes,

$$S = \frac{k_{\mathrm{B}}}{e}\left(\frac{E_{\mathrm{tr}} - E_{\mathrm{F}}}{k_{\mathrm{B}} T}\right) \tag{2.3}$$

where E_{tr} is the transport energy. In a *p*-type Gaussian DOS, E_{tr} is at an energy slightly above the peak of the DOS. The Seebeck coefficient will increase when the distance between E_{tr} and E_F increases.[32]

We found that S was roughly constant in this carrier concentration range with a small increase at high carrier concentrations ≈2.8 x 10^{20} cm^{-3}. The three points below 2 x 10^{20} cm^{-3} have an average value of 119 μV/K, while the values at higher concentrations are 156 and 167 μV/K. Typically, the Seebeck coefficient of small molecule semiconductors decreases with increasing dopant concentration.[9] Because the Seebeck constant is related to the distance between E_{tr} and E_F by Eq. 2.3, E_{tr}-E_F in spiro-OMeTAD:F_4TCNQ may have increased at ≈2.8 x 10^{20} cm^{-3}. The increase in E_{tr}-E_F could be caused by a change in DOS shape by spiro-

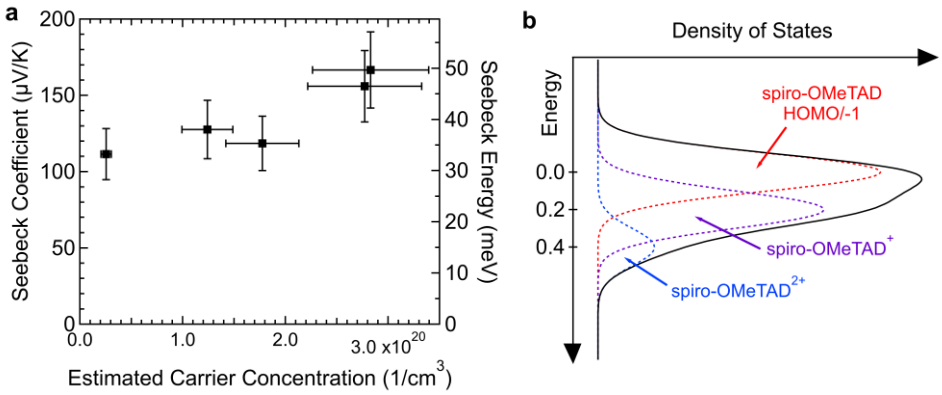

Figure 2.7. (a) In-plane Seebeck coefficient was generally constant over this carrier concentration range but increased slightly at ≈2.8 x 1020 1/cm3. Error in the Seebeck coefficient measurement was estimated at 15%, while the estimated error in the carrier concentration was 20%. (b) Schematic the electronic DOS of doped spiro-OMeTAD showing the estimated energies to remove an electron from the neutral molecule, spiro-OMeTAD+ and spiro-OMeTAD2+. These states are close enough in energy that the DOS of states is likely broadened by ionized states at high levels of doping. This schematic assumes Gaussian widths of 0.1 eV spaced 0.2 eV apart.

$OMeTAD^{2+}$ states. Upon doping, a Gaussian density of spiro-$OMeTAD^{+}$ states forms that overlaps with the Gaussian DOS of spiro-OMeTAD. As the carrier concentration increases, it is possible that bipolarons could form, further extending the tail of the DOS and potentially increasing E_{tr}-E_F. This mechanism of increasing the Seebeck coefficient has been observed and modeled in polymer blends.[32,33] Figure 2.7b shows a schematic of how the densities of charged states could look when the spiro-OMeTAD DOS using three Gaussian functions each with a width of 0.1 eV and with centers spaced 0.2 eV apart. The total DOS used was 1 x 10^{21} cm^{-3}, with a carrier concentration of 3 x 10^{20} cm^{-3} and 25% of charged molecules in the bipolaron state. These parameters were an approximation based on typical parameters for amorphous small molecules and the properties of F_4TCNQ:spiro-OMeTAD.–Differential pulse voltammetry measurements in solvent have shown that the first three oxidation potentials of spiro-OMeTAD are -5.15, -5.27, and -5.48 eV.[12] However, the exact spacing of neutral, 1+, and 2+ states may change in the solid state, especially if the dielectric constant of the film changes with doping. In addition to changing the shape of the DOS, bipolarons have

also been associated with an increase in Seebeck coefficient in hopping semiconductors through an increase in vibrational entropy.[34]

To complement these studies, we studied the changes in thermal transport in spiro-OMeTAD films with doping. We measured the in-plane thermal diffusivity of films with varying carrier concentrations with a transient grating technique.[35] The transient gradient apparatus uses a visible wavelength laser (515 nm or 2.4 eV) to induce a periodic thermal expansion in the sample. Spiro-OMeTAD^{+} and spiro-OMeTAD^{2+} absorb at this wavelength, so the doped films could be measured without any change in sample preparation. Because undoped spiro-OMeTAD films are transparent to the pump laser, we prepared a dyed spiro-OMeTAD film by blade-coating a film from a solution of Oil Red O and spiro-OMeTAD in chlorobenzene. The thermal diffusivity of this pink-dyed film of insulating spiro-OMeTAD was 0.155 ± 0.004 mm^2/s. The thermal diffusivity of F_4TCNQ vapor-doped films, shown in Figure 2.8, was roughly constant, or slightly decreasing, with carrier concentration in the range measured.

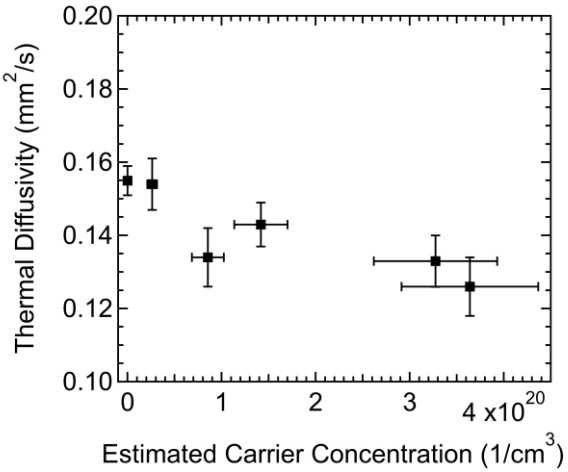

Figure 2.8. In-plane thermal diffusivity of the samples is roughly constant over this carrier concentration range. The y error is the thermal diffusivity fitting error, and the estimated carrier concentration error is 20%.

The thermal conductivity can be calculated from the product of the thermal diffusivity, density, and specific heat capacity. We measured the specific heat capacity of spiro-OMeTAD powder with modulated differential scanning calorimetry (0.9 J/kg·°C) and took the density of spiro-OMeTAD films as 1.02 g/cm^3.[27] With these values, we find an in-plane thermal conductivity for spiro-OMeTAD of 0.14 W/m·K. This thermal conductivity is similar to measurements on other amorphous molecules of 0.14-0.15 W/m·K.[36] For comparison, undoped C_{60} and its derivatives have even lower thermal conductivity of ≈0.06 W/m·K,[37] while undoped films of semiconducting polymers can have thermal conductivities of ≈0.2 to 2 W/m·K depending on the crystallinity and molecular orientation.[38–41] The thermal conductivity of doped samples will depend on changes in density or heat capacity, but we can expect that the former is unlikely to increase more than ≈20% (based on the density of crystalline spiro-OMeTAD) and the latter by a comparable factor. Any expected change due to these factors would be relatively small and would tend to bring the thermal conductivity of the doped samples to the same level as the undoped samples. This result is not surprising given the low electrical conductivity of the doped samples but does show that the intermolecular interactions of the charged molecules likely do not substantially modify the thermal conductivity of the amorphous films. The resulting thermoelectric figure of merit is quite low, $ZT=0.8\times10^{-4}$ at room temperature.

2.4. Conclusions

We used vapor infiltration to dope spiro-OMeTAD films with F_4TCNQ up to 39 ± 2 mol% F_4TCNQ. Although spiro-OMeTAD can crystallize in neutral form, the doped films remained amorphous. Our results show that this doping method can be used to reach a high conductivity relative to other doped *p*-type small molecules and provides a convenient route

to study doping in small molecules. An increase in the Seebeck coefficient at ≈2.8 x 10^{20} 1/cm^3 suggested that the presence of spiro-$OMeTAD^{2+}$ in the films changes the shape of the DOS. Finally, we found that the thermal diffusivity of spiro-OMeTAD is similar to other amorphous organic materials and does not change significantly with doping. Our findings also suggest that degenerate frontier orbitals may change the thermoelectric properties of organic semiconductors and could be a useful molecular design parameter.

2.5. Acknowledgements

This work was supported by the National Science Foundation (NSF) under DMR 1808622. Portions of this work were carried out at the MRL Shared Experimental Facilities, supported by the NSF MRSEC program under award no. DMR 1720256. Use of the Stanford Synchrotron Radiation Lightsource, SLAC National Accelerator Laboratory, is supported by the U.S. Department of Energy, Office of Science, Office of Basic Energy Sciences under Contract No. DE-AC02-76SF00515. Use was made of computational facilities purchased with funds from the National Science Foundation (CNS-1725797) and administered by the Center for Scientific Computing (CSC). The CSC is supported by the California NanoSystems Institute (CNSI) and the MRSEC (NSF DMR 1720256) at UC Santa Barbara. We acknowledge the use of the Nanostructures Cleanroom Facility within the CNSI, supported by UC Santa Barbara and the UC Office of the President. A.P. was funded by the FLAM program under NSF award no. DMR 1460656. A. V. and B. L. acknowledges the support of a Sony Faculty Research Award for the thermal transport measurements. We thank Kathryn A. O'Hara and Naveen R. Venkatesan for assistance with GIWAXS measurements and Tom Mates for assistance with SIMS.

2.6. Appendix S1: Supplementary Information

2.6.1 Vapor Doping

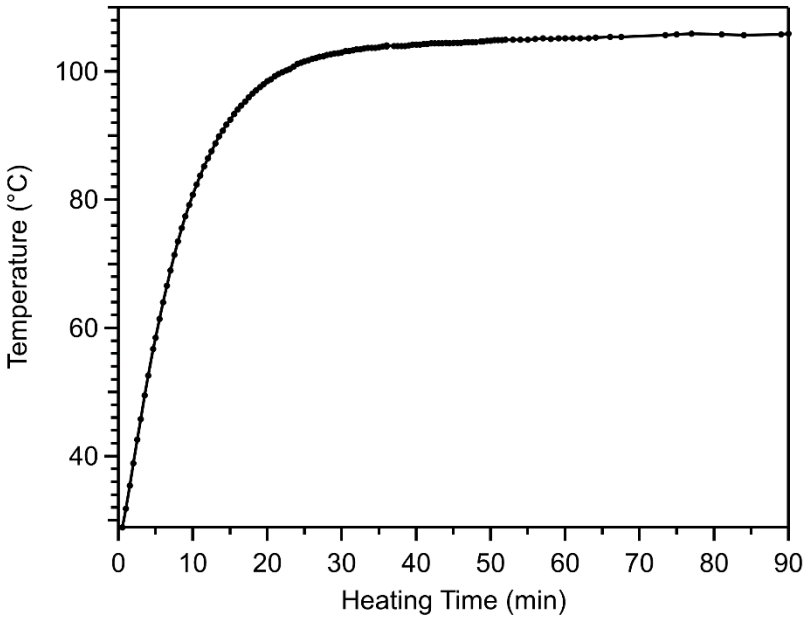

Figure S 1.1. Temperature of substrate in vapor doping chamber vs. time heated at 200 °C. Temperature is nearly level after 30 min, only increasing from 103-106 °C during the last 60 min of heating.

2.6.2 GIWAXS Linecuts

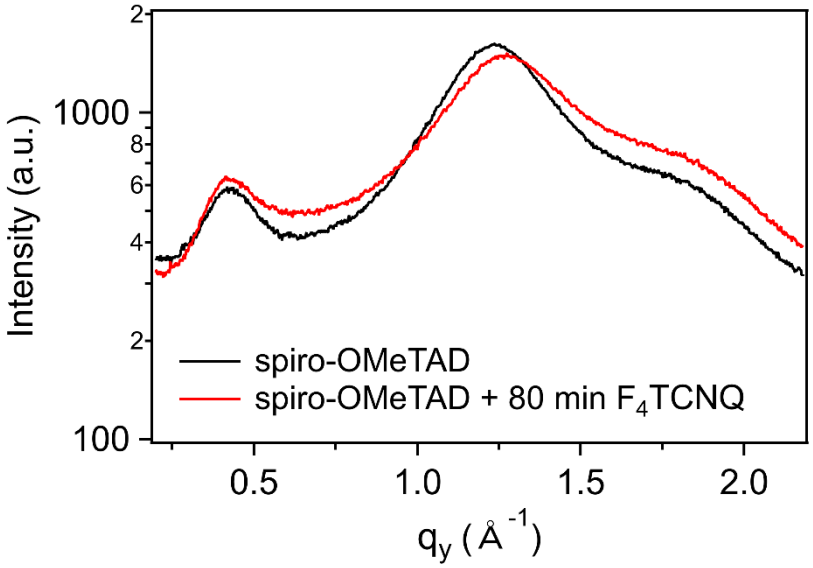

Figure S 1.2. Q_y linecuts of undoped (black) and 80 min F_4TCNQ vapor doped (red) spiro-OMeTAD from GIWAXS scattering.

2.6.3 F_4TCNQ Anion Reference

We synthesized $[Cp^*_2Co][F_4TCNQ]$ and $[Cp^*_2Fe][F_4TCNQ]$ similar to previously reported procedure.[24] We measured varying concentrations of $[Cp^*_2Co][F_4TCNQ]$ or $[Cp^*_2Fe][F_4TCNQ]$ in acetonitrile in 1 cm quartz cuvettes (Figure S1.3). Calculating the maximum NIR molar attenuation coefficient, ε, from each spectrum resulted in inconsistent ε values (Table S1). Fitting the absorbance at the tallest NIR peak for F_4TCNQ^- (857 nm) vs. concentration with a line gives an ε ~35,500 M^{-1} cm^{-1} (Figure S1.4). This value is lower than the previously measured ε value for $[Cp^*_2Co][F_4TCNQ]$ of ~50,000 M^{-1} cm^{-1},[24] but it is closer to ε values ~40,000-42,000 M^{-1} cm^{-1} reported for other F_4TCNQ anionic compounds (Table S1.2).[42,43] Our ε value may differ from these previous measurements due to small errors in the ionic compound synthesis or in preparing the reference solutions. We used the average of the fitted NIR F_4TCNQ^- molar attenuation peak areas (8331 eV M^{-1} cm^{-1}) as the reference value for estimating film carrier concentrations. The standard deviation of this average is 12.5%, but to account for any additional sources of error, we estimated the error in the carrier concentrations at 20%.

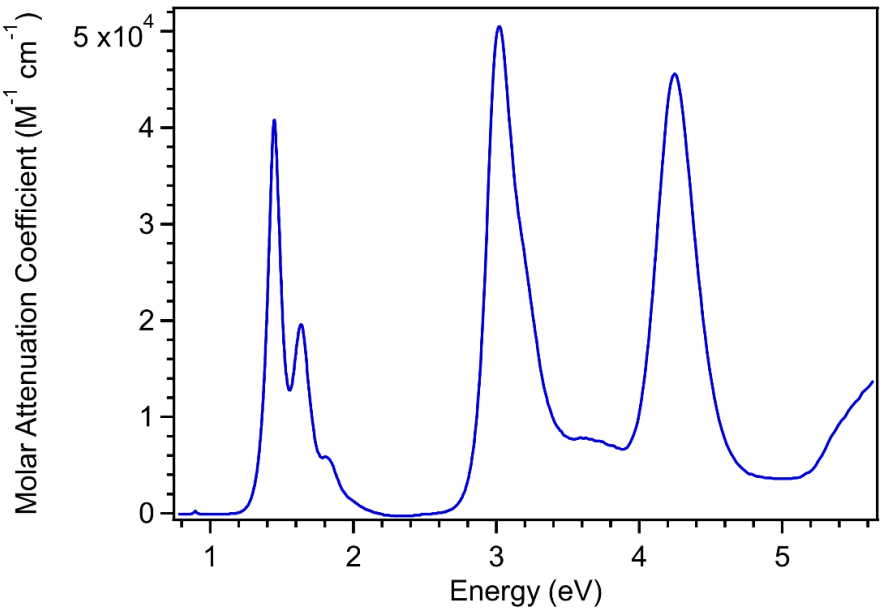

Figure S 1.3. UV-Vis-NIR molar attenuation coefficient spectrum of $[Cp^*_2Co][F_4TCNQ]$ 0.0074 mg/mL (12 mM) in acetonitrile in 1 cm quartz cuvette.

Table S 1.1. F_4TCNQ anion molar attenuation coefficient results from several solution UV-Vis-NIR trials.

Compound	Concentration (mM)	ε at 857 nm (M^{-1} cm^{-1})	Fitted ε NIR area sum (eV M^{-1} cm^{-1})
$[Cp^*_2Co][F_4TCNQ]$	4.1	35,300	7768
$[Cp^*_2Co][F_4TCNQ]$	8.2	44,200	10,051
$[Cp^*_2Co][F_4TCNQ]$	8.3	33,300	7325
$[Cp^*_2Co][F_4TCNQ]$	12	40,900	9016
$[Cp^*_2Fe][F_4TCNQ]$	17	34,900	7497
	Average:	37,700 ± 4100	8331 ± 1044

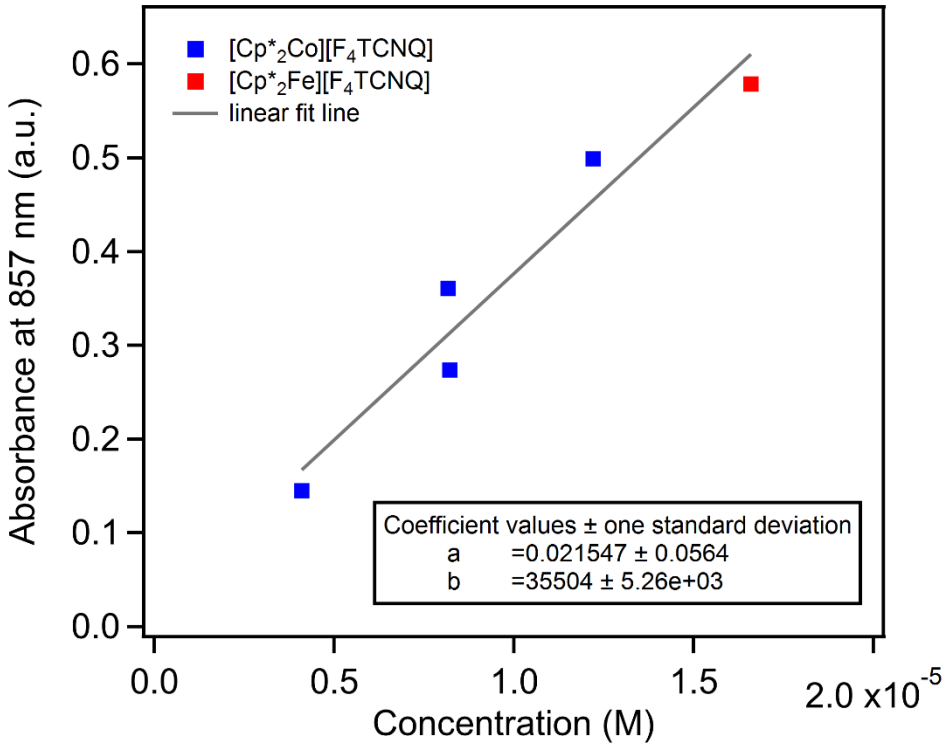

Figure S 1.4. Plot of NIR absorbance at 857 nm of varying concentrations of $[Cp^*_2Co][F_4TCNQ]$ (blue) or $[Cp^*_2Fe][F_4TCNQ]$ (red) solution in acetonitrile solution. Slope of linear fit line (b) used to calculate the molar attenuation coefficient, ε, of F_4TCNQ^- at 857 nm.

Table S 1.2. Previously reported NIR molar attenuation coefficient (ε) values for F_4TCNQ anions.

Compound	Peak ε in NIR (M^{-1} cm^{-1})	Ref.
$[Cp^*_2Co][F_4TCNQ]$	~50,000	24
F_4TCNQ and excess tetrabutylammonium iodide	~40,000	51
$Li^+F_4TCNQ^{\bullet-}$	~42,000	52

2.6.4 F_4TCNQ Anion Fitting Method

The area of the three NIR F_4TCNQ anion peaks was used to estimate the carrier concentration of the doped spiro-OMeTAD films for electrical, thermoelectric, and thermal transport measurements. The area of the three peaks was calculated by fitting them using the Multi-peak Fitting package in Igor. The fitting was performed on the section of the spectrum 1.25 – 2.15 eV using a set linear baseline to reduce background effects. For solution spectra, three Voigt peaks (convolution of Gaussian and Lorentzian peaks) were used, with the constraint that they must have the same width and shape factor within the spectrum (Figure S1.5). The height of peak 1 was constrained as half of the height of peak 0, and the height of peak 2 was constrained as one-fourth the height of peak 1. For the chosen reference spectrum (Figure S1.5), the shape factor was 0.56, indicating both Gaussian and Lorentzian contributions to the peak shape.

For film spectra, the same fitting method was used with the addition of a fourth peak for the smaller spiro-$OMeTAD^+$ absorbance at 700 nm (1.77 eV) that is obscured by the F_4TCNQ^- absorbances. Because this peak has an asymmetric shape, especially at low spiro-$OMeTAD^+$ concentrations,[25] we used the "ExpModGauss" peak shape (convolution of Gaussian peak and exponential decay) to fit this obscured absorbance peak (Figure S1.6). The location of this peak was constrained between 1.5-1.8 eV and was usually fit to a location 1.7-1.8 eV. For the F_4TCNQ^- peak fittings, the Voigt shape parameter was close to zero, indicating a Gaussian peak shape. See Figure S1.7 for how the calculated carrier concentration estimates correspond to vapor doping time.

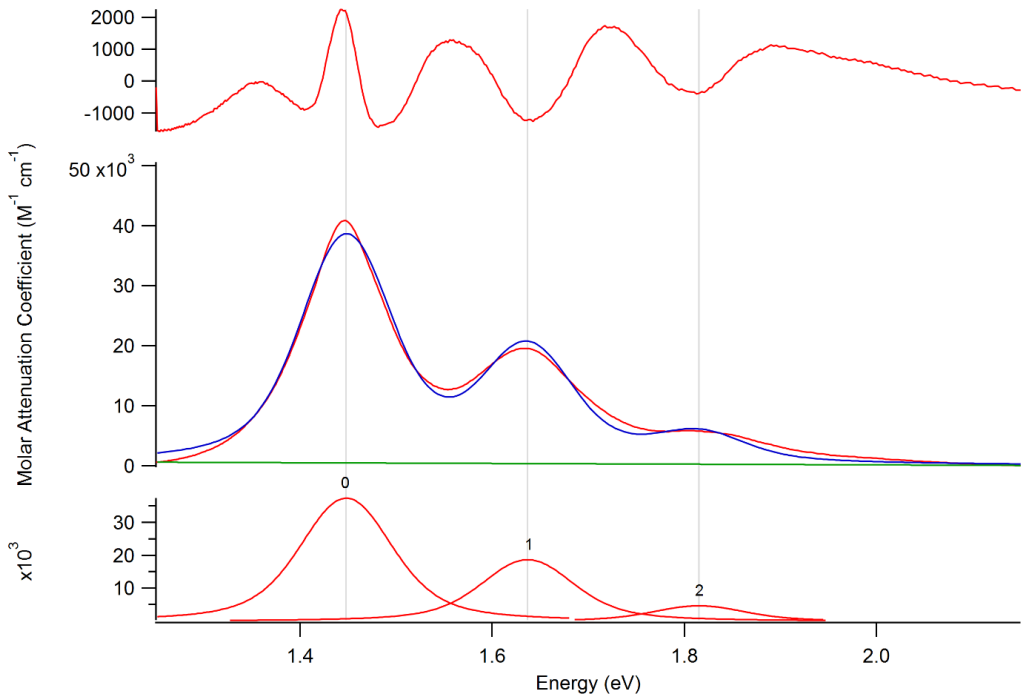

Figure S 1.5. Fitting results for 12 mM [Cp^*_2Co][F_4TCNQ] reference solution. Top panel shows deviation of fit from spectrum. Middle panel shows sum of fit peaks (blue) and the baseline (green) over the reference spectrum (red). Bottom panel shows the three Voigt peaks used to fit the spectrum.

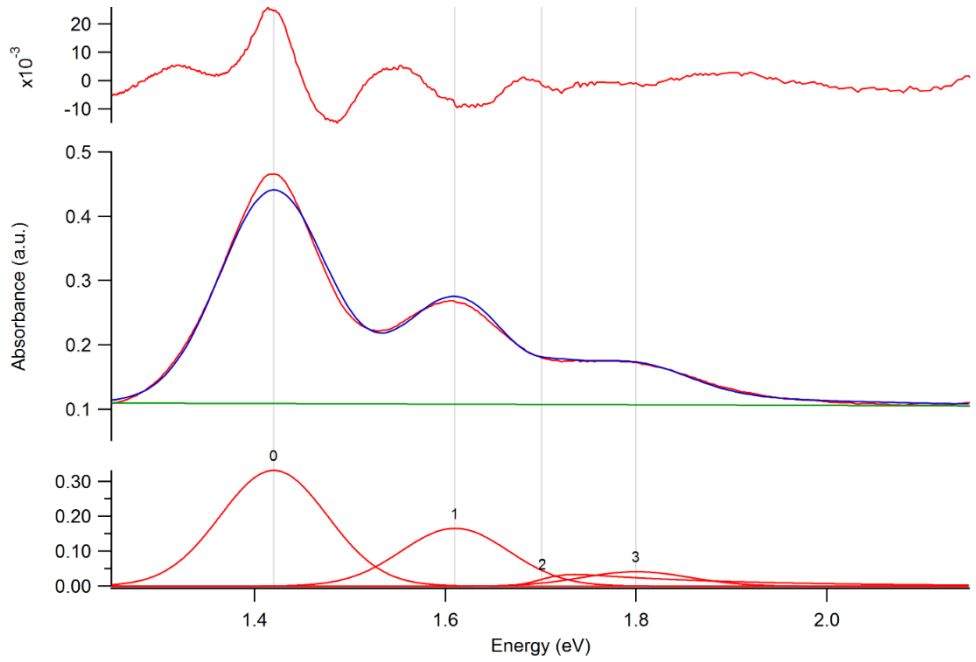

Figure S 1.6. Example of fitting results for a F_4TCNQ vapor-doped spiro-OMeTAD film. Top panel shows deviation of fit from the film spectrum. Middle panel shows the sum of the fit peaks (blue) and baseline (green) over the film spectrum (red). Bottom panel shows the four peaks used to fit the spectrum. Peaks 0, 1, and 3 are the Voigt (nearly Gaussian) peaks fitting the F_4TCNQ anion signal. Peak 2 is the ExpModGauss peak at 1.74 eV fitting the spiro-$OMeTAD^+$ signal.

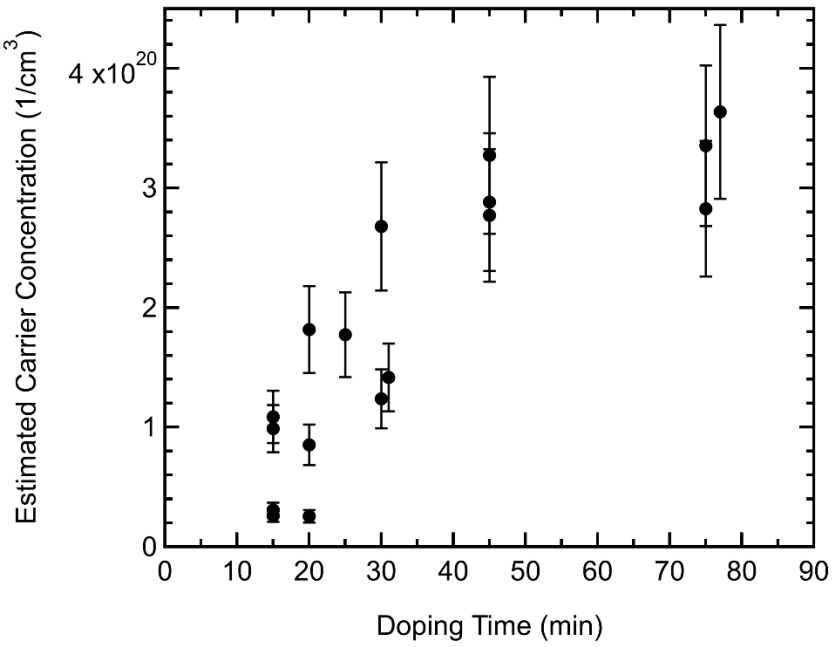

Figure S 1.7. Estimated carrier concentration versus doping time.

2.6.5 Density Estimation

Film thickness and carrier concentrations are the averages of three samples with the same doping time. Mass densities for doped films were estimated by adding the mass of F_4TCNQ molecules (from the estimated carrier concentration) to the average mass of an average undoped spiro-OMeTAD film (417 nm thick). The estimated F_4TCNQ mol% was calculated using the amount of F_4TCNQ estimated from the UV-Vis-NIR spectra and the amount of spiro-OMeTAD in a film with a density of 1.02 g/cm^3.[27]

$$\frac{1.02\ g}{cm^3} \times \frac{mol}{1225.43\ g} \times N_A = 5.02 \times 10^{20}\ molecules/cm^3$$

Table S 1.3. Average thickness and estimated mol% of spiro-OMeTAD:F_4TCNQ films depending on doping time.

Doping Time (min)	Thickness (nm)	Estimated Carrier Concentration (x 10^{20} 1/cm^3)	Estimated Mass Density (g/cm^3)	Estimated mol% F_4TCNQ
0	417 ± 15	0	1.02 (ref. 27)	0
15	495 ± 98	0.7 ± 0.4	0.92 ± 0.16	11 ± 6
20	461 ± 17	0.9 ± 0.6	0.97 ± 0.05	15 ± 9
30	479 ± 22	1.8 ± 0.6	0.97 ± 0.04	26 ± 7
45	544 ± 9	3.0 ± 0.2	0.918 ± 0.005	37 ± 2
75	506 ± 29	3.3 ± 0.3	0.99 ± 0.04	39 ± 2

2.6.6 Mobility

Mobility (μ) was calculated using conductivity (σ) measurements and estimated carrier concentrations (p). The hole mobility stays on the order of 10^{-4} $cm^2/V{\cdot}s$ but some points may indicate a downward trend in mobility with increasing carrier concentration.

$$\mu = \frac{\sigma}{pq}$$

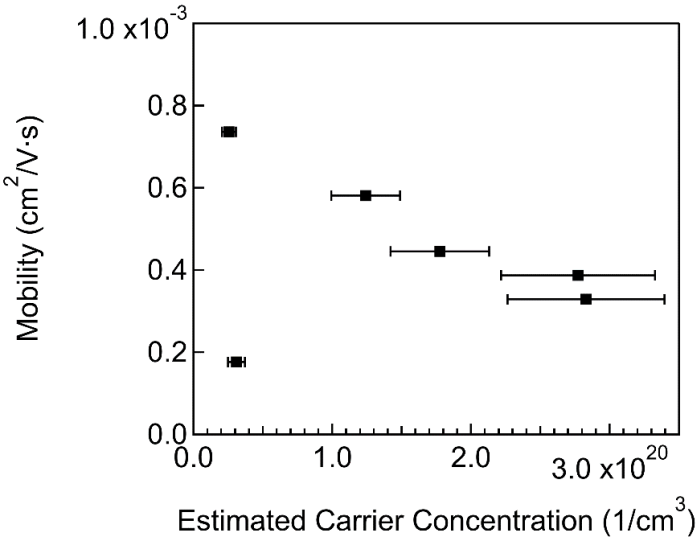

Figure S 1.8. Calculated hole mobility as a function of estimated carrier concentration.

2.6.7 Temperature-dependent Conductivity

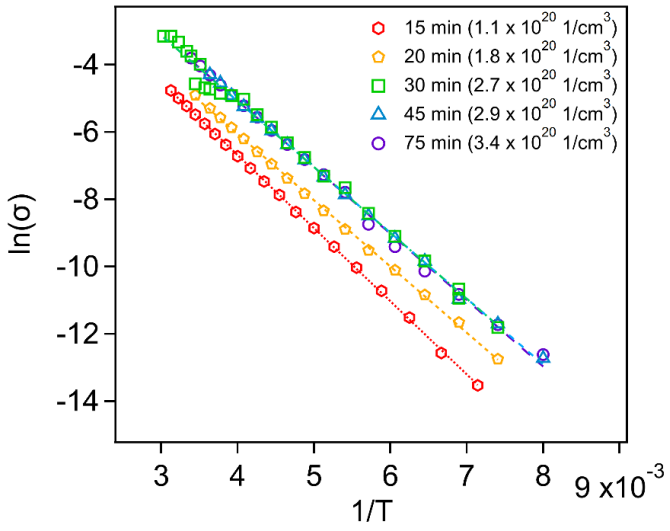

Figure S 1.9. Temperature-dependent conductivity plotted as the natural log of conductivity (S/cm) vs. inverse temperature (K) to show the Arrhenius relationship of thermally activated hopping.

2.7. References

1 S. R. Forrest, *Organic Electronics: Foundations to Applications*, Oxford University Press, Oxford, 2020.

2 L. Calió, S. Kazim, M. Grätzel and S. Ahmad, Hole-Transport Materials for Perovskite Solar Cells, *Angew. Chem. Int. Ed.*, 2016, **55**, 14522–14545.

3 J. Urieta-Mora, I. García-Benito, A. Molina-Ontoria and N. Martín, Hole transporting materials for perovskite solar cells: a chemical approach, *Chem. Soc. Rev.*, 2018, **47**, 8541–8571.

4 A. P. Proudian, M. B. Jaskot, D. R. Diercks, B. P. Gorman and J. D. Zimmerman, Atom Probe Tomography of Molecular Organic Materials: Sub-Dalton Nanometer-Scale Quantification, *Chem. Mater.*, 2019, **31**, 2241–2247.

5 K. Walzer, B. Maennig, M. Pfeiffer and K. Leo, Highly Efficient Organic Devices Based on Electrically Doped Transport Layers, *Chem. Rev.*, 2007, **107**, 1233–1271.

6 V. I. Arkhipov, P. Heremans, E. V. Emelianova and H. Bässler, Effect of doping on the density-of-states distribution and carrier hopping in disordered organic semiconductors, *Phys. Rev. B*, 2005, **71**, 045214.

7 M. Schwarze, C. Gaul, R. Scholz, F. Bussolotti, A. Hofacker, K. S. Schellhammer, B. Nell, B. D. Naab, Z. Bao, D. Spoltore, K. Vandewal, J. Widmer, S. Kera, N. Ueno, F. Ortmann and K. Leo, Molecular parameters responsible for thermally activated transport in doped organic semiconductors, *Nat. Mater.*, 2019, **18**, 242–248.

8 R. Schmechel, Hopping transport in doped organic semiconductors: A theoretical approach and its application to p-doped zinc-phthalocyanine, *J. Appl. Phys.*, 2003, **93**, 4653–4660.

9 T. Menke, D. Ray, H. Kleemann, M. P. Hein, K. Leo and M. Riede, Highly efficient p-dopants in amorphous hosts, *Org. Electron.*, 2014, **15**, 365–371.

10 A. Fediai, F. Symalla, P. Friederich and W. Wenzel, Disorder compensation controls doping efficiency in organic semiconductors, *Nat. Commun.*, 2019, **10**, 4547.

11 Z. Hawash, L. K. Ono and Y. Qi, Recent Advances in Spiro-MeOTAD Hole Transport Material and Its Applications in Organic–Inorganic Halide Perovskite Solar Cells, *Adv. Mater. Interfaces*, 2018, **5**, 1700623.

12 W. H. Nguyen, C. D. Bailie, E. L. Unger and M. D. McGehee, Enhancing the Hole-Conductivity of Spiro-OMeTAD without Oxygen or Lithium Salts by Using Spiro(TFSI)2 in Perovskite and Dye-Sensitized Solar Cells, *J. Am. Chem. Soc.*, 2014, **136**, 10996–11001.

13 T. Leijtens, J. Lim, J. Teuscher, T. Park and H. J. Snaith, Charge Density Dependent Mobility of Organic Hole-Transporters and Mesoporous TiO2 Determined by Transient Mobility Spectroscopy: Implications to Dye-Sensitized and Organic Solar Cells, *Adv. Mater.*, 2013, **25**, 3227–3233.

14 A. Abate, T. Leijtens, S. Pathak, J. Teuscher, R. Avolio, M. E. Errico, J. Kirkpatrik, J. M. Ball, P. Docampo, I. McPherson and H. J. Snaith, Lithium salts as “redox active” p-type dopants for organic semiconductors and their impact in solid-state dye -sensitized solar cells, *Phys. Chem. Chem. Phys.*, 2013, **15**, 2572–2579.

15 D. Shi, X. Qin, Y. Li, Y. He, C. Zhong, J. Pan, H. Dong, W. Xu, T. Li, W. Hu, J.-L. Brédas and O. M. Bakr, Spiro-OMeTAD single crystals: Remarkably enhanced charge-carrier transport via mesoscale ordering, *Sci. Adv.*, 2016, **2**, e1501491.

16 Y. Li, H. Li, C. Zhong, G. Sini and J.-L. Brédas, Characterization of intrinsic hole transport in single-crystal spiro-OMeTAD, *npj Flexible Electron.*, 2017, **1**, 2.
17 T. Körzdörfer and J.-L. Brédas, Organic Electronic Materials: Recent Advances in the DFT Description of the Ground and Excited States Using Tuned Range-Separated Hybrid Functionals, *Acc. Chem. Res.*, 2014, **47**, 3284–3291.
18 W. Gao and A. Kahn, Controlled p-doping of zinc phthalocyanine by coevaporation with tetrafluorotetracyanoquinodimethane: A direct and inverse photoemission study, *Appl. Phys. Lett.*, 2001, **79**, 4040–4042.
19 S. N. Patel, A. M. Glaudell, K. A. Peterson, E. M. Thomas, K. A. O'Hara, E. Lim and M. L. Chabinyc, Morphology controls the thermoelectric power factor of a doped semiconducting polymer, *Sci. Adv.*, 2017, **3**, e1700434.
20 E. Lim, K. A. Peterson, G. M. Su and M. L. Chabinyc, Thermoelectric Properties of Poly(3-hexylthiophene) (P3HT) Doped with 2,3,5,6-Tetrafluoro-7,7,8,8-tetracyanoquinodimethane (F4TCNQ) by Vapor-Phase Infiltration, *Chem. Mater.*, 2018, **30**, 998–1010.
21 T. Malinauskas, D. Tomkute-Luksiene, R. Sens, M. Daskeviciene, R. Send, H. Wonneberger, V. Jankauskas, I. Bruder and V. Getautis, Enhancing Thermal Stability and Lifetime of Solid-State Dye-Sensitized Solar Cells via Molecular Engineering of the Hole-Transporting Material Spiro-OMeTAD, *ACS Appl. Mater. Interfaces*, 2015, **7**, 11107–11116.
22 J. Li, C. W. Rochester, I. E. Jacobs, S. Friedrich, P. Stroeve, M. Riede and A. J. Moulé, Measurement of Small Molecular Dopant F4TCNQ and C60F36 Diffusion in Organic Bilayer Architectures, *ACS Appl. Mater. Interfaces*, 2015, **7**, 28420–28428.
23 J. E. Cochran, M. J. N. Junk, A. M. Glaudell, P. L. Miller, J. S. Cowart, M. F. Toney, C. J. Hawker, B. F. Chmelka and M. L. Chabinyc, Molecular Interactions and Ordering in Electrically Doped Polymers: Blends of PBTTT and F4TCNQ, *Macromolecules*, 2014, **47**, 6836–6846.
24 D. A. Dixon, J. C. Calabrese and J. S. Miller, Crystal and molecular structure of the 2:1 charge-transfer salt of decamethylferrocene and perfluoro-7,7,8,8-tetracyano-p-quinodimethane: [[Fe(C5Me5)2]+.cntdot.]2[TCNQF4]2-. The electronic structure of [TCNQF4]n (n = 0, 1-, 2-), *J. Phys. Chem.*, 1989, **93**, 2284–2291.
25 U. Bach, PhD Thesis, École Polytechnique Fédérale de Lausanne, 2000.
26 S. Fantacci, F. De Angelis, M. K. Nazeeruddin and M. Grätzel, Electronic and Optical Properties of the Spiro-MeOTAD Hole Conductor in Its Neutral and Oxidized Forms: A DFT/TDDFT Investigation, *J. Phys. Chem. C*, 2011, **115**, 23126–23133.
27 P. Docampo, A. Hey, S. Guldin, R. Gunning, U. Steiner and H. J. Snaith, Pore Filling of Spiro-OMeTAD in Solid-State Dye-Sensitized Solar Cells Determined Via Optical Reflectometry, *Adv. Funct. Mater.*, 2012, **22**, 5010–5019.
28 Q. Liu, L. Fan, Q. Zhang, A. Zhou, B. Wang, H. Bai, Q. Tian, B. Fan and T. Zhang, Benzoyl Peroxide as an Efficient Dopant for Spiro-OMeTAD in Perovskite Solar Cells, *ChemSusChem*, 2017, **10**, 3098–3104.
29 J. A. Röhr, X. Shi, S. A. Haque, T. Kirchartz and J. Nelson, Charge Transport in Spiro-OMeTAD Investigated through Space-Charge-Limited Current Measurements, *Phys. Rev. Appl.*, 2018, **9**, 044017.
30 F. Zhang and A. Kahn, Investigation of the High Electron Affinity Molecular Dopant F6-TCNNQ for Hole-Transport Materials, *Adv. Funct. Mater.*, 2017, **28**, 1703780.

31 N. F. Mott and E. A. Davis, *Electronic processes in non-crystalline materials*, Oxford University Press, Oxford, 2nd ed., 1979.
32 G. Zuo, X. Liu, M. Fahlman and M. Kemerink, High Seebeck Coefficient in Mixtures of Conjugated Polymers, *Adv. Funct. Mater.*, 2017, **28**, 1703280.
33 A. Abtahi, S. Johnson, S. M. Park, X. Luo, Z. Liang, J. Mei and K. R. Graham, Designing π-conjugated polymer blends with improved thermoelectric power factors, *J. Mater. Chem. A*, 2019, **7**, 19774–19785.
34 D. Emin, Enhanced Seebeck coefficient from carrier-induced vibrational softening, *Phys. Rev. B*, 1999, **59**, 6205–6210.
35 A. Vega-Flick, D. Jung, S. Yue, J. E. Bowers and B. Liao, Reduced thermal conductivity of epitaxial GaAs on Si due to symmetry-breaking biaxial strain, *Phys. Rev. Mater.*, 2019, **3**, 034603.
36 X. Xie, K. Yang, D. Li, T.-H. Tsai, J. Shin, P. V. Braun and D. G. Cahill, High and low thermal conductivity of amorphous macromolecules, *Phys. Rev. B*, 2017, **95**, 035406.
37 X. Wang, C. D. Liman, N. D. Treat, M. L. Chabinyc and D. G. Cahill, Ultralow thermal conductivity of fullerene derivatives, *Phys. Rev. B*, 2013, **88**, 075310.
38 J. C. Duda, P. E. Hopkins, Y. Shen and M. C. Gupta, Thermal transport in organic semiconducting polymers, *Appl. Phys. Lett.*, 2013, **102**, 251912.
39 H. Ushirokita and H. Tada, In-plane Thermal Conductivity Measurement of Conjugated Polymer Films by Membrane-based AC Calorimetry, *Chem. Lett.*, 2016, **45**, 735–737.
40 J. Liu, X. Wang, D. Li, N. E. Coates, R. A. Segalman and D. G. Cahill, Thermal Conductivity and Elastic Constants of PEDOT:PSS with High Electrical Conductivity, *Macromolecules*, 2015, **48**, 585–591.
41 A. Roy, T. L. Bougher, R. Geng, Y. Ke, J. Locklin and B. A. Cola, Thermal Conductance of Poly(3-methylthiophene) Brushes, *ACS Appl. Mater. Interfaces*, 2016, **8**, 25578–25585.
42 D. T. Scholes, S. A. Hawks, P. Y. Yee, H. Wu, J. R. Lindemuth, S. H. Tolbert and B. J. Schwartz, Overcoming Film Quality Issues for Conjugated Polymers Doped with F4TCNQ by Solution Sequential Processing: Hall Effect, Structural, and Optical Measurements, *J. Phys. Chem. Lett.*, 2015, **6**, 4786–4793.
43 D. Kiefer, R. Kroon, A. I. Hofmann, H. Sun, X. Liu, A. Giovannitti, D. Stegerer, A. Cano, J. Hynynen, L. Yu, Y. Zhang, D. Nai, T. F. Harrelson, M. Sommer, A. J. Moulé, M. Kemerink, S. R. Marder, I. McCulloch, M. Fahlman, S. Fabiano and C. Müller, Double doping of conjugated polymers with monomer molecular dopants, *Nat. Mater.*, 2019, **18**, 149–155.

3. Doping Semiconducting Polymers with a Lewis Acid-Base Pair

3.1. Introduction

Doping organic semiconductors is crucial to improving their electrical conductivity for applications in electronic and thermoelectric devices.[1,2] Organic semiconductors are typically doped with small molecules, but the number of highly effective, stable *p*-type dopants is relatively limited. Many *p*-type dopants have significant disadvantages, such as air or thermal instability, poor solubility in nonpolar solvents, and low efficiencies.[1] Another crucial aspect of doping semiconducting polymers is the interaction between doped polymers and molecular dopant counterions that frequently causes aggregation in solution and difficulty in processing homogeneous films.[3,4] Developing new dopants along with mechanistic understanding of their efficiency will help to address these critical issues.

One promising *p*-type dopant is the Lewis acid tris(pentafluorophenyl)borane (BCF, $B(C_6F_5)_3$). BCF has been found to dope organic semiconductors with a varying range of structures in solution, including poly(3-hexylthiophene) (P3HT),[5–8] poly[2,6-(4,4-bis(2-hexadecyl)-4*H*cyclopenta[2,1-*b*;3,4-*b*′]dithiophene)-*alt*-4,7(2,1,3-benzothiadiazole)] (PCPDTBT),[9] and 2,2′,7,7′-tetrakis[*N*,*N*-di(4-methoxyphenol)amino]-9,9′-spirobifluorene (spiro-OMeTAD).[10] These organic semiconductors have ionization energies near 5 eV. Electron spin resonance (ESR) spectroscopy confirmed that the reaction with BCF leads to formation of carriers with unpaired spin on the semiconductor.[5,6,9,10] The efficiency of formation of charge carriers with BCF is lower than the widely studied dopant 2,3,5,6-tetrafluoro-7,7',8,8'-tetracyanoquinodimethane (F_4TCNQ) at equivalent molar ratios in

solution.[8,9] However, in some cases the apparent charge carrier mobility in the doped material can be higher.[9]

The mechanism of doping by BCF has been under wide investigation. Because BCF's electron affinity has been estimated at 3-3.5 eV,[11,12] simple integer charge transfer is an unlikely mechanism for generating charge carriers in organic semiconductors, given that their IE is typically > 4.5 eV. The BCF radical anion decomposes within minutes[13] and reacts with solvents,[11] complicating efforts to detect it and making it difficult to determine what role, if any, it might play in doping. Because BCF easily complexes with water to form a Brønsted acid,[14] an acid doping mechanism has been proposed to explain the observation of *p*-type doping.[9] In acid doping, the acid protonates a polymer chain, and the protonated polymer chain accepts an electron from a second (or other section of the initial) polymer chain. Supporting this mechanism, the addition of water was shown to increase BCF's doping efficiency with PCPDTBT.[9] Additional reaction steps in this mechanism have been proposed, including elimination of H_2 from hydrogenated polymer chains and formation of larger counterion complexes like $[BCF(OH)(OH_2)BCF]^-$. These steps helped to rationalize the unfavorable *ab initio* calculated energetics of the protonation reaction alone.[15]

In addition to acid doping by the complex $BCF{\cdot}H_2O$, BCF can participate in several other reactions that interfere with interpretation of its properties as a dopant. As a Lewis acid, BCF could form dative bonds with heteroatoms in organic semiconductors. However, only a small group of polymers may be Lewis basic enough for complex formation, such as those with highly Lewis basic nitrogen atoms in their backbone.[16–19] One further complication of BCF's reactivity is that BCF and O_2 can act as a one-electron oxidant in the presence of a donor, forming the counterion $[(C_6F_5)_3B\text{-}O_2\text{-}B(C_6F_5)_3]^-$.[20] As these reactions suggest, the

presence of differing amounts of water and oxygen along with varying solvents can make determination of a precise mechanism challenging.

Recent studies in one-electron oxidation reactions by Lewis acid-base pairs suggest a more energetically favorable way of utilizing BCF for one-electron oxidation. A Lewis acid and base pair may be sterically prevented from forming an adduct (a frustrated Lewis pair) or have a dissociative equilibrium.[21] These pairs can undergo reactions unlike conventional Lewis acid-base adducts. For example, when BCF is combined with a weak Lewis base, the formation of the Lewis pair (LP) can drive the single electron oxidation of decamethylferrocene.[22] In the proposed two-step mechanism for this reaction, BCF first oxidizes decamethylferrocene to form BCF radical anions. Then, BCF radical anions react with benzoyl peroxide (BPO), or another Lewis base, to form the counterion [PhC(O)O-$B(C_6F_5)_3]^-$, yielding **C1** (Scheme 3.1).[22] Similar oxidation reactions have been demonstrated using oxygen[20] or quinones[23] as the weak Lewis base. The ability of Lewis acid-base pairs to carry out single electron transfer reactions suggests a route to increase the efficiency of BCF as a dopant for organic semiconductors.

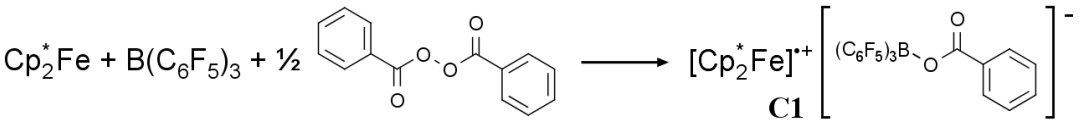

Scheme 3.1. Oxidation of decamethylferrocene by $B(C_6F_5)_3$ and benzoyl peroxide (BPO) reported by ref. [22].

Here we show that rational design of doping reactions using LPs is a route to efficiently doping a wide range of semiconducting polymers. The Lewis base BPO increased the doping efficiency of BCF with several semiconducting polymers with different backbone structures. Using regiorandom P3HT, we were able to confirm the expected product of the LP doping

reaction. In the solid state, the LP mechanism led to high electrical conductivities and changes in P3HT film morphology.

3.2. Experimental Methods

3.2.1 Materials

Except where noted, dry $B(C_6F_5)_3$ (98%, TCI America, used as received, stored at room temperature in N_2 glovebox) was used for all experiments. Benzoyl peroxide (Luperox A98) was used as received within 6-8 months of opening the bottle.

Purchased polymers were used as received: P3HT (Merck Lisicon SP001), RRa-P3HT (Sigma Aldrich), MEH-PPV (LumTec), and PFO (ADS). C_2C_6-IDTBT was synthesized by the McCulloch Lab as previously described.[§] Anhydrous solvents were used as received: chloroform (anhydrous, Sigma Aldrich); chlorobenzene (anhydrous, Sigma Aldrich); acetonitrile (99.9% Extra Dry, Acros Organics).

Anhydrous CD_2Cl_2 was prepared by drying CD_2Cl_2 (0.03% v/v TMS, Sigma Aldrich) with 4 Å molecular sieves (8-12 mesh, Fisher) for at least 3 days in an N_2 glovebox. Molecular sieves were dried for 24 h under vacuum in a vacuum oven at 150-200 °C. After a vacuum oven equipped with a rotary vane pump with hydrocarbon oil was suspected to be the source of the hydrocarbon grease signal in ^{1}H-NMR spectra, molecular sieve drying was moved to a vacuum oven equipped with a diaphragm pump. Anhydrous $CDCl_3$ was prepared by degassing $CDCl_3$ (Cambridge Isotope Laboratories) then drying with 4 Å molecular sieves as described above.

[§] H. Bronstein, D. S. Leem, R. Hamilton, P. Woebkenberg, S. King, W. Zhang, R. S. Ashraf, M. Heeney, T. D. Anthopoulos, J. de Mello and I. McCulloch, Indacenodithiophene-co-benzothiadiazole Copolymers for High Performance Solar Cells or Transistors via Alkyl Chain Optimization, *Macromolecules*, 2011, **44**, 6649–6652.

3.2.2 Spectroscopic Characterization

P3HT solutions for UV-Vis were prepared by first dissolving P3HT at 1 mg/mL, BCF at 6.2 mg/mL, and BPO at 1.5 mg/mL in chloroform. We added chloroform, BCF solution, BPO solution (in that order) to the P3HT solutions in the desired ratios so that the doped solution is at a P3HT concentration of 0.5 mg/mL. Doped solutions were stirred at room temperature at 300 rpm for 1-3 hours. Then, 50 μL of doped solution was diluted with 2 mL of chloroform in a capped 1 cm quartz cuvette for measurement. UV-Vis spectra were taken on a Shimadzu UV-3600 or UV-2600 spectrometer. Solutions of RRa-P3HT were prepared in a similar manner with DCM as the solvent. RRa-P3HT was dissolved at 0.5 mg/mL in DCM, doped at 0.33 mg/mL of RRa-P3HT, and diluted to 0.012 mg/mL of RRa-P3HT for UV-Vis measurement.

Solutions of the other polymers were prepared in a similar manner, except using air-exposed BCF (95%, Sigma Aldrich, see NMR below) and using chlorobenzene as the solvent. MEH-PPV was initially dissolved at 5 mg/mL in chlorobenzene, doped at 2.34 mg/mL of MEH-PPV, and diluted to 0.017 mg/mL of MEH-PPV for UV-Vis measurement. IDTBT was dissolved at 5 mg/mL in chlorobenzene, doped at 3 mg/mL of IDTBT, and diluted to 0.02 mg/mL of IDTBT for UV-Vis measurement. PFO was dissolved at 5 mg/mL in chlorobenzene, doped at 2.5 mg/mL of PFO, and diluted to 0.017 mg/mL of PFO for UV-Vis measurement.

Film UV-Vis-NIR spectra were recorded on a Shimadzu UV-3600 with an integrating sphere. Film FTIR spectra were recorded on a Nicolet Magna IR-850 Spectrometer.

3.2.3 NMR Spectroscopy

All spectra were recorded on a Varian VNMRS 600 MHz spectrometer at room temperature. Reaction mixture NMR solutions were prepared in a N_2 glovebox and transferred to glass screw-cap 500 Hz NMR tubes for measurement.

The initial solutions for most NMR reaction mixtures were RRa-P3HT (5 mg/mL), BCF (32.2 mg/mL), and BPO (7 mg/mL) in CD_2Cl_2. RRa-P3HT mixtures were diluted to 2.5 mg/mL. The BCF + 0.5 eq. BPO mixture was diluted to 8 mg/mL BCF and 1.75 mg/mL BPO. Reaction mixtures were stirred at room temperature at 300 rpm for 21 h before transfer to NMR tubes.

The RRa-P3HT + 0.3 eq. BCF mixture prep started with RRa-P3HT dissolved in CD_2Cl_2 at 0.5 mg/mL. Diluting CD_2Cl_2 and BCF solution in CD_2Cl_2 were added so that the reaction solution RRa-P3HT concentration was 0.33 mg/mL. The reaction mixture was stirred at room temperature at 300 rpm for 1 h before transfer to NMR tube.

^{1}H-NMR spectra in CD_2Cl_2 were calibrated to TMS, and those in $CDCl_3$ were calibrated to $CHCl_3$. ^{19}F-NMR spectra were calibrated to $CFCl_3$ by VnmrJ software.

3.2.4 Thin Film Preparation

P3HT solutions were prepared by dissolving P3HT in chloroform at 5.56 mg/mL (i.e. 5 mg per 0.9 mL) at room temperature for about 1 h. Then, acetonitrile was added to the P3HT solution in a 1:9 v/v ratio with chloroform (i.e. 5 mg P3HT per mL of 9:1 chloroform:acetonitrile).[1] P3HT vial was shaken once to mix the acetonitrile and chloroform (otherwise the acetonitrile may float on the surface of the chloroform). This mixture was allowed to equilibrate overnight (16-24 h) stirring 300 rpm at room temperature, resulting in a thick, dark purple mixture. Doped solutions at 2.5 mg/mL P3HT in 9:1 CF:ACN were

prepared by sequentially adding diluting chloroform, BCF in chloroform, BPO in chloroform, and diluting acetonitrile. Doped solutions stirred 300 rpm for 1-3 h at room temperature. Doped solutions were spun cast in a N_2 glovebox at 1000 rpm for 45 s (acceleration of 1000 rpm/s), then 3000 rpm for 30 s. No thermal annealing was performed after casting the films.

Films for conductivity measurements were cast on 15 mm x 15 mm x 1 mm quartz substrates. Films for GIWAXS were cast on native oxide silicon wafer pieces cut to approx. 15 mm x 15 mm. Quartz and silicon substrates were cleaned before film deposition by sequentially sonicating in soapy water (Alconox), DI water, acetone, and 2-propanol for 15 min each. Films for UV-Vis-NIR and FTIR spectroscopy were cast on new KBr plates.

3.2.5 GIWAXS

BCF used was purchased from Alfa Aesar (97%) and sublimated in a N_2 glovebox before use (see ^{19}F-NMR below). Films were otherwise prepared as described above on native oxide silicon substrates. GIWAXS was recorded at beamline 11-3 at the Stanford Synchrotron Radiation Lightsource (SSRL). Scattering was recorded at a 0.1° grazing angle with a sample-detector distance of 225 mm for 540 s under He flow. Scattering patterns were calibrated and analyzed using Igor packages NIKA[*] and WAXStools.[†] (citations in section 2.2 footnotes)

3.2.6 Charge Transport Measurements

Gold contacts (80 nm) were evaporated on top of the polymer films using an Angstrom Engineering thermal evaporator. The evaporation mask contact pattern contains several sets of four lines (1 mm x 0.1 mm with 0.2 mm spacing). Room-temperature conductivity was measured under N_2 atmosphere using the four-point probe method with a Keithley 6220 precision current source and Keithley 2400. Film thicknesses were measured by scratching

films with a razor blade and measuring the height difference with an Asylum MFP-3D Bio atomic force microscope in AC mode with FORTA AFM tips.

3.3. Results and Discussion

We explored the addition of BPO as a co-dopant for the reaction of BCF with P3HT as a model system (Scheme 3.2). BPO has been reported to form adducts with BCF in the absence of a donor, but reacts cleanly in the presence of [Cp_2^*Fe] to form a stable anion observed by NMR and by a single crystal structure.[22] While the mechanistic pathway is likely complex, we can split the proposed oxidation of a generic donor into four steps (Table 3.1). Among these reaction steps, the ionization energy of the donor (IE_D), electron affinity of BCF, and the homolytic bond dissociation energy of BPO are known or reasonably estimated. With the measured energies, we find the energy of formation of the known anion [PhC(O)O-$B(C_6F_5)_3$]$^-$ (E_4) can be related to the donor's ionization energy (IE_D) by Equation 3.2. Given the reported facile reaction of [Cp^*_2Fe] with IE_D = 5.1 eV, E_4 must be -2.56 eV or lower.

$$E_1 + E_2 + E_3 + E_4 < 0 \tag{3.1}$$

$$2.54 \text{ eV} - IE_D > E_4 \tag{3.2}$$

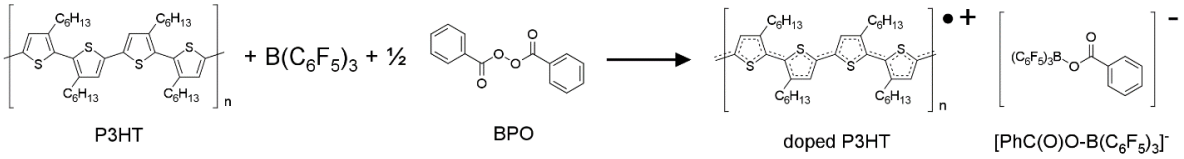

Scheme 3.2. Proposed doping mechanism of P3HT with $B(C_6F_5)_3$ and BPO explored in this paper.

Table 3.1. Four thermochemical steps of the proposed Lewis acid-base doping mechanism with energies assigned to variables or known from experiment.

	Reaction Step	Energy (eV)
E_1	$D \rightarrow D^{\bullet+} + e^-$	IE_D
E_2	$½ (PhC(O)O)_2 \rightarrow PhC(O)O\bullet$	+0.76[a]
E_3	$B(C_6F_5)_3 + e^- \rightarrow B(C_6F_5)_3^{\bullet-}$	-3.3[b]
E_4	$B(C_6F_5)_3^{\bullet-} + PhC(O)O\bullet \rightarrow [PhC(O)O\text{-}B(C_6F_5)_3]^-$	E_4

[a] Activation energy of benzoyl peroxide decomposition measured at 146.0 kJ/mol by ref. [24]
[b] Standard reduction potential of $B(C_6F_5)_3$ measured at -1.79 V vs. ferrocene/ferrocenium in dichloromethane[11] and converted to -3.3 eV per ref. [25]

We chose regioregular (RR-) and regiorandom P3HT (RRa-P3HT) as the model polymers to determine if Lewis pairs can act as dopants. P3HT has an ionization energy of 5 eV[26] that is similar to that of decamethylferrocene, and RRa-P3HT has an ionization energy that is slightly higher while being more soluble in polar solvents. The solubility is important because doped solutions of RR-P3HT are prone to forming polar aggregates that precipitate from non-polar solvents.[3] We annotate the amount of dopant used by equivalents (eq.) relative to the number of repeat units of P3HT in the solution. For solutions doped with BCF and BPO, BPO was always added in half of the molar amount of BCF as required by the expected doping reaction mechanism (Scheme 3.2); to simplify, the notation "BCF:BPO" represents this 1:0.5 ratio. We adapted our solvent choice by dielectric constant in different experiments to accommodate the charged, doped polymers as much as possible, and to provide adequate signal in UV-Vis spectra.

We compared doping of P3HT by BCF and BCF:BPO by measuring the UV-Vis-NIR absorbance of doped P3HT solutions. We doped RR-P3HT with 0.1, 0.2, and 0.3 eq. of BCF (Figure 3.1a). We note that, while we used BCF that was received dry and prepared these solutions in a N_2 glovebox in anhydrous solvents, BCF can still scavenge even trace amounts of water in these environments.[9] With increasing amounts of BCF, we observed bleaching of

the neutral P3HT peak at 450 nm and increases in two lower-energy features at 550-650 nm and 650-1000 nm. The two peaks at 550-650 nm resemble the vibronic transitions associated with aggregated P3HT in solid-state films.[27] These peaks have been observed in BCF-doped RR-P3HT solution before and were found to be aggregates that could be filtered from the solution.[7] The feature at 650-1000 nm has been attributed to the absorbance of charged P3HT or P3HT polarons.[28] The relatively flat shape of this feature has been connected to delocalized polarons within P3HT aggregates.[7] With addition of both BCF and BPO, the neutral P3HT peak at 450 nm was further bleached while the aggregation feature at 550-650 nm and the polaron absorbance at 650-1000 nm increased. Compared to solutions doped with the same amount of BCF, the BCF:BPO-doped solutions had greater bleaching of neutral P3HT and greater increases in the lower-energy absorbances (Figure 3.1a & 3.1b). These spectra show that adding BPO increases the doping efficiency of BCF with RR-P3HT. When only BPO is added to the RR-P3HT solution, little change is observed in the spectrum.

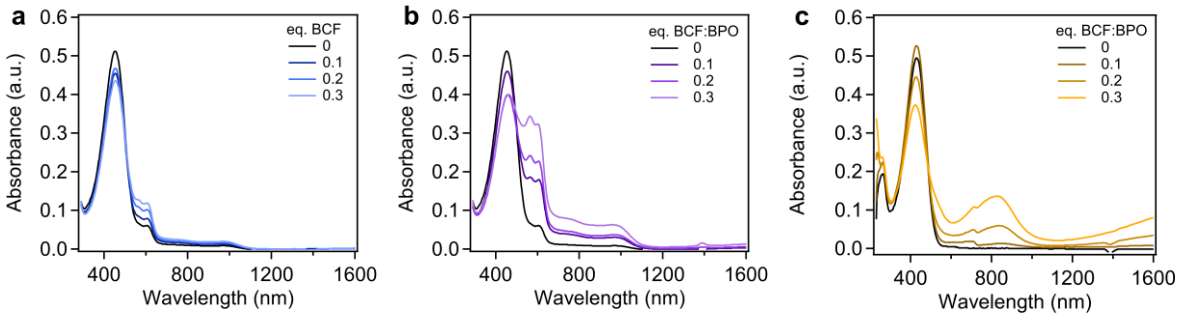

Figure 3.1. Solution UV-Vis spectra of (a) RR-P3HT doped with BCF, (b) RR-P3HT doped with BCF and BPO, and (c) RRa-P3HT doped with BCF and BPO. Solutions were measured at 0.0125 mg/mL of polymer in (a,b) chloroform or (c) dichloromethane. The small bumps in (c) spectra at 720 nm are due to spectrometer grating change.

To explore a more soluble alternative to RR-P3HT, we also examined the doping of RRa-P3HT with BCF:BPO in dichloromethane to help improve the solubility of the charged species. With increasing amounts of BCF:BPO, the absorbance of RRa-P3HT at 450 nm bleached, while lower-energy peaks at 550 nm, 850 nm, and above 1200 nm increased (Figure

3.1c). These changes show that BCF:BPO can dope RRa-P3HT, despite its slightly larger ionization energy than RR-P3HT.[26] The absorbance at 550 nm suggests that the doped RRa-P3HT began to aggregate in solution upon doping. Typically, the disorder in side chain position would prevent RRa-P3HT from crystallizing, but RRa-P3HT films have been observed to form ordered aggregates upon sequential F_4TCNQ doping.[29,30] The shape of the polaron absorbance at 850 nm is consistent with that for the localized polarons of RRa-P3HT.[8] The polaron absorbance above 1200 nm is also consistent with localized polarons because this peak redshifts with increasing polaron delocalization.[8,31] In our RR-P3HT spectra (Figs. 3.1a, 3.1b), only the tail of this absorbance is observed because the delocalized polaron absorbance would be expected at longer wavelengths than 1600 nm.

3.3.1 NMR Spectroscopy Confirms Counterion Formation

We used ^{1}H- and ^{19}F-NMR to confirm that the expected $[PhC(O)O\text{-}B(C_6F_5)_3]^-$ could be produced in a reaction of a semiconducting polymer with BCF and BPO. We chose RRa-P3HT because the signal from its aromatic protons is upfield from the peaks of BPO and it can dissolve in CD_2Cl_2 for easier comparison with the polar **C1**. Since dichloromethane has been shown to react with the BCF radical anion,[11] we expected to observe side products, alongside other potential interactions between BCF and water or oxygen. The paramagnetic species and electrostatic interactions in our system also interfered with interpretation of these spectra. The $[PhC(O)O\text{-}B(C_6F_5)_3]$ counterion is diamagnetic, but not much could be learned about the paramagnetic RRa-P3HT chains (see SI).

To compare the products of the RRa-P3HT, BCF, and BPO reaction to **C1**, we synthesized **C1** similar to the reported procedure.[22] The ^{19}F-NMR signals of **C1** (Fig. 3.2) were at -135 (d, *o*-C_6F_5), -163.4 (t, *p*-C_6F_5), and -167.6 ppm (t, *m*-C_6F_5), consistent with the

reported values.[22] The second set of signals is consistent with wet BCF[14] that likely formed when excess BCF starting material in the product was exposed to air. In the BCF:BPO-doped RRa-P3HT spectrum, peaks for the [PhC(O)O-B(C_6F_5)$_3$] anion appear shifted downfield by 0.3-0.4 ppm from **C1**'s peaks at -134.7, -163.1, and -167.2 ppm (Fig. 3.2, red bands). Because NMR signals are highly sensitive to the electronic environment, we expect shifts like these to result from differences in electronic localization or dielectric environment between samples. The ^{1}H-NMR peaks for [PhC(O)O-B(C_6F_5)$_3$]$^-$ in the RRa-P3HT mixture may be shifted upfield by 0.05-0.16 ppm from **C1**, but side products in the ^{1}H-NMR spectrum make it more difficult to interpret (see SI).

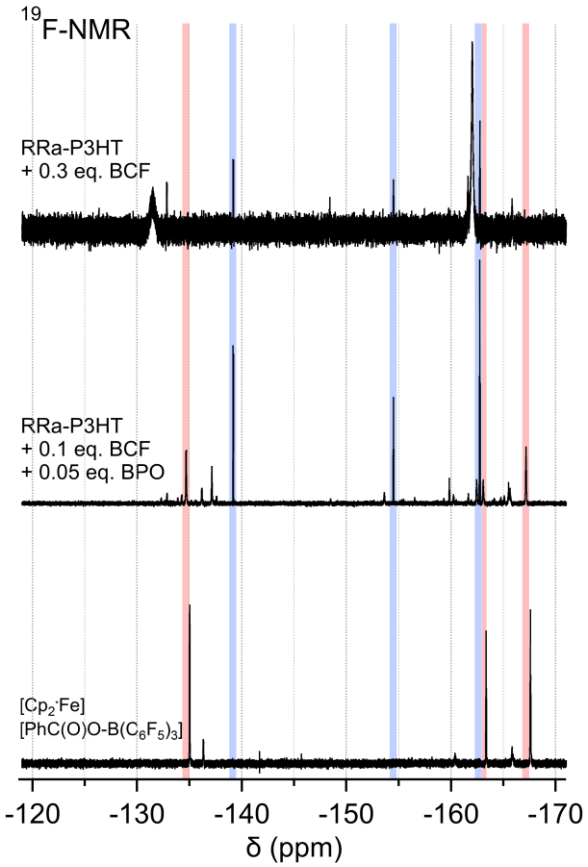

Figure 3.2. ^{19}F-NMR spectra of **C1** (bottom) and BCF:BPO- (middle) and BCF-doped RRa-P3HT (top) solutions in CD_2Cl_2. Red bands assigned to [PhC(O)O-B(C_6F_5)$_3$]$^-$ product. Blue bands indicate common side reaction product.

The ^{19}F-NMR spectrum for RRa-P3HT + 0.1 eq. BCF:BPO also has signals for several other products. The most noticeable is a doublet of multiplets at -139 ppm and complex multiplets at -154.5 and -162.7 ppm (blue bands) with a roughly 2:1:2 area ratio. While these peaks appear taller than the $[PhC(O)O\text{-}B(C_6F_5)_3]^-$ peaks in Fig. 3.2, the area ratio between the $[PhC(O)O\text{-}B(C_6F_5)_3]$ peaks and this product is 3:2. These peaks appear in many spectra, including RRa-P3HT + 0.3 eq. BCF and BCF:BPO, suggesting a common impurity of BCF not caused by side reactions with RRa-P3HT or BPO. Ruling those reactions out leaves reactions between BCF radical anions and the solvent, CD_2Cl_2, as the more likely cause. Five products of reduced BCF and dichloromethane (DCM) have been tentatively identified,[11] but the *ortho*-F signals for these products are all 4-7 ppm downfield of our product's doublet signal. Our BCF-CD_2Cl_2 product may be different from the previously identified BCF-DCM products, or the signal may be shifted by electronic or hydrogen isotope effects. The assigned BCF-CD_2Cl_2 peaks (blue bands) did not appear in the **C1** spectrum (Fig. 3.2), as would be expected for a BCF-CD_2Cl_2 side product. However, unlike these reaction mixtures prepared directly in CD_2Cl_2, the **C1** powder was precipitated and washed with pentane before measurement, which could have removed this side product.

3.3.2 Lewis Pair Dopes a Range of Polymers

We tested BCF:BPO doping on several other conjugated polymers with a range of backbone structures and ionization energies. We note that the BCF used for these experiments was found to have a higher water content than those in Figure 3.1 and we make the distinction by noting the dopant as BCF·$(H_2O)_x$. ^{19}F-NMR peaks of this BCF·$(H_2O)_x$ in CD_2Cl_2 shifted further upfield than those of BCF·(H_2O),[14] indicating that our BCF·$(H_2O)_x$ contained more than 1 eq. of water ($x > 1$).(see SI) Because water atoms are loosely bound to BCF and the

BCF:BPO reaction is expected to be more energetically favorable, we did not expect the presence of water to inhibit the BCF:BPO reaction. First, we examined the reaction of $BCF{\cdot}(H_2O)_x$:BPO and $BCF{\cdot}(H_2O)_x$ with the donor-acceptor co-polymer indacenodithiophene-*co*-benzothiadiazole with ethylhexyl side chains (C_2C_6-IDTBT). C_2C_6-IDTBT has an ionization energy of 5.3 eV,[32] and its benzothiadiazole unit provides the potential ability to complex with BCF. Little doping was observed from $BCF{\cdot}(H_2O)_x$ alone in chlorobenzene solution (Fig. 3.3a). When $BCF{\cdot}(H_2O)_x$:BPO was used for doping, the main absorbances at ~400 nm and ~650 nm were bleached while new peaks appeared at ~1050 and 1600 nm. The spectrum of doped IDTBT was consistent with bleaching of the main transition and an increase in subgap absorption peaked at 1100 nm in charge accumulation spectroscopy of an IDTBT field effect transistor.[33] These changes again indicate that $BCF{\cdot}(H_2O)_x$:BPO was a more efficient dopant for IDTBT than $BCF{\cdot}(H_2O)_x$.

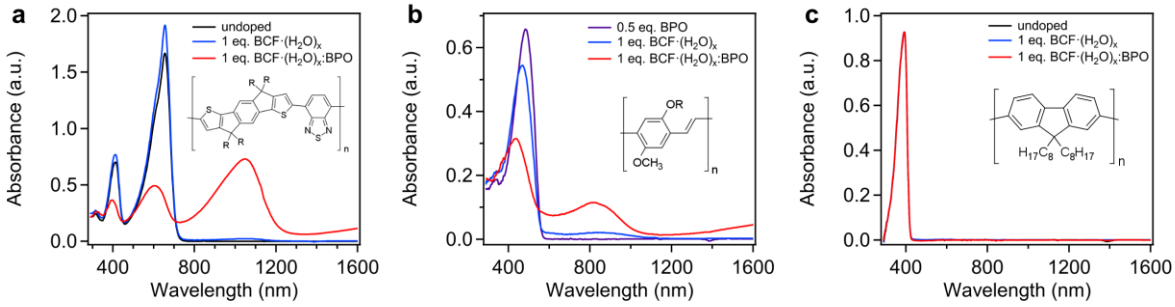

Figure 3.3. Solution UV-Vis spectra of (a) IDTBT, (b) MEH-PPV, and (c) PFO mixed with $BCF{\cdot}(H_2O)_x$ or $BCF{\cdot}(H_2O)_x$:BPO at 0.02 mg/mL of polymer in chlorobenzene. R = 2-ethylhexyl.

To examine doping of a polymer without Lewis basic heteroatoms in the backbone, we chose poly[2-methoxy-5-(2-ethylhexyloxy)-1,4-phenylenevinylene] (MEH-PPV). MEH-PPV has a comparable ionization energy (5.3 eV) to IDTBT.[34] After mixing MEH-PPV with $BCF{\cdot}(H_2O)_x$ in chlorobenzene solution, only a weak new absorbance was observed ~850 nm (Fig. 3.3b). When MEH-PPV was mixed with $BCF{\cdot}(H_2O)_x$ and BPO (Fig. 3.3b), the polymer absorbance at 500 nm was bleached and blue-shifted, while new absorbances appeared at ~850

and 1600 nm. These changes match those observed for doping of MEH-PPV with the oxidant Magic Blue.[34] Again, BCF:BPO is a more efficient dopant than $BCF\cdot(H_2O)_x$.

To test the limits of doping, we choose polyfluorene, PFO, which has a large ionization energy at 5.8 eV[35] and no heteroatoms. Upon addition of $BCF\cdot(H_2O)_x$ and $BCF\cdot(H_2O)_x$:BPO in chlorobenzene solution (Fig. 3.3c), no changes in the spectra were observed. This lack of an observed doping reaction provides a bound for the reaction E_4 to be between -2.8 and -3.3 eV and that the next reaction of BCF:BPO can oxidize donors with IE_D less than 5.8 eV.

3.3.3 Structure of Doped Films Becomes More Disordered with Increasing Dopant

After confirming that BCF:BPO is an effective dopant for a range of semiconducting polymers in solution, we examined how this doping process affects solid state properties. The relatively large $[PhC(O)O\text{-}B(C_6F_5)_3]^-$ counterion (≈1.2 nm long) could disrupt ordering in the solid state. We chose to focus on RR-P3HT for comparison to studies of doping with BCF alone and other large dopants. In the neat RR-P3HT film, we observed the expected P3HT spectrum with vibronic features indicative of aggregation into crystallites (Fig. 3.4a).[27,36] As the dopant ratio increased, the polymer absorbance decreased while two features, labeled P1 and P2 and attributed to the polarons, increased. At 1 eq. BCF:BPO doping, the P3HT peak was completely bleached. The strongest absorbance is centered at 0.6 eV while P1a and P2 decrease below the 0.2 eq. BCF:BPO spectrum. The decreases in P1a and P2 suggest that the amount of polarons in the film is decreasing. DFT calculations of oxidized polyethylenedioxythiophene chains suggest that, below 33% oxidation, the two polaron transitions will shift towards each other due to mixed valency along the chain. At 33% oxidation, the chain is a closed-shell singlet with one optical transition.[37] Based on these calculations, our 1 eq. BCF:BPO-doped film could contain a mix of intermediate open-shell

P3HT oxidation states with interacting polarons, such as paired polarons. Similar spectra have been observed in intermediate electrochemically doped P3HT[38,39] and polythiophene,[40] as well as $FeCl_3$-doped P3HT.[41]

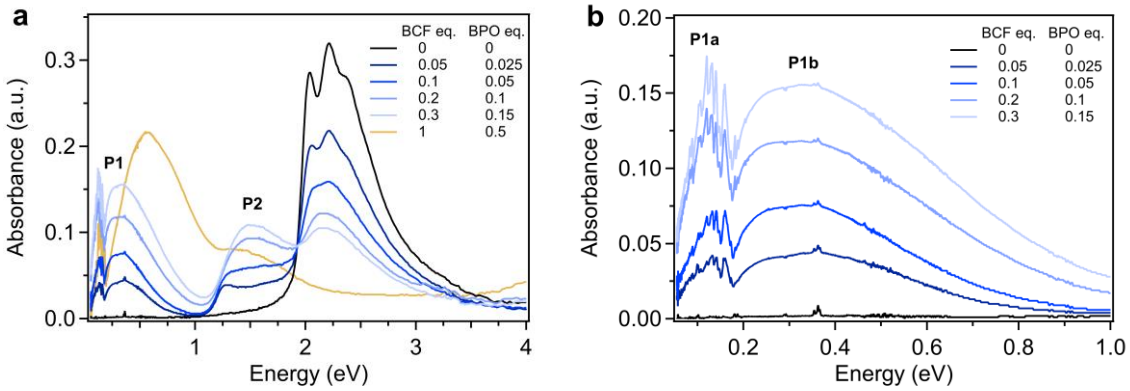

Figure 3.4. (a) Full and (b) IR region of combined film UV-Vis and FTIR spectra of BCF:BPO-doped RR-P3HT films cast from 9:1 v/v chloroform:acetonitrile solution on KBr plates.

In our 0.05 – 0.3 eq. BCF:BPO-doped films, P1 and P2 can provide information about the morphology of the films and the delocalization of the polarons. Computations and experiments have shown that the shape of P1 changes with the delocalization of the polaron and distance of the counter-anion to the polaron.[31,42,43] As polaron delocalization increases, P1a (0.1 eV) is predicted to redshift and increase, while P1b (0.2-1 eV) also redshifts with more sensitivity to the polaron-anion distance.[31] In all of our film spectra, the locations of P1a and P1b, as well as their relative ratios, were consistent with highly delocalized polarons (Figure 3.4b). The peak of P1b is at 0.34-0.36 eV. This location matches that seen in P3HT doped with dodecaborane dopants with diameters ≈2 nm.[44] We fit P1 in our data with several Gaussian functions to calculate the area of the peaks (see SI). We found that the area on the high-energy side of P1b increased disproportionately to the rest of P1 with doping. A shoulder in P1 at 0.8-1 eV has been observed in F_4TCNQ-doped P3HT and was attributed to localized

polarons that are closer to the F_4TCNQ^- counterion.[45] Alternately, a blueshift in P1 could be caused by higher open-shell oxidation states, as in the 1 eq. BCF:BPO-doped spectrum.

The shape of P2 has been connected to the degree of aggregation in P3HT solutions. In our BCF:BPO-doped films (Fig. 3.4a), P2 in the two lower doped films is a relatively flat shoulder. In the two more highly doped films, an absorbance peak at 1.5 eV is the predominant feature in P2. This trend of P2 changing shape with increasing doping has been observed before in $FeCl_3$- and $NOPF_6$-doped P3HT films.[41,46] In experiments with BCF-doped P3HT solutions, the flat shoulder was associated with aggregates that can be filtered out of the solution.[7] Comparisons of doped regioregular and RRa-P3HT solutions showed that regioregular P3HT had a relatively flat P2, while RRa-P3HT's P2 had a peak centered at 1.5 eV.[8] Based on these findings, the change in shape of P2 in our films (Fig. 3.4a) at the higher doping levels could indicate that more amorphous areas of the films were doped. With the high-energy increase in P1b, the shape changes in P1b and P2 could indicate that, as doping increases, polarons increasingly form in the amorphous areas of the film.

To check the effects of BCF and BCF:BPO doping on the structure of the thin films, we performed grazing incidence wide-angle X-ray scattering (GIWAXS). The RR-P3HT film (Fig. 3.5a) had an alkyl stacking distance of q_z = 16.2 Å and a π-π stacking distance of q_{xy} = 3.88 Å, indicating "edge-on" crystallites. These stacking distances are consistent with typical values for P3HT.[47] In doped films with BCF or BCF:BPO, the alkyl stacking distance increased, and the π-π stacking distance decreased (Table 3.2). These changes in stacking distances are consistent with dopants being incorporated into P3HT crystallites between the alkyl chains.[47] In the film cast from P3HT solution doped with 0.1 eq. BCF:BPO (Fig. 3.4b), the edge-on crystalline texture is still present with alkyl stacking of 19.0 Å and π-π stacking

of 3.80 Å. This increase in alkyl stacking was larger than in the equivalent 0.1 eq. BCF-doped film (Table 3.2). The larger $[PhC(O)O\text{-}B(C_6F_5)_3]^-$ counterion or the greater doping efficiency of BCF:BPO could cause this larger increase in alkyl stacking.

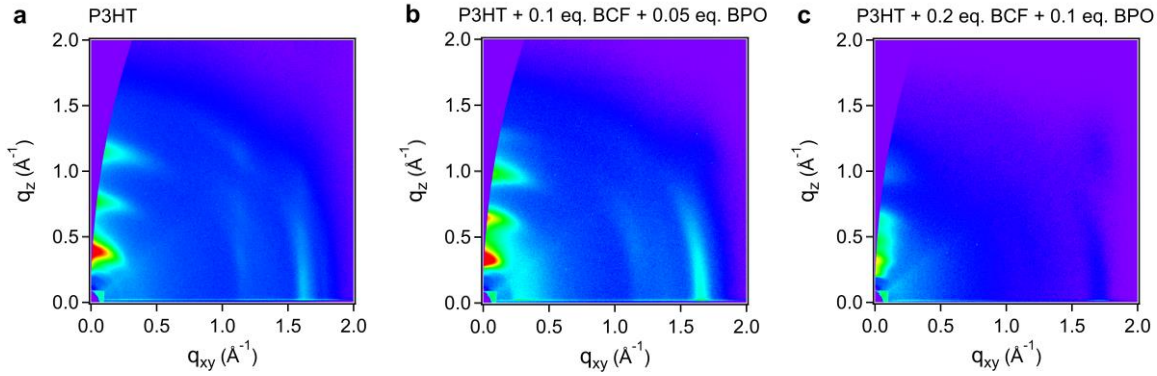

Figure 3.5. Grazing incidence wide-angle X-ray scattering images of (a) undoped RR-P3HT and RR-P3HT films doped with (b) 0.1 eq. BCF:BPO and (c) 0.2 eq. BCF:BPO. Narrower color scale was used for (c) to highlight the weaker scattering features.

Table 3.2. Alkyl and π-π stacking distances of BCF- and BCF:BPO-doped RR-P3HT films extracted from GIWAXS scattering images. (See SI for images)

	Alkyl Stacking (Å)	π-π Stacking (Å)		Alkyl Stacking (Å)	π-π Stacking (Å)
RR-P3HT	16.2	3.88			
0.05 eq. BCF	16.7	3.85	0.05 eq. BCF:BPO	17.5	3.79
0.1 eq. BCF	17.0	3.70	0.1 eq. BCF:BPO	19.0	3.80
0.2 eq. BCF	18.3	3.78	0.2 eq. BCF:BPO	19.5	3.67
0.3 eq. BCF	18.8	3.75	0.3 eq. BCF:BPO	18.5	3.75

At the higher doping level of 0.2 eq. BCF:BPO, greater changes in film structure were observed (Fig. 3.5c). The scattering peaks became less intense and more difficult to distinguish. This decrease in scattering intensity indicates a decrease in structural ordering in the film. The stacking distances could still be extracted, with alkyl stacking at 19.5 Å with π-π stacking at 3.67 Å. In a previous study of BCF-doped P3HT, films also became increasingly disordered with doping, and alkyl stacking distances up to 19.2 Å were observed.[6] Our 0.2 eq. BCF:BPO-doped film had additional scattering at q_z = 0.48 Å^{-1} between the first two alkyl stacking peaks. This scattering could correspond to a stacking distance of 13 Å. Given the

length of $[PhC(O)O\text{-}B(C_6F_5)_3]^-$ is about 12 Å, this peak could be from scattering between counterions and polymer chains. Alternately, this peak could be the alkyl stacking peak of a second phase, as in dodecaborane-doped P3HT.[44] Overall, the scattering changes significantly between the 0.1 eq. and 0.2 eq. levels of BCF:BPO. This change corresponds with the change in the UV-Vis spectra at 1.5 eV associated with more localized polarons (Fig. 3.4). Together, these changes indicate that the increase in disorder and in localized polarons with doping are connected.

3.3.4 Co-doping with BCF Lead to High Conductivity Films

We measured the in-plane conductivity of BCF- and BCF:BPO-doped RR-P3HT films using the four-point probe method (Fig. 3.6). At and above 0.1 eq. BCF, doping with BCF:BPO increased the conductivity of the films over those doped with BCF alone. The maximum conductivity measured was 25 ± 6 S/cm for the film doped with 0.2 eq. BCF:BPO. While the more disordered morphology measured in Fig. 3.5c could be expected to be detrimental for hole transport, we measured the highest conductivities for the 0.2 eq. BCF:BPO- and 0.3 eq. BCF:BPO-doped films. The increase in carrier concentration at these doping levels may offset the disruption in order, or the disordered morphology of Fig. 3.5c may be deceptively beneficial for charge transport. For example, formation of localized polarons at higher doping levels could disrupt aggregate formation while creating more intercrystallite transport pathways.

The electrical conductivities from this solution-based doping route compare favorably with other dopants and processing routes. One of the highest reported values of conductivity for P3HT doped with BCF is 33 S/cm; this value was achieved with 120% BCF, which implies that the amount of BCF and polymer were nearly equivalent in the solid.[6] P3HT solution-

doped with F_4TCNQ has been reported to have conductivity up to 8.0 S/cm at 17 mol% F_4TCNQ,[48] with conductivity observed to decrease at F_4TCNQ mole fractions above 0.17.[49] The improvement in the maximum conductivity of BCF:BPO solution-mixed doping over F_4TCNQ could be due to the greater effective electron affinity of BCF:BPO doping P3HT to a higher carrier concentration or due to the potentially higher solubility of BCF allowing more doped P3HT to stay solvated, thereby improving processability. Our results are also comparable to sequentially dodecaborane-doped P3HT films with conductivity up to 12.8 S/cm.[50]

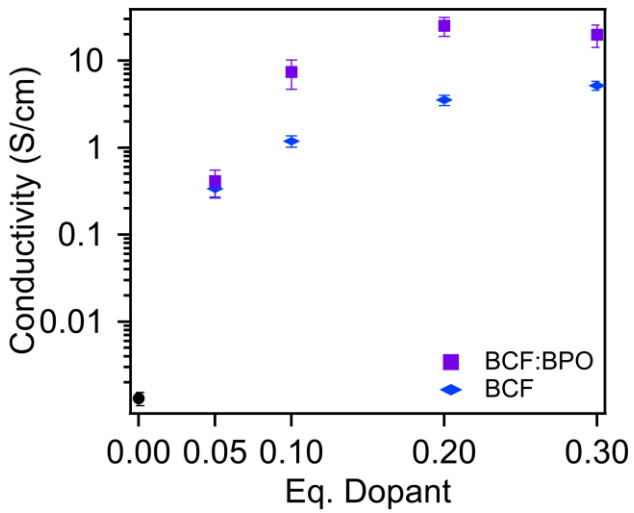

Figure 3.6. Conductivity of BCF- (blue circles) and BCF:BPO-doped (purple squares) RR-P3HT films cast from doped solution. Error bars were calculated by error propagation of the standard deviation of three measurements on each film and the film roughness.

3.4. Conclusions

We have demonstrated that single electron transfer from a Lewis acid-base pair, BCF:BPO, is a route to new dopants that increase the efficiency of doping over a Lewis acid, BCF, alone. The BCF:BPO combination can dope semiconducting polymers with various backbone structures up to ionization energies of at least 5.3 eV. Using ^{19}F-NMR spectroscopy, we found the expected counterion product, $[PhC(O)O\text{-}B(C_6F_5)_3]^-$. Despite the relatively large

size of the counterion, films of P3HT doped with BCF:BPO had high electrical conductivities of 25 ± 6 S/cm with 0.2 eq. of dopant. Optical spectroscopy showed that the films have highly delocalized polarons with the proportion of more localized polarons increasing with increasing doping. These localized polarons suggest that, above some threshold, polarons increasingly form in amorphous areas of the films with increasing disruption of the crystallite structure. Given that the P3HT film conductivity is higher than that with F_4TCNQ or BCF doping from solution, these localized polarons and disruption in ordering do not seem to be detrimental to electrical transport.

Our results show that LPs can be used to *p*-type dope semiconducting polymers and the addition of BPO can improve the doping efficiency and effective electron affinity over BCF alone. The energetic stabilization of B-O bond formation in the proposed reaction mechanism drives the doping reaction, in contrast to the unclear doping mechanism of BCF alone. The many Lewis bases that have already been demonstrated to stabilize one-electron oxidation with BCF offer further ways to adjust the effective electron affinity and counterion size during doping.[20,22,23,51] Similar Lewis acids, such as $Al(C_6F_5)_3$ and $Zn(C_6F_5)_3$, may be useful in doping, as well.[22,52,53] Like F_4TCNQ, BCF can be sublimated, so vapor infiltration of BCF may offer an additional route to optimize processing of LP-doped films. With this new LP route to oxidizing polymers, even more dopants with the desired properties for electronic and thermoelectric devices may be found.

3.5. Acknowledgements

This work was supported by the National Science Foundation (NSF) under DMR 1808622. Portions of this work were carried out at the MRL Shared Experimental Facilities, supported by the NSF MRSEC program under award no. DMR 1720256. Use of the Stanford

Synchrotron Radiation Lightsource, SLAC National Accelerator Laboratory, is supported by the U.S. Department of Energy, Office of Science, Office of Basic Energy Sciences under Contract No. DE-AC02-76SF00515. Use was made of computational facilities purchased with funds from the National Science Foundation (CNS-1725797) and administered by the Center for Scientific Computing (CSC). The CSC is supported by the California NanoSystems Institute (CNSI) and the MRSEC (NSF DMR 1720256) at UC Santa Barbara.

3.6. Appendix S2: Supplementary Information

3.6.1 Additional P3HT Spectra

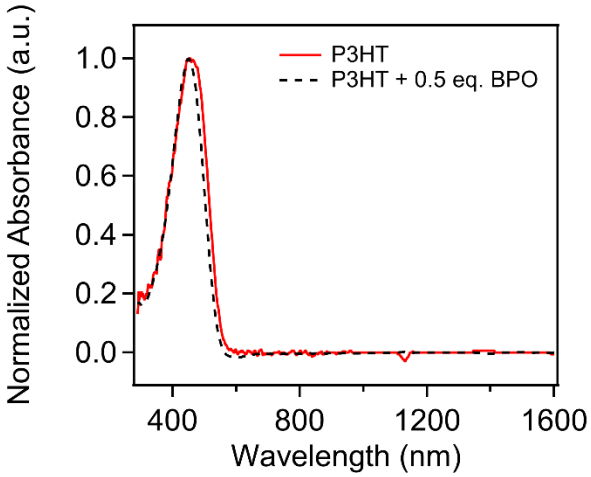

Figure S 2.1. Normalized absorbance spectra of P3HT and P3HT + 0.5 eq. BPO in chlorobenzene solution.

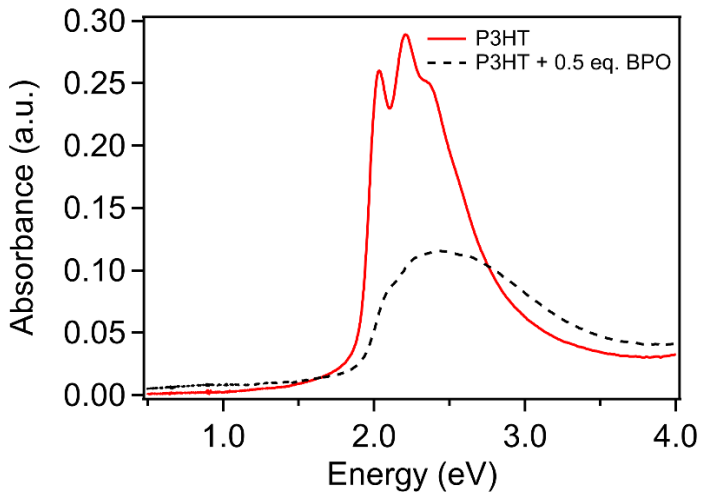

Figure S 2.2. UV-Vis-NIR spectra of P3HT and P3HT + 0.5 eq. BPO films cast from 9:1 CF:ACN on quartz substrates.

3.6.2 Analysis of ^{1}H-NMR Spectra

RRa-P3HT's most downfield thiophene proton signal is at 7.09 ppm, upfield of BPO's peaks, so the polymer peaks will not overlap with counterion peaks. In the BCF- and BPO-doped RRa-P3HT spectrum (Fig. S2.3), a doublet signal at 8.01 ppm and triplet signals at 7.42 and 7.34 ppm have apparently similar coupling to the signals of **C1**, although shifted 0.1-0.15 ppm upfield (red dashed lines). These peaks are not present in any of the control spectra (Fig. S2.3), suggesting that they are the result of a reaction that only occurs when all of RRa-P3HT, BCF, and BPO are present. The small upfield shift of the anion peaks may be due to the different cation-anion distances in the solution of **C1** and doped RRa-P3HT.

The BCF- and BPO-doped RRa-P3HT spectrum also has several more peaks, indicating that some side reactions occur. Comparison to the control spectra provides some insight into the origin of the side reactions. The set of doublet-triplet-triplet peaks at 8.06, 7.62, and 7.49 ppm roughly matches a broad set of peaks in the RRa-P3HT and BPO control spectrum (Fig. S2.3). The presence of these signals in the doped RRa-P3HT spectrum indicates some benzoyl peroxide reacted with the polymer chains, possibly along degradation mechanisms similar to (photo)oxidation of P3HT. The small doublet seen in the BCF- and BPO- doped RRa-P3HT spectrum at 8.17 ppm matches the BCF-BPO control spectrum (Fig. S2.3), indicating that a small amount of BCF-BPO complexes may form as a side product, as well.

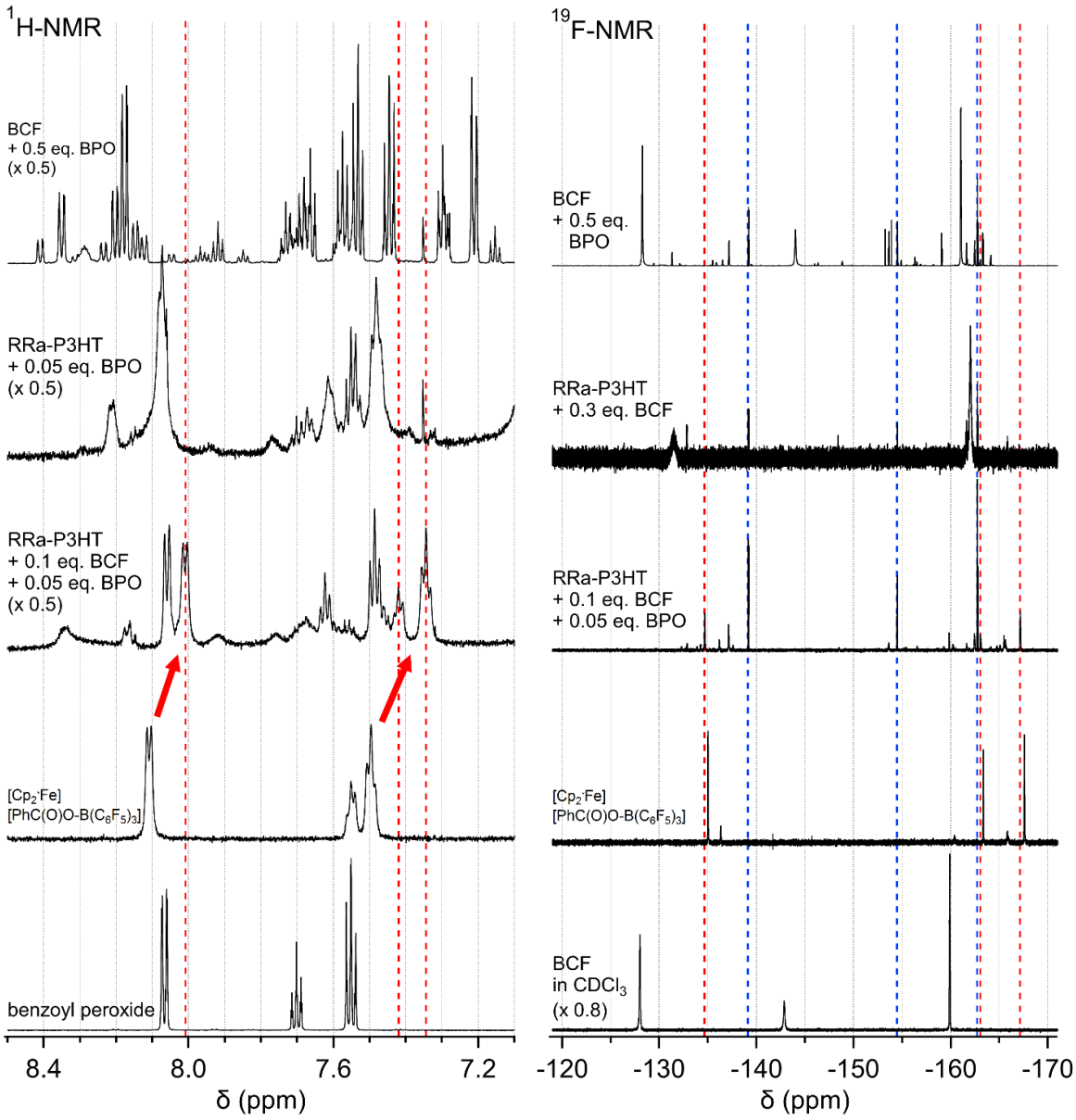

Figure S 2.3. ^{1}H- and ^{19}F-NMR spectra of BCF- and BPO-doped RRa-P3HT and relevant control solutions in CD_2Cl_2 (except BCF solution in $CDCl_3$). Red dashed lines indicate peaks attributed to [PhC(O)O-B(C_6F_5)$_3$] doping product. Blue dashed lines indicate common side reaction product.

3.6.3 NMR Spectra

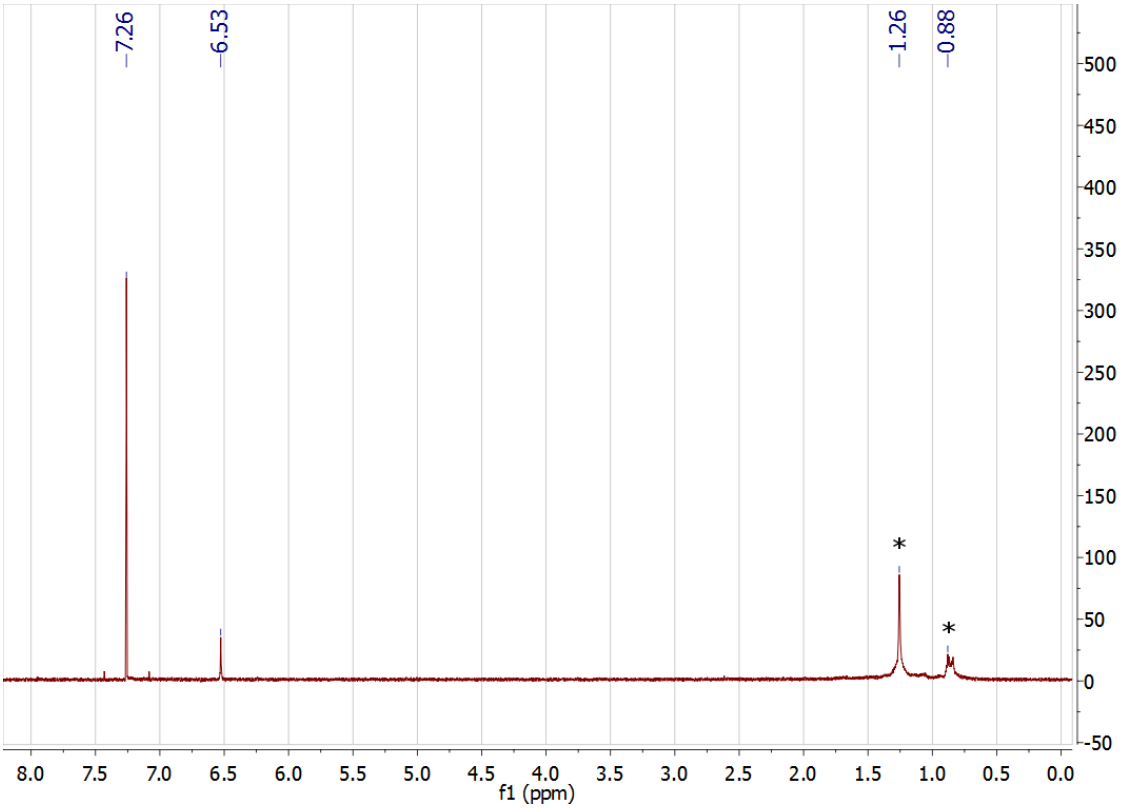

Figure S 2.4. ^{1}H-NMR spectrum of BCF (TCI America, after opening) in $CDCl_3$. Asterisks indicate hydrocarbon grease introduced during sample prep.

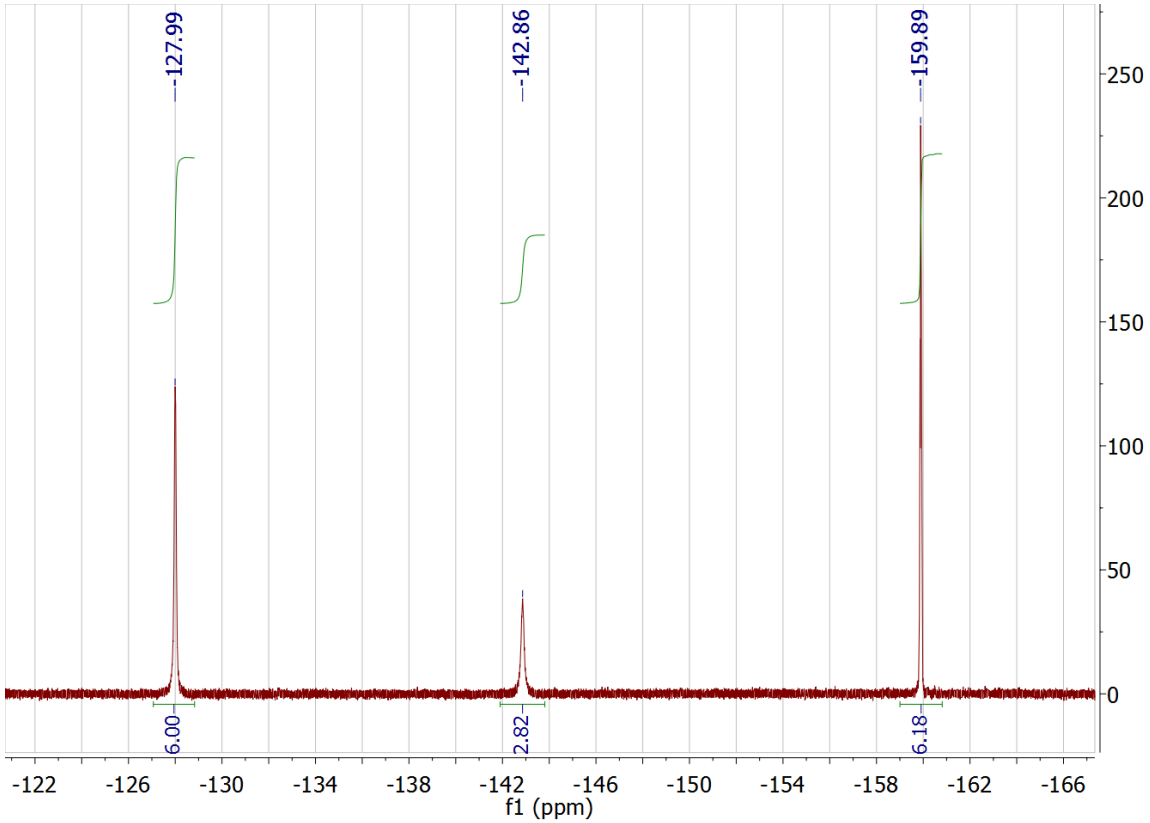

Figure S 2.5. ^{19}F-NMR spectrum of BCF (TCI America, after opening) in $CDCl_3$.

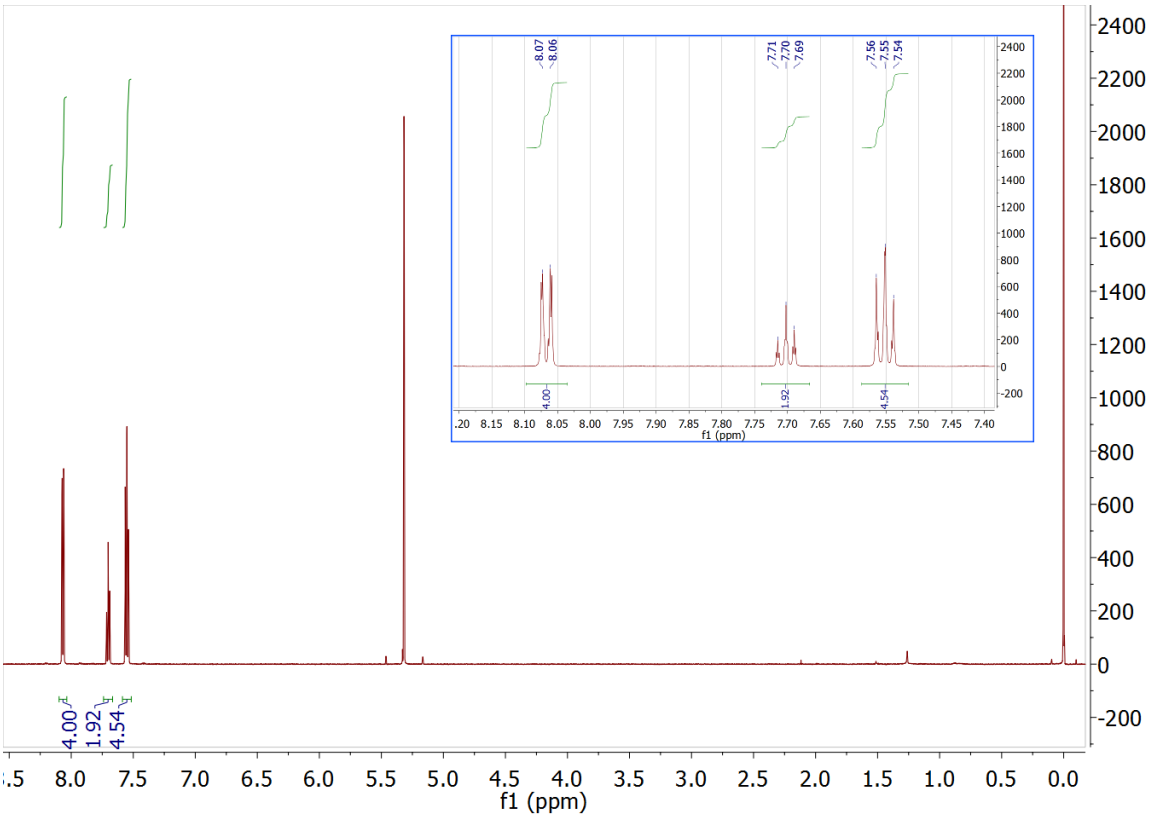

Figure S 2.6. ^{1}H-NMR spectrum of benzoyl peroxide in CD_2Cl_2. Inset highlights aromatic peaks.

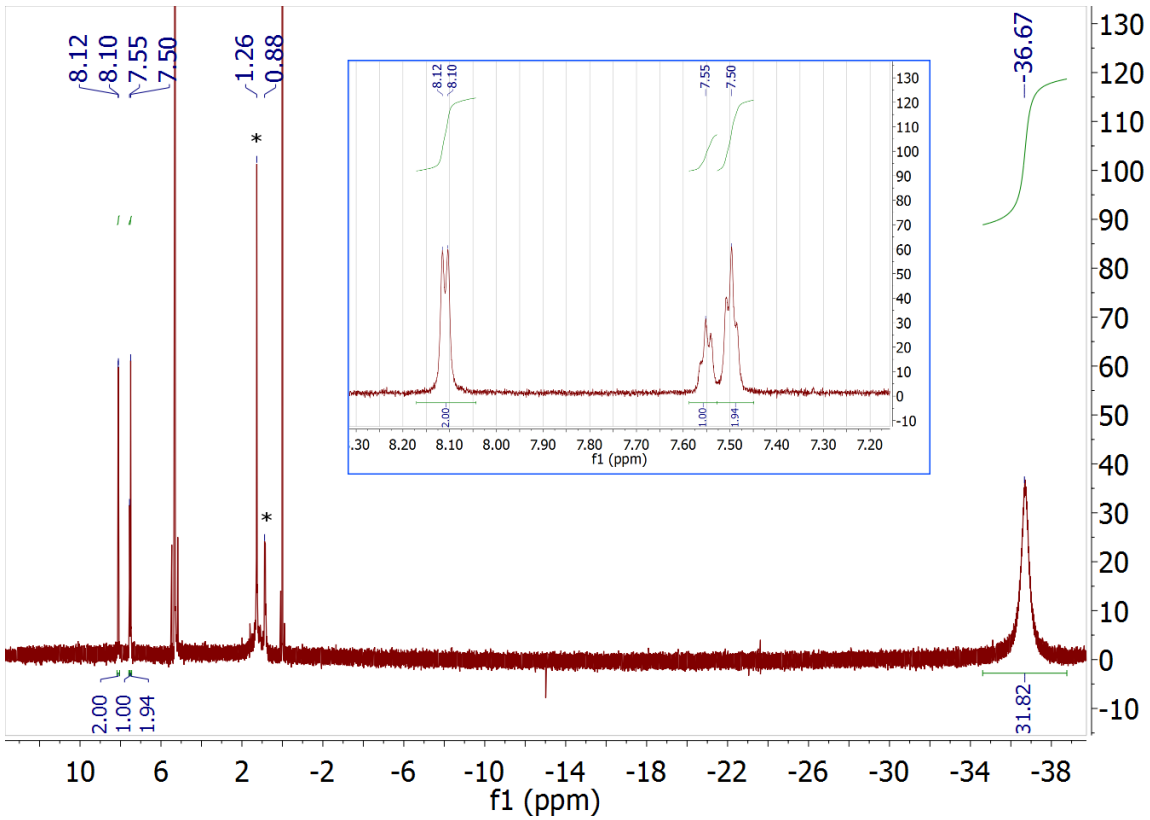

Figure S 2.7. ^{1}H-NMR spectrum of C1 in CD_2Cl_2. Asterisks indicate hydrocarbon grease. Inset highlights aromatic peaks.

With a 600 MHz NMR spectrometer, we were able to resolve the three aromatic ^{1}H features. **C1** has a doublet centered at 8.11 ppm and asymmetric triplets at 7.55 and 7.50 ppm in the expected 2:1:2 peak area ratio, respectively.

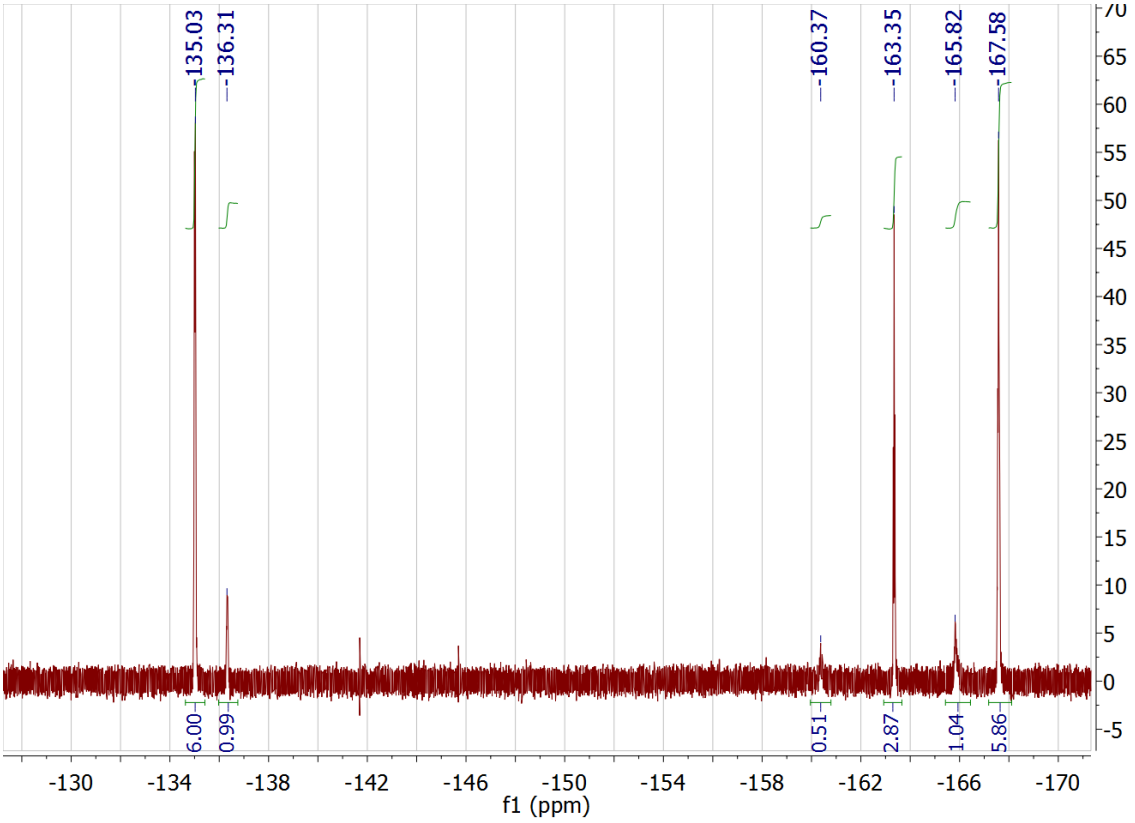

Figure S 2.8. ^{19}F-NMR spectrum of C1 in CD_2Cl_2.

C1 has three signals in its ^{19}F-NMR spectrum at -135, -163.4, and -167.6 ppm, consistent with the reported synthesis. The smaller second set of peaks in the spectrum for **C1**, at -136, -160, and -166 ppm, are likely from wet BCF. If excess unreacted BCF remained in the sample of **C1**, that excess BCF would have absorbed water when the powder of **C1** was washed and filtered in air.

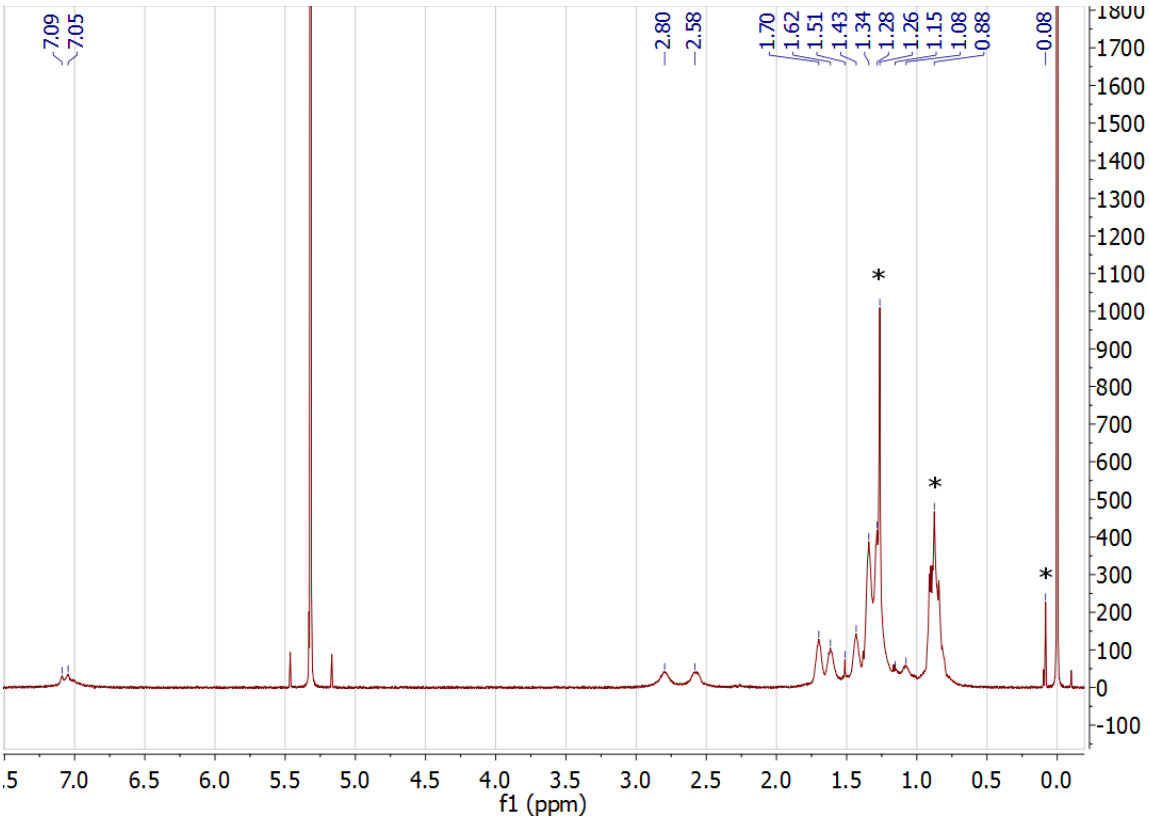

Figure S 2.9. ^{1}H-NMR spectrum of RRa-P3HT in CD_2Cl_2. Asterisks indicate hydrocarbon grease and silicone grease.

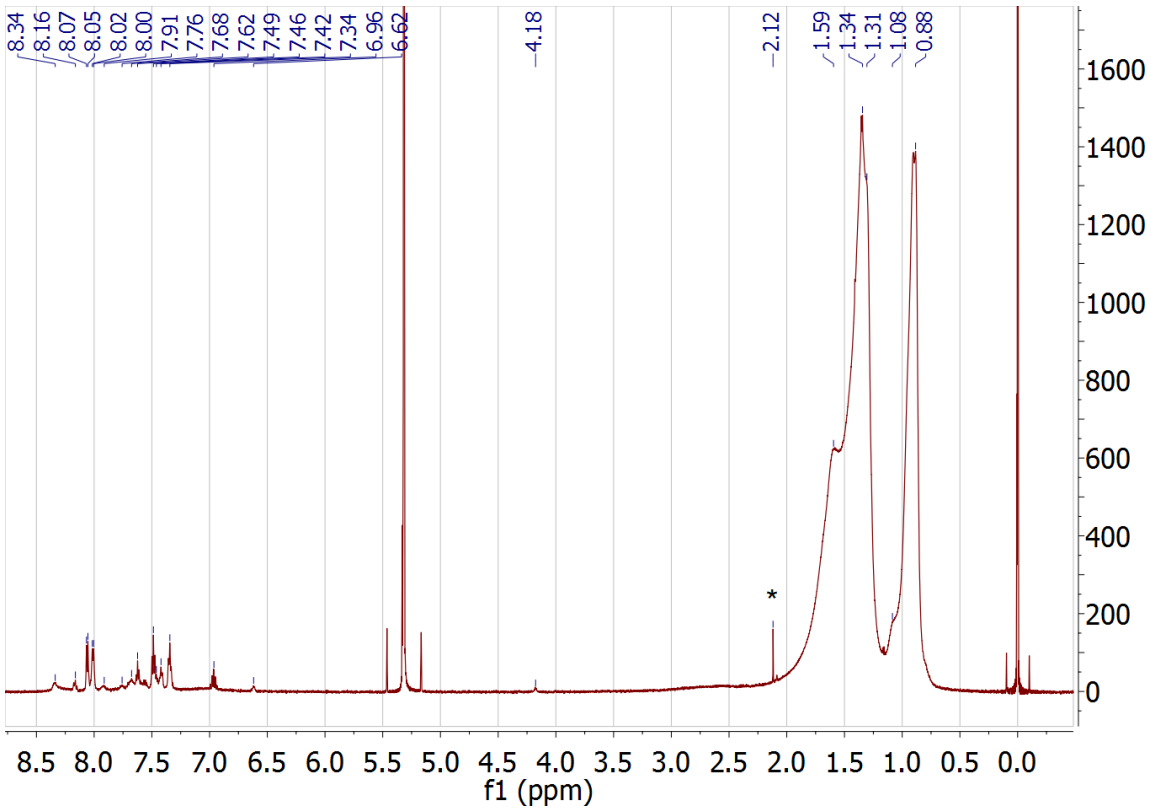

Figure S 2.10. ^{1}H-NMR spectrum of RRa-P3HT + 0.1 eq. BCF + 0.05 eq. BPO in CD_2Cl_2. Asterisk indicates acetone.

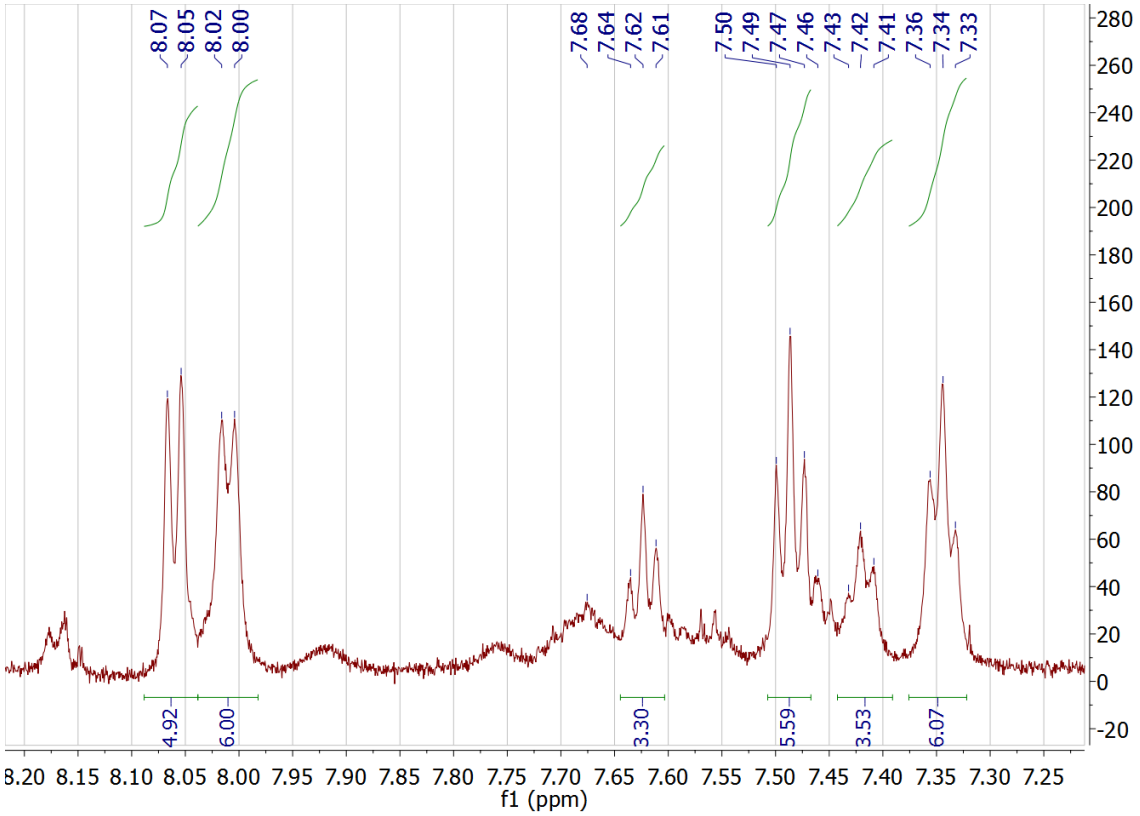

Figure S 2.11. Aromatic region of ^{1}H-NMR spectrum of RRa-P3HT + 0.1 eq. BCF + 0.05 eq. BPO in CD_2Cl_2.

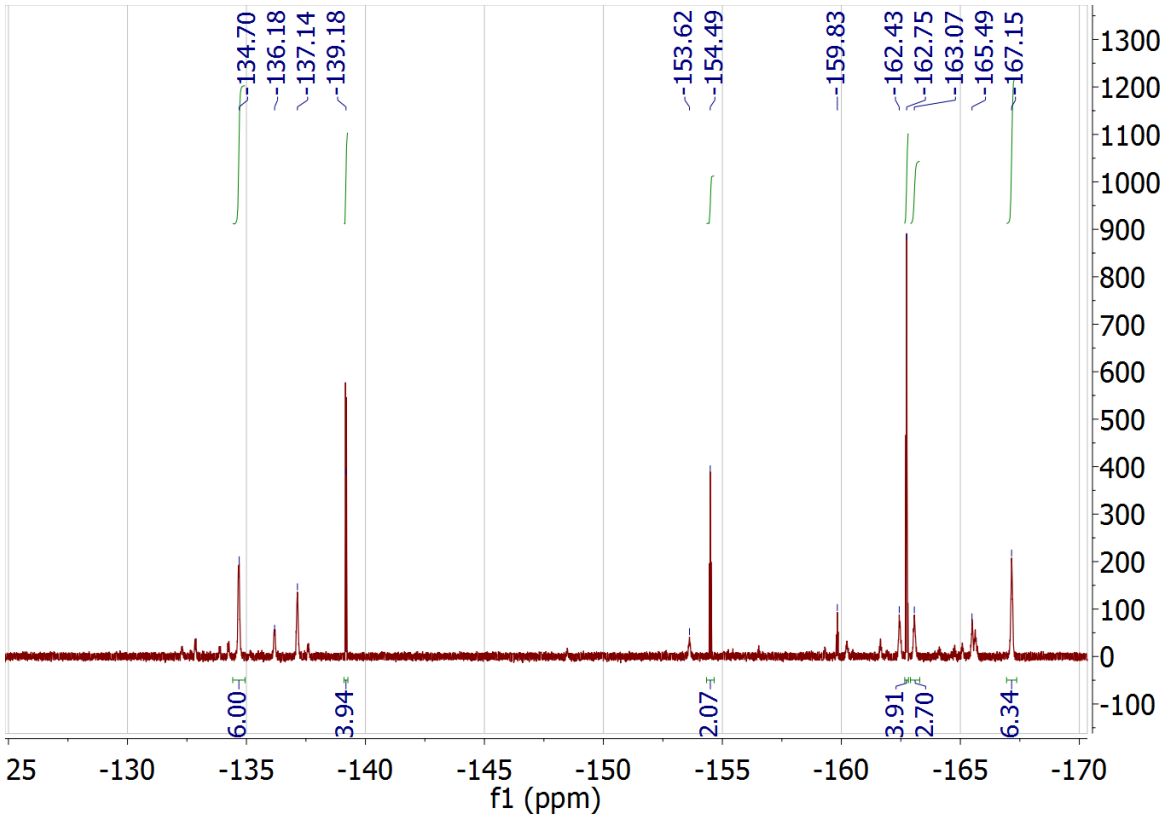

Figure S 2.12. ^{19}F-NMR spectrum of RRa-P3HT + 0.1 eq. BCF + 0.05 eq. BPO in CD_2Cl_2.

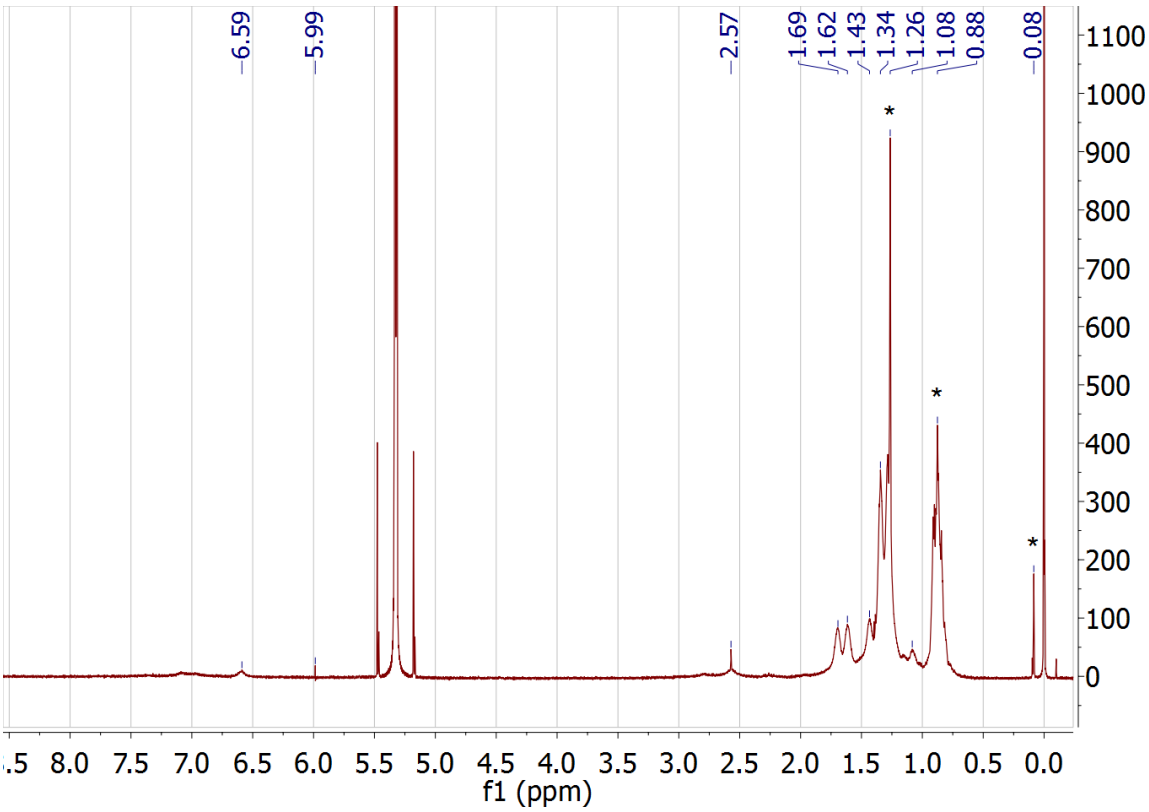

Figure S 2.13. ^{1}H-NMR spectrum of RRa-P3HT + 0.3 eq. BCF in CD_2Cl_2. Asterisks indicate hydrocarbon grease and silicone grease.

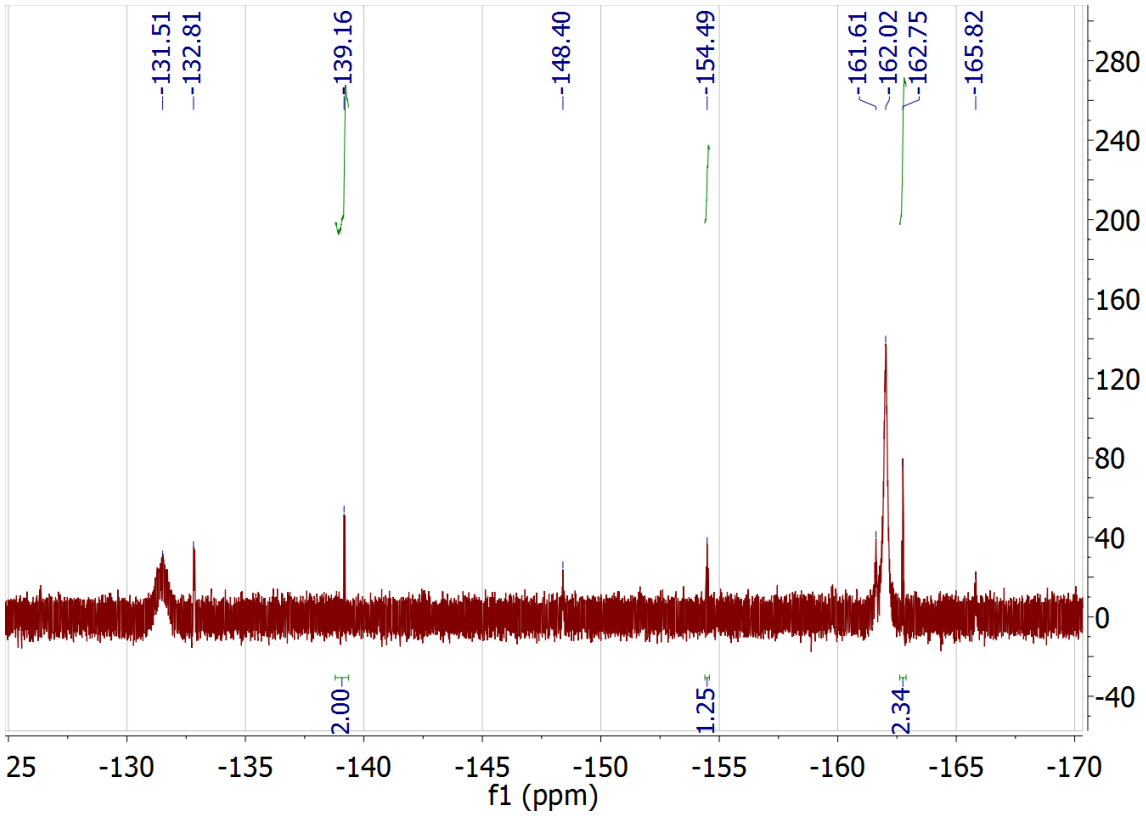

Figure S 2.14. ^{19}F-NMR spectrum of RRa-P3HT + 0.3 eq. BCF in CD_2Cl_2.

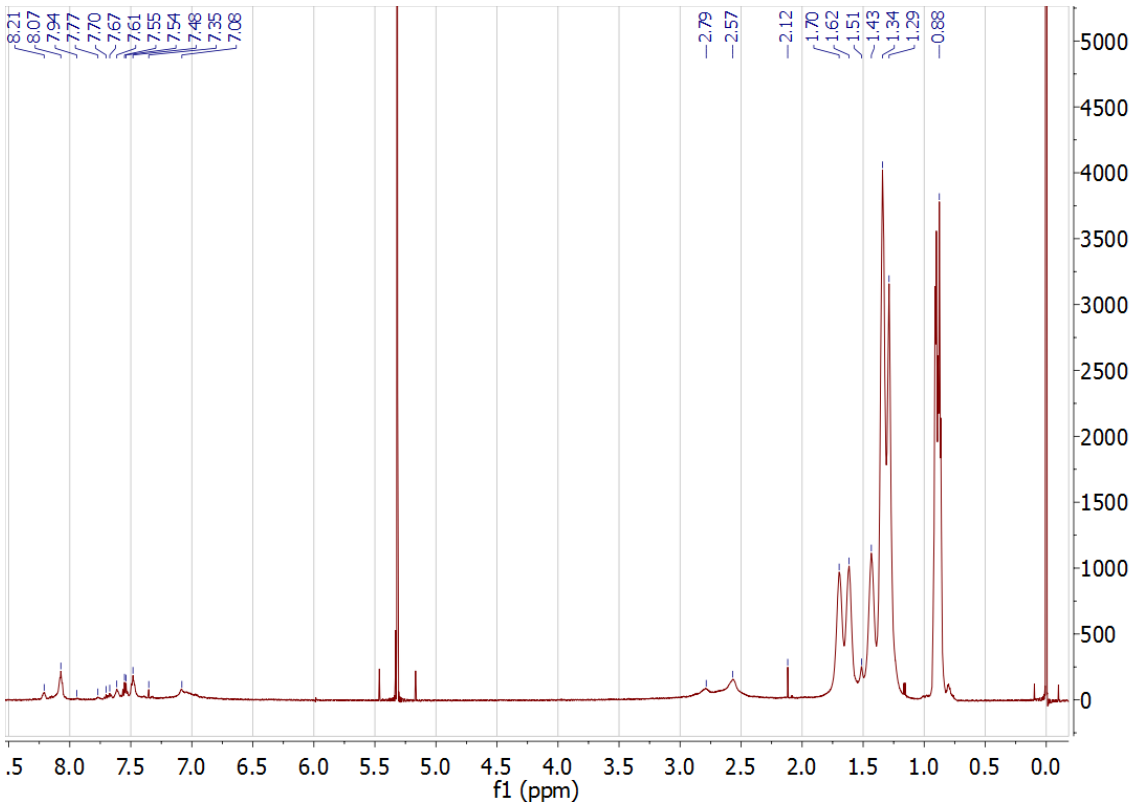

Figure S 2.15. ^{1}H-NMR spectrum of RRa-P3HT + 0.05 eq. BPO in CD_2Cl_2.

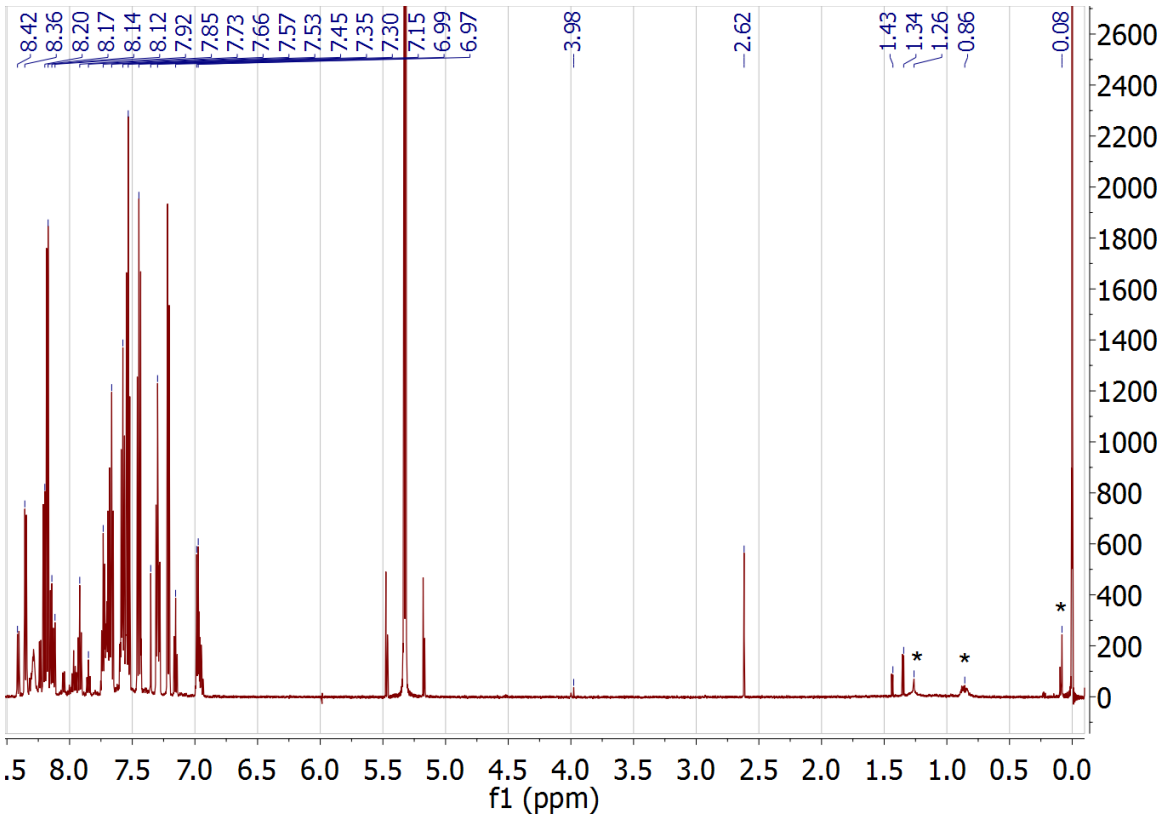

Figure S 2.16. ^{1}H-NMR spectrum of BCF + 0.5 eq. BPO in CD_2Cl_2. Asterisks indicate hydrocarbon grease and silicone grease.

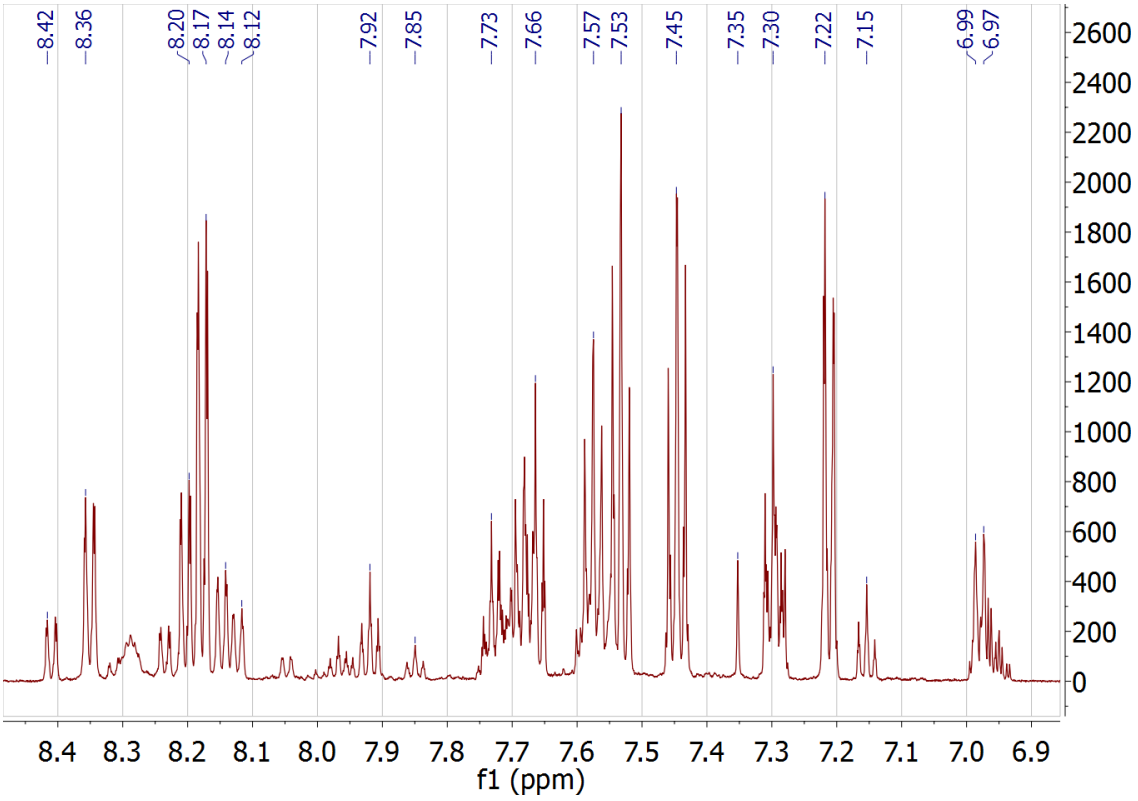

Figure S 2.17. Aromatic region of ^{1}H-NMR spectrum of BCF + 0.5 eq. BPO in CD_2Cl_2.

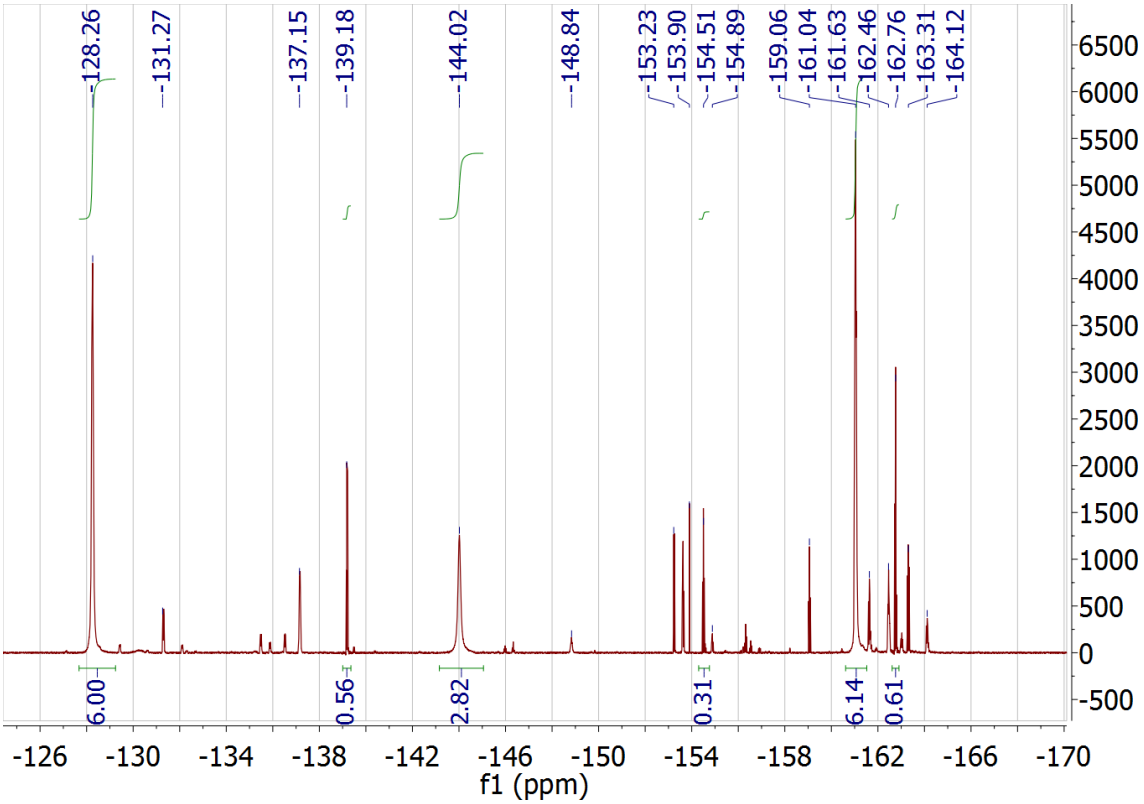

Figure S 2.18. ^{19}F-NMR spectrum of BCF + 0.5 eq. BPO in CD_2Cl_2.

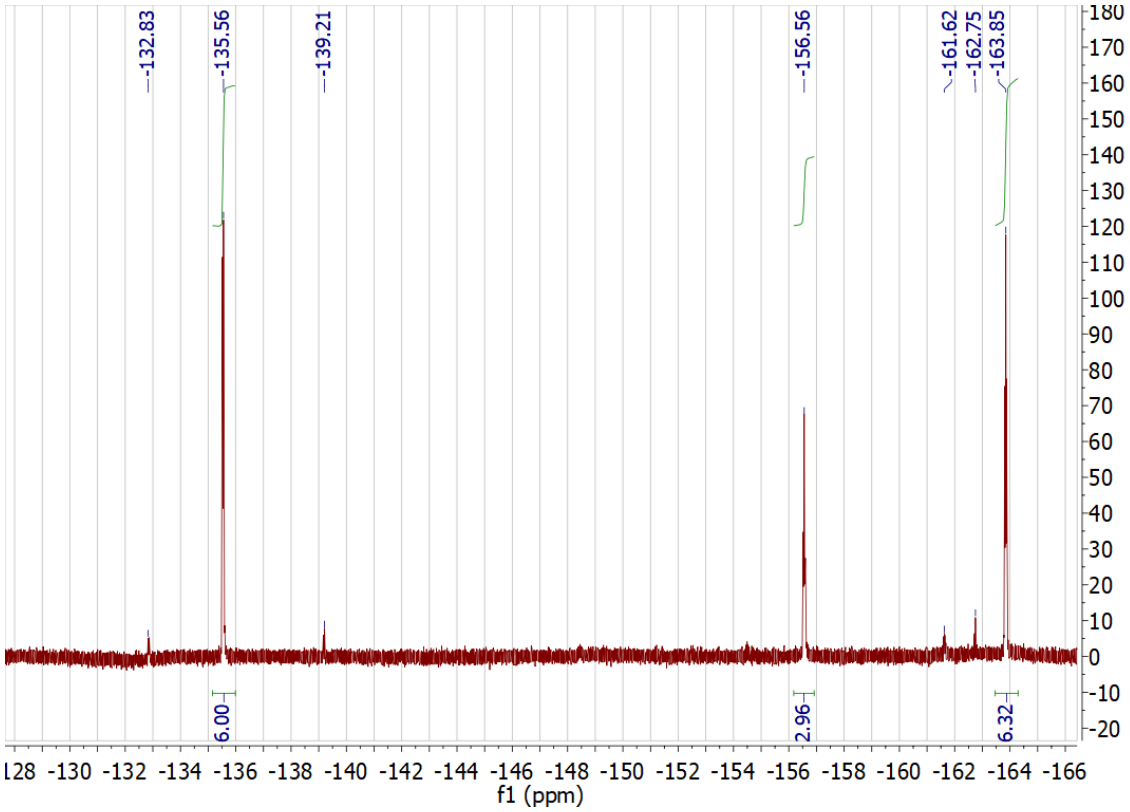

Figure S 2.19. ^{19}F-NMR spectrum of air-exposed BCF (95%, Sigma Aldrich) used to dope MEH-PPV, IDTBT, and PFO.

3.6.4 Additional Spectroscopy of Other Polymers

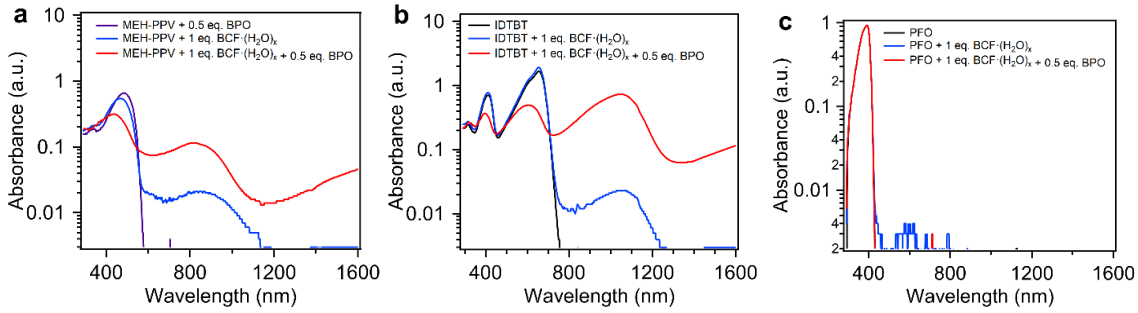

Figure S 2.20. Log scale UV-Vis spectra of doped MEH-PPV, IDTBT, and PFO solutions in chlorobenzene. (i.e. Log version of spectra in Figure 3.3)

3.6.5 GIWAXS

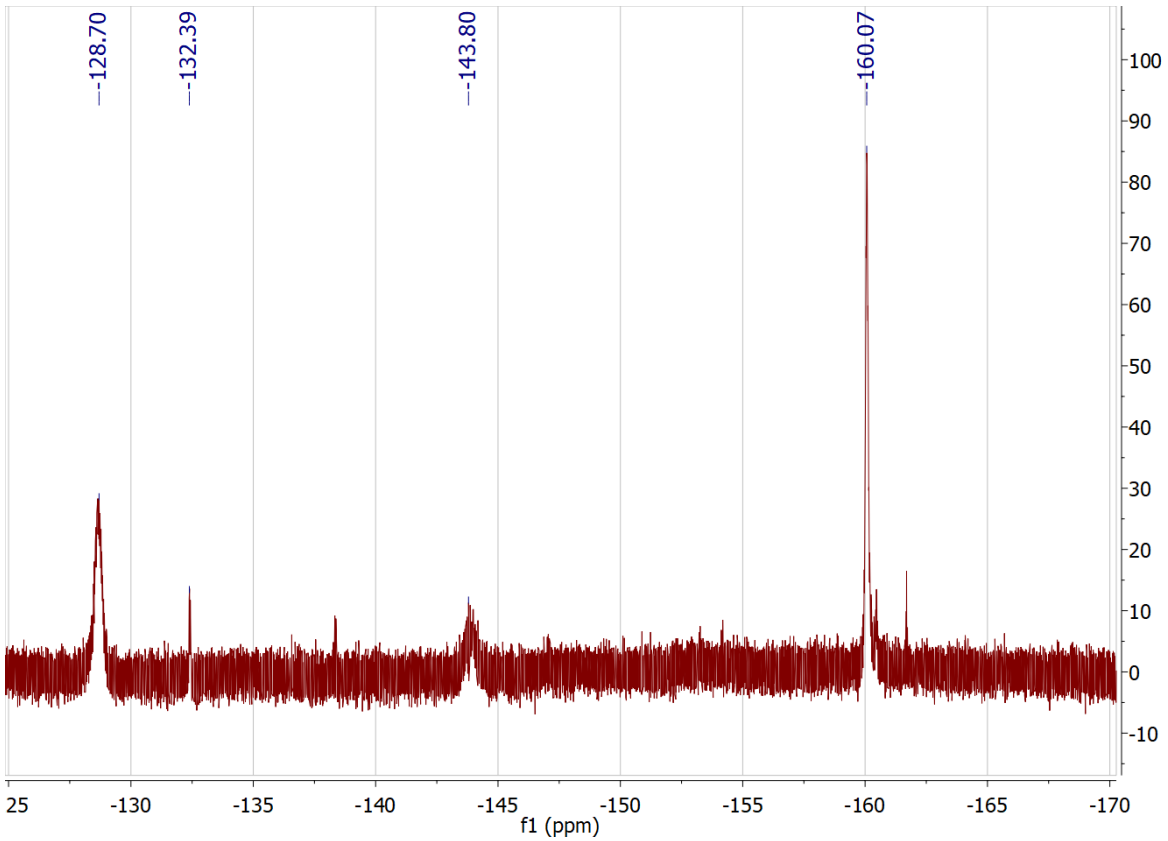

Figure S 2.21. ^{19}F-NMR spectrum in CD_2Cl_2 of sublimated BCF (Alfa Aesar) used for GIWAXS films.

BCF Doping GIWAXS:	P3HT	P3HT + 0.05 eq. BCF
	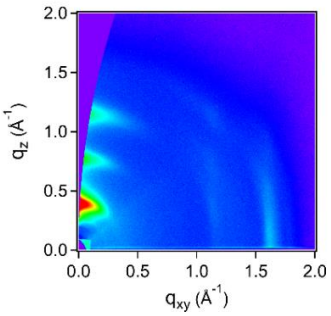	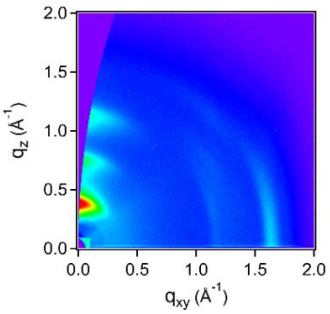
Alkyl spacing (Å)	16.2	16.7
π-π spacing (Å)	3.88	3.85
P3HT + 0.1 eq. BCF	P3HT + 0.2 eq. BCF	P3HT + 0.3 eq. BCF
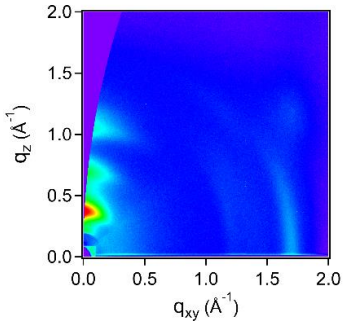	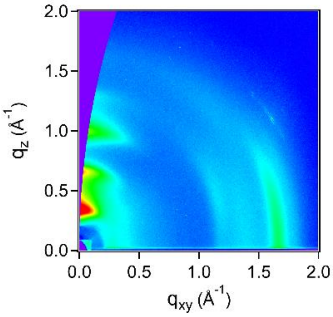	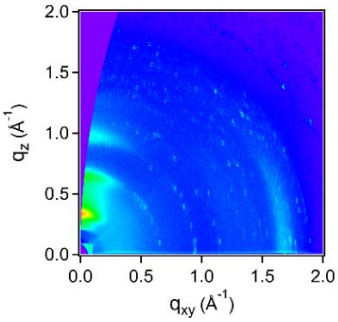
17.0	18.3	18.8
3.70	3.78	3.75

BCF + BPO Doping GIWAXS:	P3HT	P3HT + 0.05 eq. BCF + 0.025 eq. BPO
	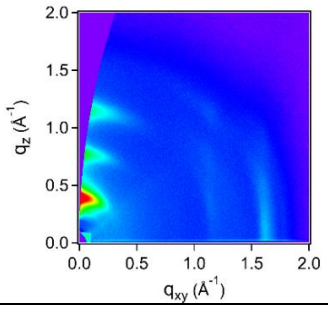	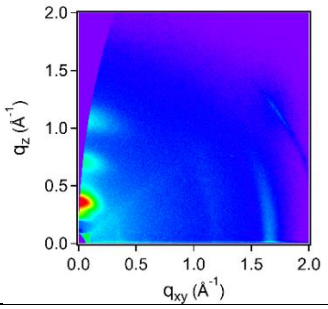
Alkyl spacing (Å)	16.2	17.5
π-π spacing (Å)	3.88	3.79
P3HT + 0.1 eq. BCF + 0.05 eq. BPO	P3HT + 0.2 eq. BCF + 0.1 eq. BPO	P3HT + 0.3 eq. BCF + 0.15 eq. BPO
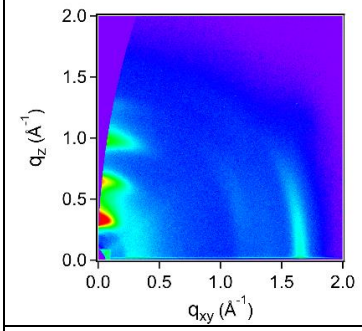	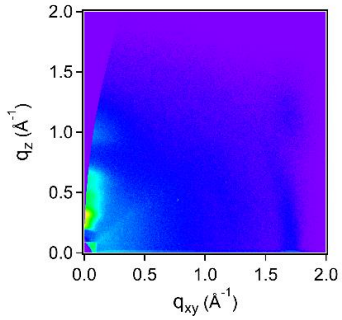	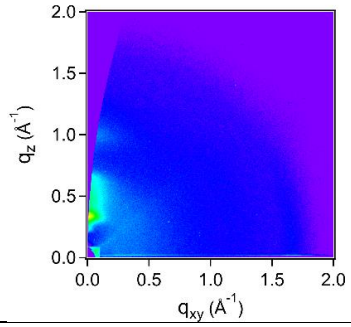
19.0	19.5	18.5
3.80	3.67	3.75

3.6.6 Film NIR+FTIR Fitting

The FTIR and NIR spectra between 0.055 – 1.0 eV of each film were fitted with 15 gaussian peaks using the IgorPro Multipeak Fitting 2 package. A constant baseline was manually set near the absorbance value at 1.0 eV. After using the "Auto-locate peaks" function to generate initial guesses for the IRAV (#4-11) and C-H stretch (#12-14) fitting functions, guesses for the broader functions (#0-3) were manually entered. During the fitting, peak locations, heights, and widths were allowed to vary freely.

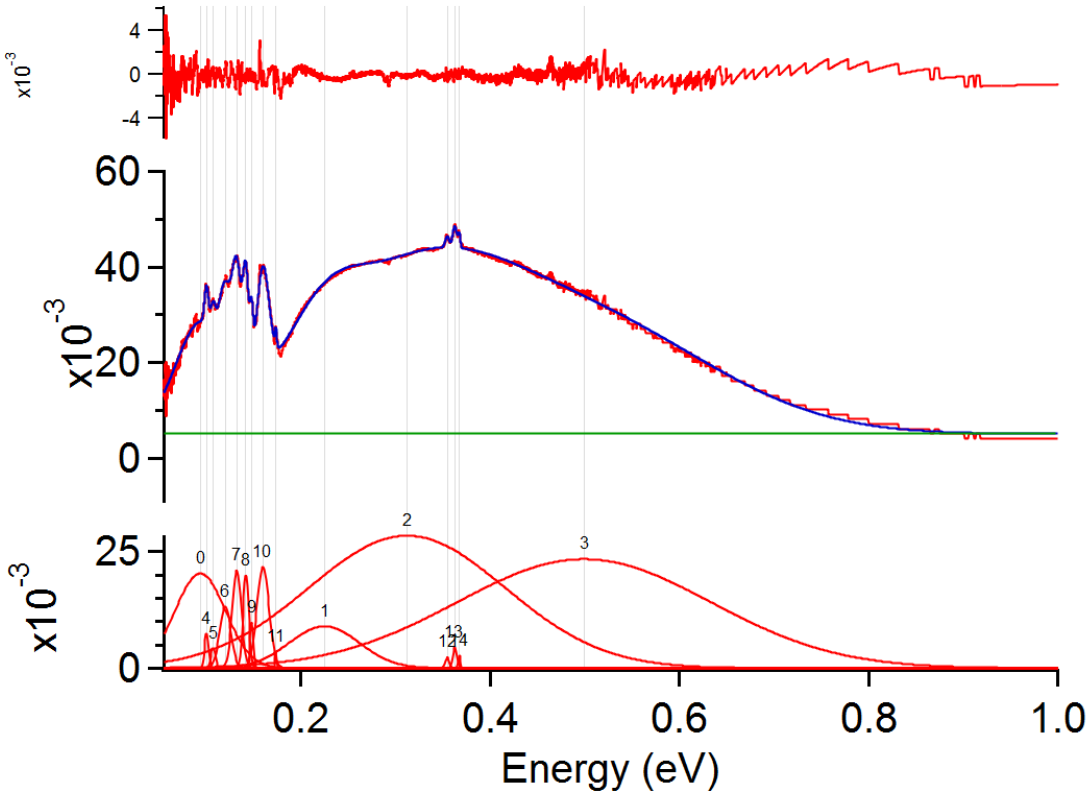

Figure S 2.22. Example of Gaussian fitting of FTIR and NIR spectra of P3HT + 0.05 eq. BCF:BPO film.

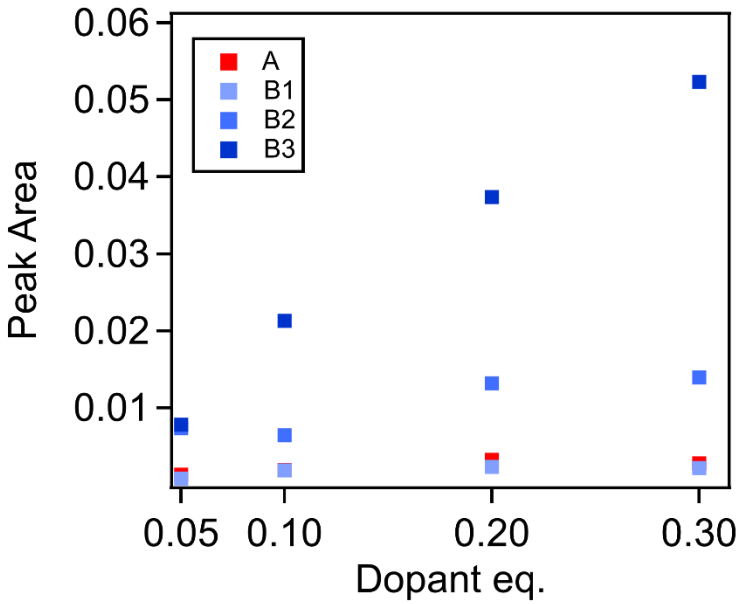

Figure S 2.23. Comparison of how the areas of the four polaron peak fitting functions change with doping.

Table S2. 1. Peak centers of four gaussian fitting peaks used to calculate the area of film IR P1 feature.

Peak Locations	A (eV)	B1 (eV)	B2 (eV)	B3 (eV)
+ 0.05 eq. BCF:BPO	0.093293	0.224423	0.311881	0.499107
+ 0.1 eq. BCF:BPO	0.093223	0.222113	0.309044	0.436165
+ 0.2 eq. BCF:BPO	0.089265	0.217534	0.293467	0.466241
+ 0.3 eq. BCF:BPO	0.089129	0.220794	0.289218	0.467767

Table S2. 2. Peak areas of four gaussian fitting peaks used to calculate the area of film IR P1 feature.

Peak Areas	A	B1	B2	B3
+ 0.05 eq. BCF:BPO	0.001358	0.000835	0.007396	0.007843
+ 0.1 eq. BCF:BPO	0.00195	0.001878	0.006477	0.021319
+ 0.2 eq. BCF:BPO	0.003292	0.002378	0.013209	0.037385
+ 0.3 eq. BCF:BPO	0.002832	0.002209	0.01397	0.052343

3.6.7 Conductivity

Table S2. 3. Conductivity values of BCF- and BCF:BPO-doped RR-P3HT films in this work.

	Conductivity (S/cm)		Conductivity (S/cm)
RR-P3HT	0.0013 ± 0.0002		
+ 0.05 eq. BCF	0.35 ± 0.07	+ 0.05 eq. BCF:BPO	0.4 ± 0.1
+ 0.1 eq. BCF	1.2 ± 0.2	+ 0.1 eq. BCF:BPO	7 ± 3
+ 0.2 eq. BCF	3.5 ± 0.5	+ 0.2 eq. BCF:BPO	25 ± 6
+ 0.3 eq. BCF	5.2 ± 0.6	+ 0.3 eq. BCF:BPO	20 ± 6

Table S2. 4. Comparison table of previous conductivity measurements of BCF-doped P3HT and PCPDTBT.

Polymer	BCF doping	Conditions	Conductivity (S/cm)	Ref.
P3HT	120%	In air	33.0	6
P3HT	25%	In N_2	0.020	6
P3HT	0.25/monomer		~10^{-3}	5
PCPDTBT	0.2 eq.	In N_2	8 x 10^{-3}	9
PCPDTBT	23 mol%		0.65	54

3.7. Appendix S3: Miscellaneous Lewis Acid-Base Experiments

3.7.1 GIWAXS of RRa-P3HT Doped by BCF:BPO

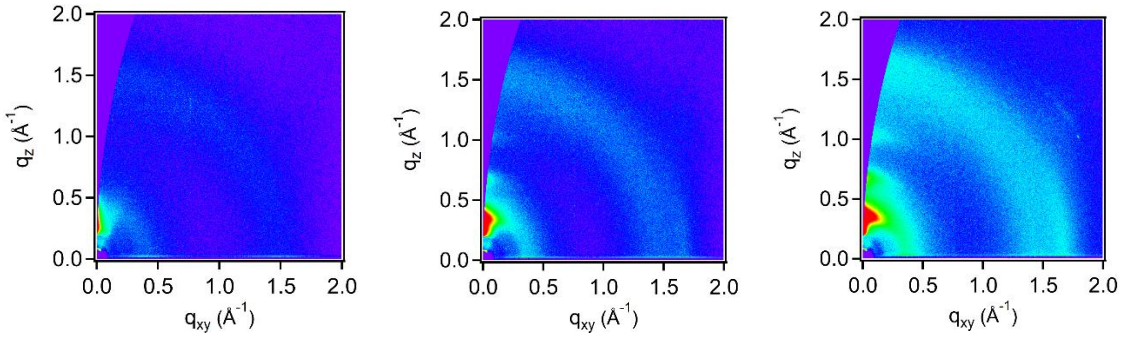

Figure S3. 1. GIWAXS of RRa-P3HT films (left) undoped, (center) doped with 0.1 eq. BCF:BPO, and (right) doped with 0.2 eq. BCF:BPO. Films were doped in solution and cast from 9:1 v/v chloroform:acetonitrile solvent. Alkyl stacking and π-π stacking peaks appeared in doped films, suggesting that doping causes aggregation of RRa-P3HT in solution or during casting.

3.7.2 GIWAXS of IDTBT Doped by BCF:BPO

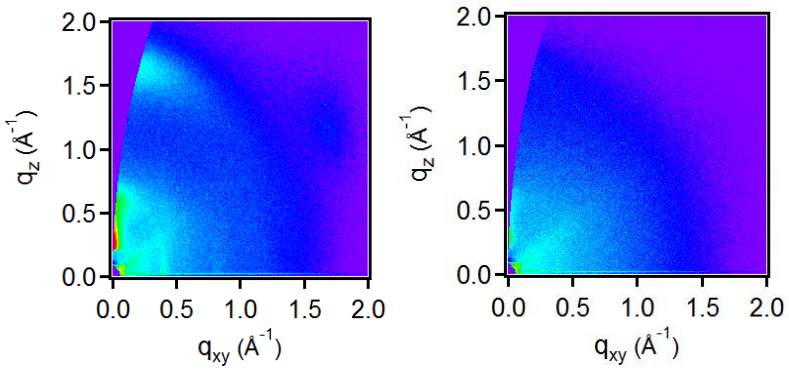

Figure S3. 2. GIWAXS of IDTBT films (left) undoped, and (right) doped with BCF:BPO. Undoped film shows weak face-on ordering, and doped film shows no ordering.

3.7.3 UV-Vis Spectroscopy of RR-P3HT doped by BCF:quinones

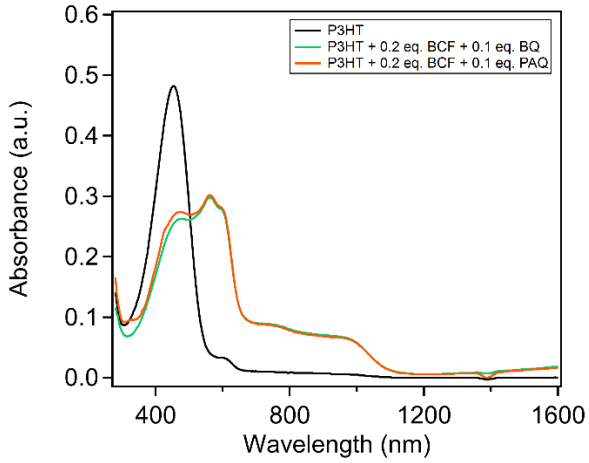

Figure S3. 3. Solution UV-Vis spectra of RR-P3HT and RR-P3HT doped by BCF and quinones. Quinones used were *p*-benzoquinone (BQ) and 9,10-phenanthrenedione (PAQ). Solutions were 0.05 mg/mL of P3HT in chloroform.

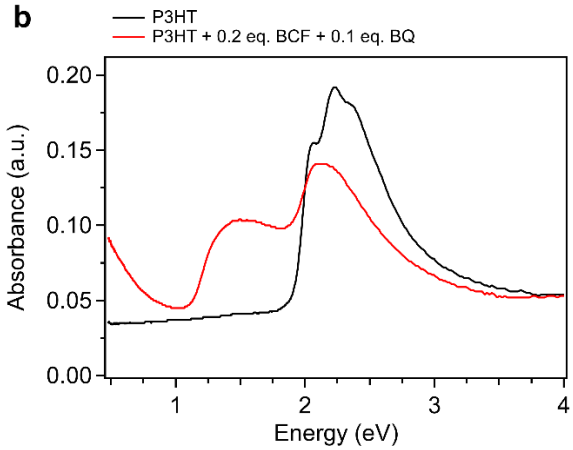

Figure S3. 4. UV-Vis-NIR spectra of RR-P3HT and BCF:BQ-doped RR-P3HT films.

3.8. References

1 I. E. Jacobs and A. J. Moulé, Controlling Molecular Doping in Organic Semiconductors, *Adv. Mater.*, 2017, **29**, 1703063.

2 K. A. Peterson, E. M. Thomas and M. L. Chabinyc, Thermoelectric Properties of Semiconducting Polymers, *Annu. Rev. Mater. Res.*, 2020, **50**, 551–574.

3 D. T. Scholes, S. A. Hawks, P. Y. Yee, H. Wu, J. R. Lindemuth, S. H. Tolbert and B. J. Schwartz, Overcoming Film Quality Issues for Conjugated Polymers Doped with F4TCNQ by Solution Sequential Processing: Hall Effect, Structural, and Optical Measurements, *J. Phys. Chem. Lett.*, 2015, **6**, 4786–4793.

4 L. Müller, D. Nanova, T. Glaser, S. Beck, A. Pucci, A. K. Kast, R. R. Schröder, E. Mankel, P. Pingel, D. Neher, W. Kowalsky and R. Lovrincic, Charge-Transfer–Solvent Interaction Predefines Doping Efficiency in p-Doped P3HT Films, *Chem. Mater.*, 2016, **28**, 4432–4439.

5 P. Pingel, M. Arvind, L. Kölln, R. Steyrleuthner, F. Kraffert, J. Behrends, S. Janietz and D. Neher, p-Type Doping of Poly(3-hexylthiophene) with the Strong Lewis Acid Tris(pentafluorophenyl)borane, *Adv. Electron. Mater.*, 2016, **2**, 1600204.

6 E. H. Suh, J. G. Oh, J. Jung, S. H. Noh, T. S. Lee and J. Jang, Brønsted Acid Doping of P3HT with Largely Soluble Tris(pentafluorophenyl)borane for Highly Conductive and Stable Organic Thermoelectrics Via One-Step Solution Mixing, *Adv. Energy Mater.*, 2020, **10**, 2002521.

7 A. E. Mansour, D. Lungwitz, T. Schultz, M. Arvind, A. M. Valencia, C. Cocchi, A. Opitz, D. Neher and N. Koch, The optical signatures of molecular-doping induced polarons in poly(3-hexylthiophene-2,5-diyl): individual polymer chains versus aggregates, *J. Mater. Chem. C*, 2020, **8**, 2870–2879.

8 M. Arvind, C. E. Tait, M. Guerrini, J. Krumland, A. M. Valencia, C. Cocchi, A. E. Mansour, N. Koch, S. Barlow, S. R. Marder, J. Behrends and D. Neher, Quantitative Analysis of Doping-Induced Polarons and Charge-Transfer Complexes of Poly(3-hexylthiophene) in Solution, *J. Phys. Chem. B*, 2020, **124**, 7694–7708.

9 B. Yurash, D. X. Cao, V. V. Brus, D. Leifert, M. Wang, A. Dixon, M. Seifrid, A. E. Mansour, D. Lungwitz, T. Liu, P. J. Santiago, K. R. Graham, N. Koch, G. C. Bazan and T.-Q. Nguyen, Towards understanding the doping mechanism of organic semiconductors by Lewis acids, *Nat. Mater.*, 2019, **18**, 1327–1334.

10 T. Ye, J. Wang, W. Chen, Y. Yang and D. He, Improved Performance and Reproducibility of Perovskite Solar Cells by Well-Soluble Tris(pentafluorophenyl)borane as a p-Type Dopant, *ACS Appl. Mater. Interfaces*, 2017, **9**, 17923–17931.

11 E. J. Lawrence, V. S. Oganesyan, G. G. Wildgoose and A. E. Ashley, Exploring the fate of the tris(pentafluorophenyl)borane radical anion in weakly coordinating solvents, *Dalton Trans.*, 2013, **42**, 782–789.

12 J. Panidi, A. F. Paterson, D. Khim, Z. Fei, Y. Han, L. Tsetseris, G. Vourlias, P. A. Patsalas, M. Heeney and T. D. Anthopoulos, Remarkable Enhancement of the Hole Mobility in Several Organic Small-Molecules, Polymers, and Small-Molecule:Polymer Blend Transistors by Simple Admixing of the Lewis Acid p-Dopant B(C6F5)3, *Adv. Sci.*, 2017, **5**, 1700290.

13 R. J. Kwaan, C. J. Harlan and J. R. Norton, Generation and Characterization of the Tris(pentafluorophenyl)borane Radical Anion, *Organometallics*, 2001, **20**, 3818–3820.

14 T. Beringhelli, D. Maggioni and G. D'Alfonso, 1H and 19F NMR Investigation of the Reaction of B(C6F5)3 with Water in Toluene Solution, *Organometallics*, 2001, **20**, 4927–4938.
15 P. S. Marqués, G. Londi, B. Yurash, T.-Q. Nguyen, S. Barlow, S. R. Marder and D. Beljonne, Understanding how Lewis acids dope organic semiconductors: a "complex" story, *Chem. Sci.*, 2021, **12**, 7012–7022.
16 B. Yurash, D. Leifert, G. N. M. Reddy, D. X. Cao, S. Biberger, V. V. Brus, M. Seifrid, P. J. Santiago, A. Köhler, B. F. Chmelka, G. C. Bazan and T.-Q. Nguyen, Atomic-Level Insight into the Postsynthesis Band Gap Engineering of a Lewis Base Polymer Using Lewis Acid Tris(pentafluorophenyl)borane, *Chem. Mater.*, 2019, **31**, 6715–6725.
17 G. C. Welch and G. C. Bazan, Lewis Acid Adducts of Narrow Band Gap Conjugated Polymers, *J. Am. Chem. Soc.*, 2011, **133**, 4632–4644.
18 Y. Han, G. Barnes, Y.-H. Lin, J. Martin, M. Al-Hashimi, S. Y. AlQaradawi, T. D. Anthopoulos and M. Heeney, Doping of Large Ionization Potential Indenopyrazine Polymers via Lewis Acid Complexation with Tris(pentafluorophenyl)borane: A Simple Method for Improving the Performance of Organic Thin-Film Transistors, *Chem. Mater.*, 2016, **28**, 8016–8024.
19 M. F. Roberts and S. A. Jenekhe, Lewis acid coordination complexes of polymers. 1. Boron chloride, aluminum chloride and gallium chloride complexes of poly(p-phenylenebenzobisthiazole), *Chem. Mater.*, 1993, **5**, 1744–1754.
20 J. T. Henthorn and T. Agapie, Dioxygen Reactivity with a Ferrocene–Lewis Acid Pairing: Reduction to a Boron Peroxide in the Presence of Tris(pentafluorophenyl)borane, *Angew. Chem. Int. Ed.*, 2014, **53**, 12893–12896.
21 L. L. Liu and D. W. Stephan, Radicals derived from Lewis acid/base pairs, *Chem. Soc. Rev.*, 2019, **48**, 3454–3463.
22 L. L. Liu, L. L. Cao, Y. Shao and D. W. Stephan, Single Electron Delivery to Lewis Pairs: An Avenue to Anions by Small Molecule Activation, *J. Am. Chem. Soc.*, 2017, **139**, 10062–10071.
23 X. Tao, C. G. Daniliuc, R. Knitsch, M. R. Hansen, H. Eckert, M. Lübbesmeyer, A. Studer, G. Kehr and G. Erker, The special role of B(C 6 F 5) 3 in the single electron reduction of quinones by radicals, *Chem. Sci.*, 2018, **9**, 8011–8018.
24 M.-H. Lee, J.-R. Chen, M. Das, T.-F. Hsieh and C.-M. Shu, Thermokinetic parameter evaluation by DSC and TAM III along with accountability of mass loss by TG from the thermal decomposition analyses of benzoyl peroxide, *J. Therm. Anal. Calorim.*, 2015, **122**, 1143–1150.
25 C. M. Cardona, W. Li, A. E. Kaifer, D. Stockdale and G. C. Bazan, Electrochemical Considerations for Determining Absolute Frontier Orbital Energy Levels of Conjugated Polymers for Solar Cell Applications, *Adv. Mater.*, 2011, **23**, 2367–2371.
26 S. Ko, E. T. Hoke, L. Pandey, S. Hong, R. Mondal, C. Risko, Y. Yi, R. Noriega, M. D. McGehee, J.-L. Brédas, A. Salleo and Z. Bao, Controlled Conjugated Backbone Twisting for an Increased Open-Circuit Voltage while Having a High Short-Circuit Current in Poly(hexylthiophene) Derivatives, *J. Am. Chem. Soc.*, 2012, **134**, 5222–5232.
27 F. C. Spano, Modeling disorder in polymer aggregates: The optical spectroscopy of regioregular poly(3-hexylthiophene) thin films, *J. Chem. Phys.*, 2005, **122**, 234701.
28 M. J. Nowak, D. Spiegel, S. Hotta, A. J. Heeger and P. A. Pincus, Charge storage on a conducting polymer in solution, *Macromolecules*, 1989, **22**, 2917–2926.

29 E. Lim, A. M. Glaudell, R. Miller and M. L. Chabinyc, The Role of Ordering on the Thermoelectric Properties of Blends of Regioregular and Regiorandom Poly(3-hexylthiophene), *Adv. Electron. Mater.*, 2019, **5**, 1800915.
30 P. Y. Yee, D. T. Scholes, B. J. Schwartz and S. H. Tolbert, Dopant-Induced Ordering of Amorphous Regions in Regiorandom P3HT, *J. Phys. Chem. Lett.*, 2019, **10**, 4929–4934.
31 R. Ghosh, A. R. Chew, J. Onorato, V. Pakhnyuk, C. K. Luscombe, A. Salleo and F. C. Spano, Spectral Signatures and Spatial Coherence of Bound and Unbound Polarons in P3HT Films: Theory Versus Experiment, *J. Phys. Chem. C*, 2018, **122**, 18048–18060.
32 H. Bronstein, D. S. Leem, R. Hamilton, P. Woebkenberg, S. King, W. Zhang, R. S. Ashraf, M. Heeney, T. D. Anthopoulos, J. de Mello and I. McCulloch, Indacenodithiophene-co-benzothiadiazole Copolymers for High Performance Solar Cells or Transistors via Alkyl Chain Optimization, *Macromolecules*, 2011, **44**, 6649–6652.
33 D. Venkateshvaran, M. Nikolka, A. Sadhanala, V. Lemaur, M. Zelazny, M. Kepa, M. Hurhangee, A. J. Kronemeijer, V. Pecunia, I. Nasrallah, I. Romanov, K. Broch, I. McCulloch, D. Emin, Y. Olivier, J. Cornil, D. Beljonne and H. Sirringhaus, Approaching disorder-free transport in high-mobility conjugated polymers, *Nature*, 2014, **515**, 384–388.
34 A. I. Hofmann, R. Kroon, S. Zokaei, E. Järsvall, C. Malacrida, S. Ludwigs, T. Biskup and C. Müller, Chemical Doping of Conjugated Polymers with the Strong Oxidant Magic Blue, *Adv. Electron. Mater.*, 2020, **6**, 2000249.
35 J. Hwang and A. Kahn, Electrical doping of poly(9,9-dioctylfluorenyl-2,7-diyl) with tetrafluorotetracyanoquinodimethane by solution method, *J. Appl. Phys.*, 2005, **97**, 103705.
36 J. Hynynen, D. Kiefer and C. Müller, Influence of crystallinity on the thermoelectric power factor of P3HT vapour-doped with F4TCNQ, *RSC Adv.*, 2018, **8**, 1593–1599.
37 I. Zozoulenko, A. Singh, S. K. Singh, V. Gueskine, X. Crispin and M. Berggren, Polarons, Bipolarons, And Absorption Spectroscopy of PEDOT, *ACS Appl. Polym. Mater.*, 2019, **1**, 83–94.
38 C. Enengl, S. Enengl, S. Pluczyk, M. Havlicek, M. Lapkowski, H. Neugebauer and E. Ehrenfreund, Doping-Induced Absorption Bands in P3HT: Polarons and Bipolarons, *ChemPhysChem*, 2016, **17**, 3836–3844.
39 D. Neusser, C. Malacrida, M. Kern, Y. M. Gross, J. van Slageren and S. Ludwigs, High Conductivities of Disordered P3HT Films by an Electrochemical Doping Strategy, *Chem. Mater.*, 2020, **32**, 6003–6013.
40 K. Kaneto, Y. Kohno and K. Yoshino, Polythiophene, Electrochemical Doping and Photoexcitation, *Mol. Cryst. Liq. Cryst.*, 1985, **118**, 217–220.
41 Z. Liang, H. H. Choi, X. Luo, T. Liu, A. Abtahi, U. S. Ramasamy, J. A. Hitron, K. N. Baustert, J. L. Hempel, A. M. Boehm, A. Ansary, D. R. Strachan, J. Mei, C. Risko, V. Podzorov and K. R. Graham, n-type charge transport in heavily p-doped polymers, *Nat. Mater.*, 2021, **20**, 518–524.
42 D. T. Scholes, P. Y. Yee, J. R. Lindemuth, H. Kang, J. Onorato, R. Ghosh, C. K. Luscombe, F. C. Spano, S. H. Tolbert and B. J. Schwartz, The Effects of Crystallinity on Charge Transport and the Structure of Sequentially Processed F4TCNQ-Doped Conjugated Polymer Films, *Adv. Funct. Mater.*, 2017, **27**, 1702654.

43 E. M. Thomas, K. A. Peterson, A. H. Balzer, D. Rawlings, N. Stingelin, R. A. Segalman and M. L. Chabinyc, Effects of Counter-Ion Size on Delocalization of Carriers and Stability of Doped Semiconducting Polymers, *Adv. Electron. Mater.*, 2020, **6**, 2000595.
44 T. J. Aubry, K. J. Winchell, C. Z. Salamat, V. M. Basile, J. R. Lindemuth, J. M. Stauber, J. C. Axtell, R. M. Kubena, M. D. Phan, M. J. Bird, A. M. Spokoyny, S. H. Tolbert and B. J. Schwartz, Tunable Dopants with Intrinsic Counterion Separation Reveal the Effects of Electron Affinity on Dopant Intercalation and Free Carrier Production in Sequentially Doped Conjugated Polymer Films, *Adv. Funct. Mater.*, 2020, **30**, 2001800.
45 M. G. Voss, D. T. Scholes, J. R. Challa and B. J. Schwartz, Ultrafast Transient Absorption Spectroscopy of Doped P3HT Films: Distinguishing Free and Trapped Polarons, *Faraday Discuss.*, 2019, **216**, 339–362.
46 Y. Xuan, X. Liu, S. Desbief, P. Leclère, M. Fahlman, R. Lazzaroni, M. Berggren, J. Cornil, D. Emin and X. Crispin, Thermoelectric properties of conducting polymers: The case of poly(3-hexylthiophene), *Phys. Rev. B*, 2010, **82**, 115454.
47 E. Lim, K. A. Peterson, G. M. Su and M. L. Chabinyc, Thermoelectric Properties of Poly(3-hexylthiophene) (P3HT) Doped with 2,3,5,6-Tetrafluoro-7,7,8,8-tetracyanoquinodimethane (F4TCNQ) by Vapor-Phase Infiltration, *Chem. Mater.*, 2018, **30**, 998–1010.
48 I. E. Jacobs, E. W. Aasen, J. L. Oliveira, T. N. Fonseca, J. D. Roehling, J. Li, G. Zhang, M. P. Augustine, M. Mascal and A. J. Moulé, Comparison of solution-mixed and sequentially processed P3HT:F4TCNQ films: effect of doping-induced aggregation on film morphology, *J. Mater. Chem. C*, 2016, **4**, 3454–3466.
49 D. T. Duong, C. Wang, E. Antono, M. F. Toney and A. Salleo, The chemical and structural origin of efficient p-type doping in P3HT, *Org. Electron.*, 2013, **14**, 1330–1336.
50 T. J. Aubry, J. C. Axtell, V. M. Basile, K. J. Winchell, J. R. Lindemuth, T. M. Porter, J.-Y. Liu, A. N. Alexandrova, C. P. Kubiak, S. H. Tolbert, A. M. Spokoyny and B. J. Schwartz, Dodecaborane-Based Dopants Designed to Shield Anion Electrostatics Lead to Increased Carrier Mobility in a Doped Conjugated Polymer, *Adv. Mater.*, 2019, **30**, 1805647.
51 L. L. Liu, L. L. Cao, D. Zhu, J. Zhou and D. W. Stephan, Homolytic cleavage of peroxide bonds via a single electron transfer of a frustrated Lewis pair, *Chem. Commun.*, 2018, **54**, 7431–7434.
52 L. L. Cao, K. L. Bamford, L. L. Liu and D. W. Stephan, Zinc-Containing Radical Anions via Single Electron Transfer to Donor–Acceptor Adducts, *Chem. - Eur. J.*, 2018, **24**, 3980–3983.
53 A. F. Paterson, L. Tsetseris, R. Li, A. Basu, H. Faber, A.-H. Emwas, J. Panidi, Z. Fei, M. R. Niazi, D. H. Anjum, M. Heeney and T. D. Anthopoulos, Addition of the Lewis Acid Zn(C6F5)2 Enables Organic Transistors with a Maximum Hole Mobility in Excess of 20 cm2 V−1 s−1, *Adv. Mater.*, 2019, **31**, 1900871.
54 J. Lee, J. Kim, T. L. Nguyen, M. Kim, J. Park, Y. Lee, S. Hwang, Y.-W. Kwon, J. Kwak and H. Y. Woo, A Planar Cyclopentadithiophene–Benzothiadiazole-Based Copolymer with sp2-Hybridized Bis(alkylsulfanyl)methylene Substituents for Organic Thermoelectric Devices, *Macromolecules*, 2018, **51**, 3360–3368.

4. Potential Frustrated Lewis Pair Mechanism for *n*-Type Doping

4.1. Introduction

In the previous chapter, we showed that a Lewis acid-base pair mechanism can use a Lewis acid to effectively *p*-type dope a wide range of semiconducting polymers. While *p*-type doping has challenges, *n*-type semiconducting polymers are even more difficult to study. In solution processible thermoelectric *n*-type polymers, the maximum conductivity and power factor is about an order of magnitude lower than that of *p*-type polymers.[1] *N*-type organic semiconductors need to have high electron affinities to avoid charge trapping by oxygen and water impurities (≈ -3.6 eV)[2] and for efficient doping. These properties make *n*-type organic semiconductor experiments much more sensitive to oxygen and water contamination and require synthetic chemists to design highly electron withdrawing molecules.[3] Overcoming this air instability also requires innovation in designing air stable dopants. The selection of *n*-type dopants is even more limited than that of *p*-type dopants and follows different doping mechanisms.

The use of Lewis acid-base pairs in *p*-type doping suggests there may be an opportunity to apply Lewis acid-base chemistry to the challenge of *n*-type doping. One revealing parallel is that, while Brønsted acids are used as *p*-type dopants, many *n*-type dopants are bases.[4] Amines have been commonly used as *n*-type dopants, including tetrakis(dimethylamino)ethylene[5] and triazabicyclodecene-based dopants.[6] Lewis bases in the form of N-heterocyclic carbenes have also shown potential as *n*-type dopants.[7–9] These basic *n*-type dopants suggest that there could be a *n*-type frustrated Lewis pair (FLP) doping mechanism involving Lewis bases.

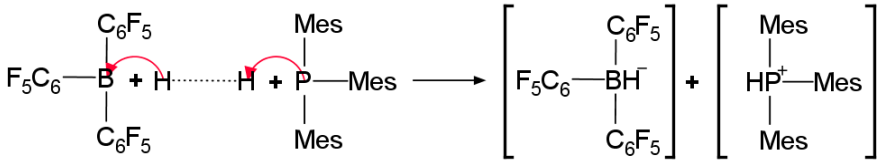

Scheme 4.1. H_2 activation by frustrated Lewis pair $B(C_6F_5)_3$ and $PMes_3$. H_2 splits heterolytically to yield borohydride and phosphonium ions.

One of the representative FLP reactions is the heterolytic activation of hydrogen (H_2) by the sterically hindered Lewis acid-base pair: tris(pentafluorophenyl)borane ($B(C_6F_5)_3$, BCF) and trimesitylphosphine ($PMes_3$).[10] In this reaction, the phosphine is protonated, while the borane accepts hydride (Scheme 4.1). This hydride transfer echoes the proposed hydride transfer mechanism of the common *n*-type dopant, 4-(2,3-Dihydro-1,3-dimethyl-1*H*-benzimidazol-2-yl)-*N*,*N*-dimethylbenzenamine (N-DMBI).[11,12] A recent study of this mechanism suggested that the most likely route for this reaction was:[11]

I. Hydride transfer from N-DMBI to a small molecule (acceptor, A)

II. Electron transfer from $AH^{\bullet -}$ to a second acceptor

III. Hydrogen elimination from two $AH^{\bullet}$ molecules

We propose that *n*-type organic semiconductors can act as the Lewis acid in a heterolytic H_2 activation with a sterically hindered Lewis base. This reaction would involve hydride transfer to the organic semiconductor, equivalent to the first step in the proposed doping mechanism of N-DMBI. In this chapter, we use thermochemical analysis and computation to examine the potential for a series of phosphines, in combination with H_2, to dope small molecule acceptors.

4.2. Computational Methods

We used Gaussian 16 to calculate the free energy of the species in our proposed reaction.[13] We performed our DFT calculations at the unrestricted ωB97X-D/6-31G++(d,p)

level in chloroform (C-PCM) with the default range tuning parameter, $\omega = 0.2$ Bohr^{-1}. Where possible, molecular geometries were tightly optimized. The triarylphosphine geometries generally do not converge at the tight level using basis set 6-31G++(d,p) in solvent. The protonated **P1** ($PMes_3H^+$) could only be optimized to a transition state with one negative vibrational mode. These computational conditions more closely match those used in the *p*-type Lewis acid doping study by Marqués et al.[14] than those of Jhulki et al.[11]

4.3. Results and Discussion

We chose to use two of the most easily doped small molecules from Jhulki et al.,[11] BDOPV and PDI-CN (Scheme 4.2). BDOPV is a model small molecule for the high performance *n*-type thermoelectric benzodifuran-paraphenylenevinylene polymers (FBDPPV, etc.).[15] Perylene diimides (PDIs) are commonly used as acceptors in organic solar cells or in electron transport layers.[16] The electron withdrawing cyano groups in both of these model small molecules may help them accept electrons more easily than similar molecules with different functional groups. The typical aliphatic groups were replaced with methyl groups to simplify computations. For the series of phosphines examined here (Scheme 4.2), we used common FLP triarylphosphines (PAr_3), as well as ones with electron donating methoxy- groups that are commercially available. Phosphines, including **P2** and **P4**, have been used before to *n*-type dope carbon nanotubes.[17]

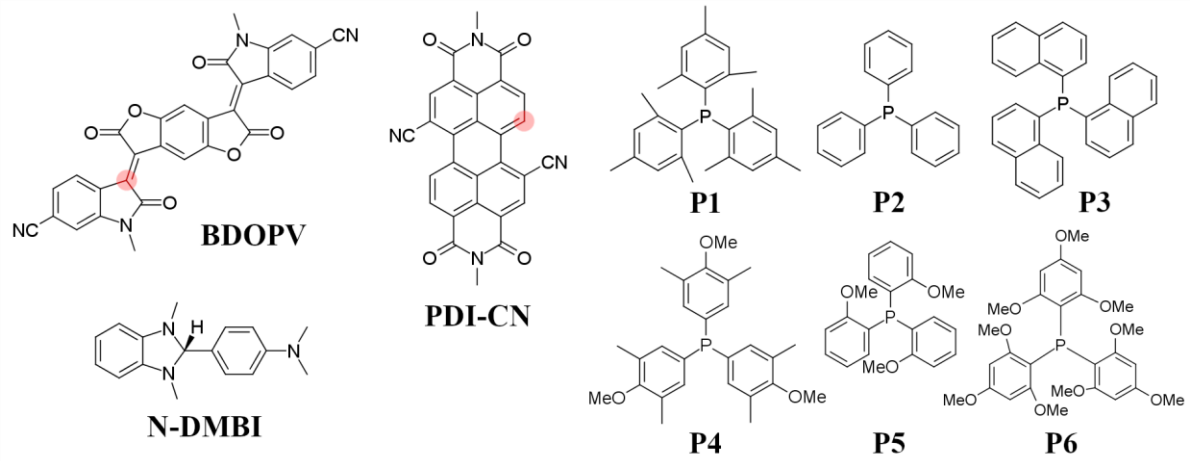

Scheme 4.2. Chemical structures of small molecule acceptors (BDOPV and PDI-CN), common *n*-type dopant N-DMBI, and six triarylphosphines (**P1-6**) studied in this chapter. The red dot on each acceptor indicates the hydride acceptance site used, chosen based on the most energetically favorable sites calculated in ref. [11]

First, we used experimentally known reaction energies to estimate whether this reaction mechanism would be energetically favorable. To do this, we first broke down the three steps of the proposed mechanism into component reactions (Table 4.1). Some of these steps (blue shaded) can be simplified because the acceptor (A) accepts a hydride, donates an electron, and then releases a hydrogen atom, which regenerates the neutral acceptor. While these steps are kinetically important, the overall energetics of those steps should be equal to the negative electron affinity of a hydrogen atom (Table 4.2, #3). Therefore, the reactions in Table 4.1 can be simplified to the five steps in Table 4.2. In Table 4.2, we used PDI-CN as the acceptor and triphenylphosphine (**P2**) as the phosphine. **P2** was the only phosphine in our study with an experimentally determined proton affinity in the NIST WebBook. Using the gas phase enthalpies from the NIST WebBook and the reduction potential of PDI-CN in solution, we estimated the overall energy of this doping reaction at +129 kJ/mol.

Table 4.1. Generic proposed n-type doping mechanism of an acceptor (A) by a triarylphosphine (PAr_3) and H_2 broken down into three reactions and their simpler component steps.

Overall		$2A + H_2 + PAr_3 \rightarrow A^{\bullet-} + A + ½H_2 + PAr_3H^+$
I.	H_2 Splitting	$H_2 \rightarrow H^+ + H^-$
		$A + H^- \rightarrow AH^{\bullet-}$
		$PAr_3 + H^+ \rightarrow PAr_3H^+$
II.	Electron transfer	$AH^{\bullet-} \rightarrow AH^{\bullet} + e^-$
		$e^- + A \rightarrow A^{\bullet-}$
III.	H_2 Elimination	$AH^{\bullet} \rightarrow A + H^{\bullet}$
		$H^{\bullet} \rightarrow ½H_2$

Table 4.2. Reaction energy of doping of PDI-CN by triphenylphosphine (PPh_3, P2) and H_2 estimated from known reaction energies.

	Reaction	Expt. Energy (kJ/mol)	Ref.
1	$H_2 \rightarrow H^+ + H^-$	+1675.3	[18]
2	$PPh_3 + H^+ \rightarrow PPh_3H^+$	-972.8††	[19]
3	$H^{\bullet-} \rightarrow H^{\bullet} + e^-$	+72.8††	[18]
4	$e^- + PDI\text{-}CN \rightarrow PDI\text{-}CN^{\bullet-}$	-428.4	[11]‡‡
5	$H^{\bullet} \rightarrow ½H_2$	-218	[20]
		+129	

††Proton and electron affinities are usually reported as a positive value. In this table, we used a sign convention where negative energies are energetically favorable.
‡‡The reduction potential of PDI-CN (-0.66 V vs. Fc^+/Fc^0 in CH_2Cl_2) was converted to -4.44 eV per ref. [21]

This estimate suggests that **P2** and H_2 would be unlikely to dope PDI-CN through this mechanism. Table 4.2 suggests there are limited chemical design options to make this reaction more energetically favorable. Three of the reaction energies are properties of hydrogen that cannot be changed. The electron affinity of the acceptor is a key property, but we have already chosen an acceptor with a high electron affinity. Finally, the proton affinity of the phosphine can be tuned by changing the functional groups on the phosphorus atom. We used free energy computations to examine a series of phosphine molecules to determine whether any of them could make this FLP *n*-type doping mechanism energetically favorable.

To better compare the calculations to the experimental estimate in Table 4.2, we calculated the proton affinities of **P1-6** (Table 4.3) as the absolute enthalpy change of phosphine bonding with a proton in chloroform. Our calculated proton affinity for **P2** was 753.0 kJ/mol, which is significantly lower than the gas phase ion value of 972.8 kJ/mol.[19] This discrepancy may indicate that our DFT method significantly underestimates proton affinities or that the proton affinity is lower in solution. All of the phosphines had a greater proton affinity than **P2**, with **P6** having the highest proton affinity of 850.2 kJ/mol. This value is almost 100 kJ/mol greater than that of **P2**, which could offset most of the estimated 129 kJ/mol needed to make this reaction energetically favorable.

Table 4.3. Calculated energy values for the proton affinity (enthalpy), free energy of H_2 splitting (step I), and total free energy (steps I-III) of triarylphosphines **P1-6** when doping PDI-CN and PDOPV.

(kJ/mol)	**Proton Affinity** ($CHCl_3$)	**PDI-CN**		**BDOPV**	
		ΔG_{split}	ΔG_T	ΔG_{split}	ΔG_T
P1	802.9	+37.2	+7.73	-34.7	+7.83
P2	753.0	+79.7	+50.2	+7.77	+50.3
P3	758.2	+77.9	+48.4	+5.95	+48.5
P4	769.4	+57.2	+27.7	-14.8	+27.8
P5	795.5	+39.0	+9.53	-32.9	+9.62
P6	850.2	-20.7	-50.2	-92.7	-50.1

We calculated the free energies of the reactant and product species of the proposed reactions to calculate the change in free energy. Because steps II and III (Table 4.1) only change with the acceptor, we report the free energy change of H_2 splitting in step I, ΔG_{split}, and the total free energy change of all three steps, ΔG_T. Both acceptors had very similar ΔG_T values for each phosphine, even though their ΔG_{split} values were often different. BDOPV's greater hydride affinity[11] makes ΔG_{split} lower for each reaction with BDOPV. Conversely,

the electron transfer (II) and H_2 elimination (III) steps are less favorable for BDOPV, with ΔG_{II} = +28.7 and ΔG_{III} = +13.8 kJ/mol for BDOPV. These reaction energies are lower for PDI-CN at ΔG_{II} = +19.0 and ΔG_{III} = -48.5 kJ/mol, making H_2 elimination from PDICN-H$^{\bullet}$ much more energetically favorable. Because electron transfer and H_2 elimination are energetically unfavorable for BDOPV-H$^{\bullet-}$, it may not follow those reaction steps. Jhulki et al. found that BDOPV-H$^{\bullet-}$ was stable but could decay to BDOPV$^{\bullet-}$ more quickly when exposed to O_2 or when excess BDOPV was present.[11]

While the total free energy of the reactions didn't vary much between BDOPV and PDI-CN, varying the triarylphosphine had a greater effect on ΔG_T. Only **P6** had a negative ΔG_T, indicating that the proposed reactions would be energetically favorable to dope BDOPV and PDI-CN. Two others, **P1** and **P5**, had negative ΔG_{split} values with BDOPV and low ΔG_Ts of ≈+8 and ≈+10 kJ/mol, respectively, with both acceptors. These results match expectations that the electron-donating methoxy- groups of **P5** and **P6** would increase the proton affinity and improve the energetic favorability over that of **P2**. **P4** also has methoxy- groups, but methoxy- groups in the *para*- position have been shown to be less basic than groups in the *ortho*- positions.[22] Steric hindrance may have played a role in making reactions with **P1** more favorable than those with **P2**. Changing the phenyl groups of **P2** to 1-naphthyl groups in **P3**, however, did not affect ΔG_T much. These results suggest that H_2 and **P6** could be used to dope organic semiconductors with electron affinity ≈4.5 eV.

4.4. Experimental Considerations

While these results suggest that FLP *n*-type doping with phosphines and H_2 is worth investigating experimentally, using H_2 gas for doping will require changes in solution preparation or film processing. Hydrogen gas also introduces new hazards into the doping

process because of its flammability and explosion risk. Mixtures in air above 4% hydrogen are flammable, so reactions with hydrogen need to be oxygen-free and kept away from ignition sources. A mixture of 5% hydrogen gas in nitrogen, commonly used to regenerate glovebox catalysts, could provide a convenient and safe way to test this type of reaction initially. This gas mixture could be bubbled through a solution of the acceptor and phosphine. Due to the high ionization energy of the phosphines (≈7 eV), electron transfer is unlikely to occur before introducing H_2. Alternatively, films cast from acceptor-phosphine mixture could be exposed to H_2 after casting.

Another potential issue with translating this potential doping mechanism to experiment is that unexpected reactions may occur. In particular, we note that **P5** and **P6** are not commonly used in FLP chemistry. They are more commonly used as organometallic ligands[23,24] or in nucleophilic substitution of halides.[25,26] **P6** has also recently been shown to methoxylate acyl fluorides.[27] In FLP chemistry, **P6** has been used in a Lewis pair polymerization of methylmethacrylate,[28] and **P5** attacks the aromatic group of $B(C_6F_5)_3$.[29] **P6** has even been noted to react with dichloromethane.[22] These uses of **P5** and **P6** suggest that it may have reactivity that makes it undesirable for use in FLP reactions. Another possibility is that stronger Lewis bases like **P5** and **P6** are simply not needed for H_2 activation with the strong Lewis acid $B(C_6F_5)_3$. Given the need to "balance" the Lewis acidity and basicity in H_2 activation,[30] stronger Lewis bases might be required for H_2 activation with the weaker Lewis acids of the organic semiconductors. In the case of undesired reactivity from **P5** or **P6**, the widely used **P1** may be the most likely phosphine, of the ones studied here, to be useful as an *n*-type dopant with H_2. If side reactions with

solvents are the only concern, adding the phosphine to the acceptor film through sequential casting or vapor diffusion could help.

4.5. Conclusions

We have proposed a novel *n*-type doping mechanism inspired by FLP chemistry. With sterically hindered phosphines as the Lewis base and the organic semiconductor as the Lewis acid, H_2 activation could initiate *n*-type doping with hydride transfer to the acceptor. We investigated this reaction mechanism using thermochemical reaction analysis and using DFT computations. Out of the series of phosphines studied, **P6** could make the proposed reaction energetically favorable with acceptors of 4.5 eV electron affinity. The use of H_2 gas in doping may require changes in film preparation, but the use of gases in doping is not new to the field of organic semiconductors. In addition to the earliest work using dopants like I_2 and AsF_5, CO_2 has recently been used in conjunction with LiTFSI for *p*-type doping.[31] The potential utility of this doping mechanism goes beyond the six phosphines studied here. Because phosphines are widely used in organometallic compounds, a wide variety of structures, sizes, and donor strengths are available[32] to optimize the energetics of doping and the film morphology.

4.6. Acknowledgements

Use was made of computational facilities purchased with funds from the National Science Foundation (CNS-1725797) and administered by the Center for Scientific Computing (CSC). The CSC is supported by the California NanoSystems Institute (CNSI) and the MRSEC (NSF DMR 1720256) at UC Santa Barbara.

4.7. References

1 K. A. Peterson, E. Lim and M. L. Chabinyc, in *Conjugated Polymers*, eds. J. R. Reynolds, B. C. Thompson and T. A. Skotheim, CRC Press, 4th edn., 2019, pp. 129–159.

2 H. T. Nicolai, M. Kuik, G. a. H. Wetzelaer, B. de Boer, C. Campbell, C. Risko, J. L. Brédas and P. W. M. Blom, Unification of trap-limited electron transport in semiconducting polymers, *Nat. Mater.*, 2012, **11**, 882–887.

3 H. Jia and T. Lei, Emerging research directions for n-type conjugated polymers, *J. Mater. Chem. C*, 2019, **7**, 12809–12821.

4 R. Kroon, D. A. Mengistie, D. Kiefer, J. Hynynen, J. D. Ryan, L. Yu and C. Müller, Thermoelectric plastics: from design to synthesis, processing and structure–property relationships, *Chem. Soc. Rev.*, 2016, **45**, 6147–6164.

5 J. Liu, Y. Shi, J. Dong, M. I. Nugraha, X. Qiu, M. Su, R. C. Chiechi, D. Baran, G. Portale, X. Guo and L. J. A. Koster, Overcoming Coulomb Interaction Improves Free-Charge Generation and Thermoelectric Properties for n-Doped Conjugated Polymers, *ACS Energy Lett.*, 2019, **4**, 1556–1564.

6 H. Nakayama, J. A. Schneider, M. Faust, H. Wang, J. Read de Alaniz and M. L. Chabinyc, A new family of liquid and solid guanidine-based n-type dopants for solution-processed perovskite solar cells, *Mater. Chem. Front.*, 2020, **4**, 3616-3622.

7 Y.-F. Ding, C.-Y. Yang, C.-X. Huang, Y. Lu, Z.-F. Yao, C.-K. Pan, J.-Y. Wang and J. Pei, Thermally Activated n-Doping of Organic Semiconductors Achieved by N-Heterocyclic Carbene Based Dopant, *Angew. Chem.*, 2021, **133**, 5880–5884.

8 D. Schmidt, D. Bialas and F. Würthner, Ambient Stable Zwitterionic Perylene Bisimide-Centered Radical, *Angew. Chem.*, 2015, **127**, 3682–3685.

9 H. Li, C. Risko, J. H. Seo, C. Campbell, G. Wu, J.-L. Brédas and G. C. Bazan, Fullerene–Carbene Lewis Acid–Base Adducts, *J. Am. Chem. Soc.*, 2011, **133**, 12410–12413.

10 G. C. Welch and D. W. Stephan, Facile Heterolytic Cleavage of Dihydrogen by Phosphines and Boranes, *J. Am. Chem. Soc.*, 2007, **129**, 1880–1881.

11 S. Jhulki, H.-I. Un, Y.-F. Ding, C. Risko, S. K. Mohapatra, J. Pei, S. Barlow and S. R. Marder, Reactivity of an air-stable dihydrobenzoimidazole n-dopant with organic semiconductor molecules, *Chem*, 2021, **7**, 1050–1065.

12 B. D. Naab, S. Guo, S. Olthof, E. G. B. Evans, P. Wei, G. L. Millhauser, A. Kahn, S. Barlow, S. R. Marder and Z. Bao, Mechanistic Study on the Solution-Phase n-Doping of 1,3-Dimethyl-2-aryl-2,3-dihydro-1H-benzoimidazole Derivatives, *J. Am. Chem. Soc.*, 2013, **135**, 15018–15025.

13 Gaussian 16, Revision C.01, Frisch, M. J.; Trucks, G. W.; Schlegel, H. B.; Scuseria, G. E.; Robb, M. A.; Cheeseman, J. R.; Scalmani, G.; Barone, V.; Petersson, G. A.; Nakatsuji, H.; Li, X.; Caricato, M.; Marenich, A. V.; Bloino, J.; Janesko, B. G.; Gomperts, R.; Mennucci, B.; Hratchian, H. P.; Ortiz, J. V.; Izmaylov, A. F.; Sonnenberg, J. L.; Williams-Young, D.; Ding, F.; Lipparini, F.; Egidi, F.; Goings, J.; Peng, B.; Petrone, A.; Henderson, T.; Ranasinghe, D.; Zakrzewski, V. G.; Gao, J.; Rega, N.; Zheng, G.; Liang, W.; Hada, M.; Ehara, M.; Toyota, K.; Fukuda, R.; Hasegawa, J.; Ishida, M.; Nakajima, T.; Honda, Y.; Kitao, O.; Nakai, H.; Vreven, T.; Throssell, K.; Montgomery, J. A., Jr.; Peralta, J. E.; Ogliaro, F.; Bearpark, M. J.; Heyd, J. J.; Brothers, E. N.; Kudin, K. N.; Staroverov, V. N.; Keith, T. A.; Kobayashi, R.; Normand, J.; Raghavachari, K.; Rendell, A. P.; Burant, J. C.; Iyengar, S. S.; Tomasi, J.; Cossi, M.; Millam, J. M.; Klene, M.; Adamo, C.; Cammi, R.;

Ochterski, J. W.; Martin, R. L.; Morokuma, K.; Farkas, O.; Foresman, J. B.; Fox, D. J. Gaussian, Inc., Wallingford CT, 2016.
14 P. S. Marqués, G. Londi, B. Yurash, T.-Q. Nguyen, S. Barlow, S. R. Marder and D. Beljonne, Understanding how Lewis acids dope organic semiconductors: a “complex” story, *Chem. Sci.*, 2021, **12**, 7012–7022.
15 K. Shi, F. Zhang, C.-A. Di, T.-W. Yan, Y. Zou, X. Zhou, D. Zhu, J.-Y. Wang and J. Pei, Toward High Performance n-Type Thermoelectric Materials by Rational Modification of BDPPV Backbones, *J. Am. Chem. Soc.*, 2015, **137**, 6979–6982.
16 K. Balakrishnan, A. Datar, T. Naddo, J. Huang, R. Oitker, M. Yen, J. Zhao and L. Zang, Effect of Side-Chain Substituents on Self-Assembly of Perylene Diimide Molecules: Morphology Control, *J. Am. Chem. Soc.*, 2006, **128**, 7390–7398.
17 Y. Nonoguchi, K. Ohashi, R. Kanazawa, K. Ashiba, K. Hata, T. Nakagawa, C. Adachi, T. Tanase and T. Kawai, Systematic Conversion of Single Walled Carbon Nanotubes into n-type Thermoelectric Materials by Molecular Dopants, *Sci. Rep.*, 2013, **3**, 3344.
18 R. C. Shiell, X. K. Hu, Q. C. J. Hu and J. W. Hepburn, in *NIST Chemistry WebBook, NIST Standard Reference Database Number 69*, eds. P. J. Linstrom and W. G. Mallard, National Institute of Standards and Technology, Gaithersburg MD, 20899.
19 E. P. Hunter and S. G. Lias, in *NIST Chemistry WebBook, NIST Standard Reference Database Number 69*, eds. P. J. Linstrom and W. G. Mallard, National Institute of Standards and Technology, Gaithersburg MD, 20899.
20 M. W. Chase Jr., in *NIST Chemistry WebBook, NIST Standard Reference Database Number 69*, eds. P. J. Linstrom and W. G. Mallard, National Institute of Standards and Technology, Gaithersburg MD, 20899.
21 C. M. Cardona, W. Li, A. E. Kaifer, D. Stockdale and G. C. Bazan, Electrochemical Considerations for Determining Absolute Frontier Orbital Energy Levels of Conjugated Polymers for Solar Cell Applications, *Adv. Mater.*, 2011, **23**, 2367–2371.
22 M. Wada and S. Higashizaki, A highly basic triphenylphosphine, [2,4,6-(MeO)3C6H2]3P, *J. Chem. Soc., Chem. Commun.*, 1984, 482–483.
23 J.-S. Sun, C. E. Uzelmeier, D. L. Ward and K. R. Dunbar, Pd(II) and Pt(II) complexes with mixed phosphorus-oxygen donor ligands, *Polyhedron*, 1998, **17**, 2049–2063.
24 N. A. Barnes, S. M. Godfrey, R. T. A. Halton, I. Mushtaq and R. G. Pritchard, The reaction of tertiary phosphines with (Ph2Se2I2)2—the influence of steric and electronic effects, *Dalton Trans.*, 2006, 4795–4804.
25 J. Saame, T. Rodima, S. Tshepelevitsh, A. Kütt, I. Kaljurand, T. Haljasorg, I. A. Koppel and I. Leito, Experimental Basicities of Superbasic Phosphonium Ylides and Phosphazenes, *J. Org. Chem.*, 2016, **81**, 7349–7361.
26 A. Taladriz, A. Healy, E. J. Flores Pérez, V. Herrero García, C. Ríos Martínez, A. A. M. Alkhaldi, A. A. Eze, M. Kaiser, H. P. de Koning, A. Chana and C. Dardonville, Synthesis and Structure–Activity Analysis of New Phosphonium Salts with Potent Activity against African Trypanosomes, *J. Med. Chem.*, 2012, **55**, 2606–2622.
27 X. Wang, Z. Wang, T. Ishida and Y. Nishihara, Methoxylation of Acyl Fluorides with Tris(2,4,6-trimethoxyphenyl)phosphine via C–OMe Bond Cleavage under Metal-Free Conditions, *J. Org. Chem.*, 2020, **85**, 7526–7533.
28 W. Nzahou Ottou, E. Conde-Mendizabal, A. Pascual, A.-L. Wirotius, D. Bourichon, J. Vignolle, F. Robert, Y. Landais, J.-M. Sotiropoulos, K. Miqueu and D. Taton, Organic Lewis Pairs Based on Phosphine and Electrophilic Silane for the Direct and Controlled

Polymerization of Methyl Methacrylate: Experimental and Theoretical Investigations, *Macromolecules*, 2017, **50**, 762–774.
29 G. C. Welch, R. Prieto, M. A. Dureen, A. J. Lough, O. A. Labeodan, T. Höltrichter-Rössmann and D. W. Stephan, Reactions of phosphines with electron deficient boranes, *Dalton Trans.*, 2009, 1559–1570.
30 J. Paradies, From structure to novel reactivity in frustrated Lewis pairs, *Coord. Chem. Rev.*, 2019, **380**, 170–183.
31 J. Kong, Y. Shin, J. A. Röhr, H. Wang, J. Meng, Y. Wu, A. Katzenberg, G. Kim, D. Y. Kim, T.-D. Li, E. Chau, F. Antonio, T. Siboonruang, S. Kwon, K. Lee, J. R. Kim, M. A. Modestino, H. Wang and A. D. Taylor, CO2 doping of organic interlayers for perovskite solar cells, *Nature*, 2021, **594**, 51–56.
32 A. S. Balueva, E. I. Musina and A. A. Karasik, in *Organophosphorus Chemistry: Volume 47*, 2018, pp. 1–49.

5. Conclusions

In this work, we have investigated several organic semiconductor and dopant systems through the lenses of chemical mechanism, electronic structure, or morphology. In our small molecule system, the relatively constant morphology and simple electron-transfer doping made smaller changes in electronic structure more apparent. The increase in Seebeck coefficient at high doping levels was connected to broadening of the density of states by doubly oxidized molecules. We studied the Lewis acid-base pair of BCF and BPO for *p*-type doping and found that BPO increases the doping efficiency of BCF. The large resulting counterion leads to a long polaron-anion distance and delocalized polarons, but it may hinder aggregation at higher dopant concentrations. Films cast from BCF:BPO-doped P3HT solutions had a high conductivity relative to other P3HT solution doping experiments. Finally, we explored the potential of H_2 and triarylphosphines for *n*-type doping using computations. We found that some highly Lewis basic phosphines may come close to making the proposed doping mechanism energetically favorable. However, establishing whether these reactions can occur in experiment depends on the reaction kinetics, as well as overcoming the experimental challenges of using H_2 gas and minimizing potential side reactions.

These three doping studies show that exploring new doping chemistry may be required to reach the conductivities desired for electronic and energy conversion devices. At high conductivities, the electronic nature of the charge carriers can change, and understanding this electronic structure is crucial for controlling transport in the material. Morphology and electronic structure can be altered simultaneously by dopants, so understanding their interrelation is important, as well. Our work suggests there are more dopant combinations to

explore in Lewis acid-base chemistry and offers ways to connect the changes in electronic structure, morphology, and transport caused by these new dopants.